

POLITECNICO DI TORINO

Collegio di Ingegneria Chimica e dei Materiali

**Corso di Laurea Magistrale
in Ingegneria dei Materiali**

Tesi di Laurea Magistrale

**Magnesium Silicide: a novel, silicon-based material for
printable thermoelectric devices**



Relatori

prof. Fabrizio Giorgis

prof. Isabel Ferreira

Candidato

Davide Miglietta

Luglio 2018

*Alla mia famiglia,
il mio porto sicuro*

Table of contents

| | |
|---|----|
| Riassunto | IV |
| 1 Introduction..... | 1 |
| 1.1 Thesis Structure..... | 3 |
| 2 Thermoelectricity..... | 5 |
| 2.1 Thermoelectric effects [6, 7] | 5 |
| 2.2 P-type and n-type semiconductors [8]..... | 6 |
| 2.3 ZT Figure of merit and TE efficiency [8, 9]..... | 6 |
| 2.4 Thermoelectric generators (TEGs) [10] | 8 |
| 2.5 TEGs applications [10]..... | 10 |
| 2.6 Traditional Thermoelectric Materials [12, 13] | 12 |
| 3 Magnesium Silicide: A Novel Thermoelectric Material..... | 15 |
| 3.1 Magnesium Silicide: structure and physico-chemical properties | 15 |
| 3.2 Chemical reactivity of Magnesium Silicide | 16 |
| 3.3 Mg ₂ Si Fabrication Routes and State of the Art | 17 |
| 3.3.1 Fabrication Routes: Melting Techniques..... | 18 |
| 3.3.2 Fabrication Routes: Solid-state synthesis | 19 |
| 3.4 Doped Magnesium Silicide and its Solid Solutions | 22 |
| 3.4.1 N-type dopants | 22 |
| 3.4.2 P-type dopants | 25 |
| 4 Characterization Techniques..... | 27 |
| 4.1 Scanning Electron Microscopy (SEM)..... | 27 |
| 4.2 X-ray Diffraction (XRD)..... | 28 |
| 4.3 Raman Spectroscopy | 29 |
| 4.4 Infrared Spectroscopy (FTIR) | 30 |
| 4.5 DSC/TGA..... | 30 |
| 5 Magnesium Silicide Synthesis | 33 |
| 5.1 Ball milling and mechanical alloying [49-54]..... | 33 |
| 5.2 Ball mill..... | 33 |
| 5.2.1 Planetary ball mill | 34 |
| 5.2.2 Selection of tools materials | 34 |
| 5.2.3 Ball dimension and number, mass ratio balls to powder..... | 35 |
| 5.2.4 Dry and Wet Milling | 36 |
| 5.2.5 Overheating | 37 |
| 5.2.6 Inert Atmosphere..... | 37 |
| 5.3 Increase of internal energy and alloying mechanism | 37 |

| | | |
|-------|--|----|
| 5.3.1 | Alloying Mechanism | 37 |
| 5.4 | Experimental setting..... | 37 |
| 5.4.1 | Materials and milling parameters | 39 |
| 5.4.2 | Calculations | 39 |
| 5.4.3 | Procedure..... | 40 |
| 5.5 | Annealing temperature choice by DSC/TGA analysis | 41 |
| 5.5.1 | Results: | 41 |
| 5.5.2 | DSC results comparison and discussion: | 43 |
| 5.5.3 | TGA results comparison and discussion: | 44 |
| 5.6 | Mg ₂ Si formation reaction by thermal annealing and inert atmosphere comparison | 45 |
| 5.6.1 | Experimental setting..... | 45 |
| 5.6.2 | Five hours milled powder..... | 46 |
| 5.6.3 | Synthesis from commercial powder (unmilled) | 50 |
| 5.7 | Characterization of annealed powder | 51 |
| 5.7.1 | XRD results | 51 |
| 5.7.2 | Raman results | 59 |
| 5.7.3 | IR results..... | 60 |
| 5.7.4 | SEM results | 62 |
| 6 | 3d Printing of silicon and magnesium silicide powder | 69 |
| 6.1 | 3d printing technologies | 69 |
| 6.2 | Experimental Setting: 3D Printer | 69 |
| 6.3 | Extrudable Paste and After-Printing Treatment | 71 |
| 6.4 | Paste formulation..... | 71 |
| 6.4.1 | Materials..... | 72 |
| 6.5 | Paste formulation: Preliminary study | 75 |
| 6.5.1 | Procedure..... | 76 |
| 6.5.2 | Tested materials and formulations..... | 78 |
| 6.5.3 | Selected formulations | 84 |
| 6.5.4 | Influence of powder grain size | 84 |
| 6.6 | DSC/TGA Analysis for de-binding temperature determination..... | 86 |
| 6.6.1 | Polystyrene formulations: DSC/TGA results | 86 |
| 6.6.2 | Ethyl cellulose formulations..... | 89 |
| 6.6.3 | Resume: Burnout Temperatures | 90 |
| 6.7 | 3D printing of Mg ₂ Si powder | 90 |
| 6.7.1 | Post processing: de-binding and sintering..... | 91 |
| 6.7.2 | Experimental setting..... | 92 |
| 7 | Conclusions..... | 97 |

| | |
|------------------------------------|-----|
| 7.1 Future perspectives | 99 |
| List of Symbols and Acronyms | 100 |
| List of Figures | 102 |
| List of tables | 105 |
| Bibliography..... | 106 |
| Acknowledgements | 110 |

Riassunto

Nell'ottica di uno sviluppo sostenibile e di un utilizzo efficiente ed efficace delle risorse, in un mondo dove cambiamento climatico, sovrappollazione e scarsità delle risorse sono problemi reali, è dirimente lo studio e lo sviluppo di soluzioni tecnologiche innovative. Soluzioni che siano in grado di dare una risposta alle sopracitate criticità.

Alcune delle opzioni che più specificamente riguardano il campo dell'ingegneria dei materiali sono: lo studio di materiali innovativi ed eco-friendly, graduale soppiantamento delle fonti di energia non rinnovabili in favore di quelle rinnovabili, ottimizzazione dei processi (industriali e non) esistenti anche in termini di riutilizzo di sottoprodotti come materiali di scarto o calore dissipato ("waste heat"). Il calore, infatti, è un sottoprodotto di innumerevoli processi industriali, domestici e anche, per esempio, nel settore dei trasporti. In alcuni casi questo "waste heat" è riutilizzato ma in molti altri casi è dissipato, dando chiaramente luogo ad uno spreco di quello che da sottoprodotto potrebbe trasformarsi in risorsa.

In quest'ottica i materiali termoelettrici possono giocare un ruolo chiave. La termoelettricità è una proprietà dei materiali per cui il calore è trasformato direttamente in elettricità. La termoelettricità è una caratteristica comune a tutti i materiali, ma è rilevante nei materiali cosiddetti termoelettrici. I dispositivi basati su questi principi non presentano parti in movimento e sono caratterizzati da architetture relativamente semplici, in quanto sfruttano una proprietà intrinseca dei materiali. Nel corso degli anni, lo studio della termoelettricità ha visto periodi di grande interesse e ricerca alternati a momenti dove la ricerca in questo campo è stata sensibilmente meno attiva. Questo perché, pur riconoscendone il grande potenziale, alcune serie problematiche hanno limitato la produzione su larga scala di tali dispositivi. In prima battuta la loro efficienza non è ancora pienamente soddisfacente e la scarsità, e quindi costo elevato, dei materiali tradizionalmente utilizzati sono state le principali ragioni. Ad esempio, Tellurio, Germanio (materiali rari e costosi) e Piombo (tossico) hanno permesso lo sviluppo di generatori termoelettrici allo stato solido relativamente efficienti e molto affidabili che hanno avuto diffusione solo in ambito aerospaziale (generazione di elettricità su sonde spaziali), dove l'elevato costo non è un problema così dirimente.

In quest'ottica è chiaramente necessario lo sviluppo di materiali innovativi che pareggino le prestazioni e affidabilità dei materiali tradizionali e che siano allo stesso tempo economici e diffusi. Il siliciuro di magnesio Mg_2Si , oggetto di questa tesi, è un serio candidato come materiale termoelettrico innovativo e sostenibile. Una combinazione di proprietà fisiche, chimiche ed elettriche favorevoli rende questo composto intermetallico particolarmente interessante e futuribile. I costituenti (silicio e magnesio), inoltre, sono tra i materiali più diffusi sulla crosta terrestre e sono non tossici.

Questa tesi, nel contesto presentato, propone la sintesi del siliciuro partendo dalle polveri dei costituenti, tramite processo di "ball milling/mechanical alloying" seguito da un trattamento termico per permettere l'avvenimento della reazione chimica di formazione.

La seconda parte del lavoro sperimentale riguarda lo stampaggio in 3d delle polveri ottenute. L'additive manufacturing è un processo universalmente riconosciuto come un metodo veloce e versatile per la produzione di pezzi per ogni tipo di applicazione, applicabile ai più svariati materiali. Ovviamente sono disponibili numerosi metodi di stampaggio 3d applicabile a

seconda dei materiali oggetto della stampa. Per questa tesi è stato selezionato il processo di stampa 3d per estrusione di paste. In questo tipo di approccio polveri del materiale di interesse, generalmente metalliche o ceramiche, sono misturate ad una soluzione polimerica composta da un solvente ed un binder polimerico che funge da legante. La soluzione risultante è quindi inserita in un cilindro e sospinta da un pistone ad uscire da un ugello. Dopo lo stampaggio dei pezzi è necessario un trattamento termico che permetta la perdita della componente polimerica e la sinterizzazione dei pezzi stampati.

La Termoelettricità

La termoelettricità è quella branca della fisica che studia la conversione diretta del calore in energia elettrica e viceversa. L'effetto Seebeck, l'effetto Peltier e l'effetto Thomson sono gli effetti su cui la termoelettricità si basa. In particolare, l'effetto Seebeck relaziona il differenziale di potenziale elettrico generato con la differenza di temperatura applicata. Le due differenze sono proporzionali e il coefficiente di proporzionalità è il coefficiente di Seebeck α .

Fisicamente ciò che succede è che quando una differenza di temperatura è applicata alle estremità di un materiale, i portatori di carica (elettroni o lacune) si muovono verso l'estremità più fredda. Convenzionalmente quando i portatori di carica sono elettroni, quindi negativi, e conseguentemente si parla di semiconduttori di *tipo n* il coefficiente di Seebeck è considerato negativo; per conduttori di *tipo p*, dove i vettori elettronici sono lacune positive, α è convenzionalmente positivo.

La figura di merito adimensionata ZT è la principale indicazione delle prestazioni dei materiali termoelettrici. Essa è esposta dall'Equazione (2.3).

$$ZT = \frac{\alpha^2 \sigma}{\kappa} T = \frac{\alpha^2}{\rho \kappa} T \quad (2.3)$$

Dove: α è il coefficiente di Seebeck, σ è la conduttività elettrica, κ è la conducibilità termica, ρ la resistività elettrica e T è la temperatura di applicazione. $\alpha^2 \sigma$ è anche definito come "Power Factor" (PF).

L'efficienza termoelettrica è proporzionale alla figura di merito ZT e anche alla differenza di temperatura tra le estremità. Per cui maggiori ZT e ΔT , più efficiente il materiale termoelettrico. ZT è direttamente proporzionale, come si vede dall'espressione che lo riporta, alla conduttività elettrica e inversamente alla conducibilità termica. Materiali efficienti sono quindi quelli che presentano caratteristiche di discreti conduttori elettrici (nella maggior parte dei casi, semiconduttori) e allo stesso tempo isolanti o cattivi conduttori termici.

In realtà, le leggi della fisica prevedono un andamento quasi proporzionale tra la conducibilità elettrica e quella termica. La conducibilità termica consta, infatti, di una componente elettrica (κ_{el}) e di una componente relativa al reticolo cristallino (κ_{lat}). La componente elettrica è direttamente proporzionale (legge di Wiedemann–Franz) alla conducibilità elettrica. κ_{lat} , invece, non ne è dipendente. Di conseguenza materiali con proprietà termoelettriche interessanti sono quelli che presentano il giusto compromesso tra le proprietà sopra discusse.

Generatori termoelettrici (TEGs)

I generatori termoelettrici sono dispositivi allo stato solido, in grado di sfruttare le proprietà termoelettriche dei materiali, sfruttando effettivamente l'effetto Seebeck per la produzione di elettricità. Un modulo termoelettrico prevede l'accoppiamento tra un materiale di *tipo p* e uno di *tipo n*, come mostrato in "Figure 2.2". Un generatore termoelettrico prevede l'affiancamento di numerosi moduli termoelettrici.

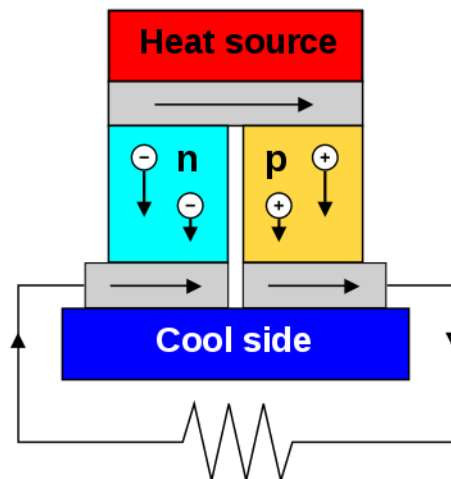


Figure 2.2: Structure of a TEG module
(Source: www.wikipedia.org)

I vantaggi principali di questi dispositivi sono dati dal fatto che, non sono presenti parti in movimento e quindi non necessitano di fluidi lubrificanti e la manutenzione necessaria è limitata. Convertono direttamente il calore in elettricità senza necessità di step intermedi. Hanno una "life-time" elevata, specialmente quando la differenza di temperatura a cui operano è costante. Sono versatili, in quanto esistono dispositivi per la generazione di pochi microwatt fino a dispositivi per la produzione di alcuni kilowatt.

I TEGs sono classificati in base alla fonte di calore che trasformano in energia elettrica e alle condizioni di utilizzo. In particolare, una possibile classificazione è la seguente:

Generazione di elettricità in ambienti estremi, come zone di difficile o impossibile accesso. Come lo spazio. In queste situazioni l'affidabilità (data la manutenzione pressoché impossibile) e l'efficienza sono le caratteristiche più importanti. Il costo dei materiali, invece, lo è meno.

Recupero del waste-heat, in applicazioni industriali e automobilistiche. In questo caso basso costo ed elevata reperibilità dei materiali sono caratteristiche fondamentali, quanto le performance termoelettriche.

Produzione domestica decentralizzata, per il recupero del calore in processi domestici, soprattutto in paesi in via di sviluppo ma anche nei paesi più industrializzati.

Micro-generazione per sensori e dispositivi microelettronici, dove vengono prodotti solo microwatt di potenza elettrica.

TEGs solari, che funzionano sfruttando il calore irradiato dal sole.

Materiali termoelettrici tradizionali

I materiali più tradizionalmente utilizzati sono:

- Tellururo di Bismuto (Bi_2Te_3)
- Tellururo di Piombo (PbTe)
- Silicio/Germanio (SiGe)
- Sistemi ternari e quaternari a base di Bismuto, Antimonio, Tellurio, Argento, Selenio e Cesio
- Skutteridi: minerali a base di Cobalto e altri elementi.

In generale i principali inconvenienti relativi a questi materiali sono relativi alla scarsità degli elementi in questione e quindi al loro elevato costo.

Per sopperire a questi inconvenienti alcuni dei materiali più futuribili e che si candidano a giocare un ruolo da protagonisti nei prossimi anni sono: FeSi_2 , ZnO e Mg_2X (dove $\text{X}=\text{Si}$, Ge , Sn). Il siliciuro di magnesio (Mg_2Si), in particolare, è il materiale oggetto di questa tesi. Diversi autori hanno già presentato performance termoelettriche (descritte da ZT) comparabili ai più tradizionali materiali, affiancando a ciò una disponibilità in crosta terrestre di alcuni ordini di grandezza superiore.

Il Siliciuro di Magnesio

Il siliciuro di magnesio è un composto intermetallico a base di silicio e magnesio che si sistemano in un sistema cubico dove il silicio occupa gli angoli e i centri delle facce del reticolo e il magnesio si pone internamente alla cella elementare, con configurazione generale detta 'anti-fluorite', come mostrato in "Figure 3.1".

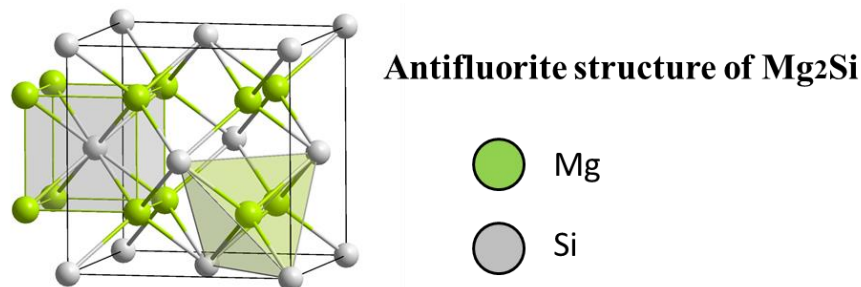


Figure 3.1: Antifluorite structure of magnesium silicide
(Source: www.wikipedia.org)

Questo materiale è intrinsecamente un semiconduttore di *tipo n* e oltre a un discreto comportamento termoelettrico combina proprietà fisiche, meccaniche e chimiche interessanti. In particolare, la sua bassa densità (1.99 g/cm^3) lo rende particolarmente interessante per applicazioni in ambito automobilistico. Mg_2Si è anche discretamente resistente all'ossidazione e inizia ad ossidare, formando ossido di magnesio (MgO) a temperature superiori a $465 \text{ }^\circ\text{C}$. MgO riduce sensibilmente le proprietà elettriche del siliciuro di magnesio e conseguentemente anche le sue proprietà termoelettriche. La formazione di ossido è anche una delle principali criticità legate alla sua sintesi. Questo è dovuto alla estrema affinità del magnesio con l'ossigeno anche a temperatura ambiente.

La reazione di formazione tra magnesio e silicio per dare Mg_2Si è una reazione esotermica ($\Delta H = -77.3 \text{ kJ/mol}$) e presenta inoltre energia libera di formazione negativa. Per la sintesi di questo materiale, le criticità più importanti sono date dal fatto che magnesio e silicio presentano un'elevata differenza tra i loro punti di fusione e in particolare il Mg presenta addirittura un punto di ebollizione (1110°C) inferiore al punto di fusione del Si (1414°C). Ciò, fa sì che sia conveniente la sintesi del materiale promuovendo la reazione allo stato solido dei costituenti. Gli altri aspetti che rendono difficoltoso l'ottenimento sono: la formazione di ossido di magnesio (praticamente inevitabile anche operando in atmosfera controllata); l'elevata volatilità del magnesio che evapora facilmente forzando ad operare in condizioni di difetto di magnesio.

Le principali tecniche che consentono la fabbricazione del materiale possono essere sia di fusione (in contenitori sigillati per ridurre l'evaporazione del magnesio) e sia di reazione allo stato solido (partendo dalle polveri dei costituenti). In particolare, le sintesi allo stato solido possono essere: alligaggio meccanico, Spark Plasma Sintering, applicazione di energia tramite microonde o di energia termica. Spesso questi processi vengono anche combinati.

Per questo lavoro di tesi è stato scelto di combinare l'azione meccanica, "milling" in un mulino a sfere ad alta energia, in atmosfera di argon, con successivo trattamento termico atto a promuovere la reazione di formazione. In letteratura sono già stati presentati lavori per cui Mg_2Si sia stato ottenuto solamente tramite alligaggio meccanico. Ciò avviene solamente dopo decine di ore di milling e in molti casi anche dopo 60 ore la reazione non è completa. Un approccio più diffuso consiste in: il milling è ridotto a poche ore ed è seguito da trattamento termico in atmosfera inerte. Il vantaggio di questo accoppiamento sta nel fatto che gli impatti ad alta energia tra le polveri con le sfere e tra di esse, durante il milling, riducono l'energia di attivazione della reazione. Questo perché:

- La dimensione delle particelle è ridotta, aumentando quindi l'area superficiale di contatto tra di esse;
- La distanza tra le particelle è minimizzata per i continui impatti;
- L'energia interna è aumentata per l'introduzione di difetti e stress.

Tutto ciò porta ad un aumento dell'energia interna del sistema ed una conseguente diminuzione dell'energia di attivazione della reazione. Ciò è schematizzato dalla "Figure 3.5".

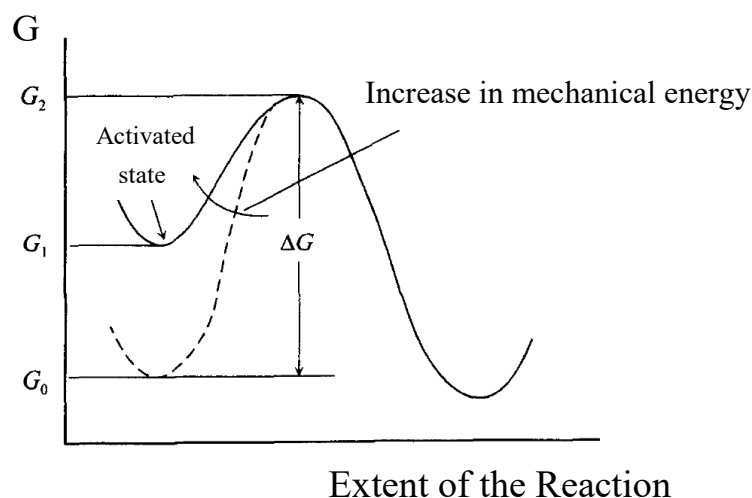


Figure 3.5: Increase of internal energy by mechanical action, resulting in decrease of the activation energy of the formation reaction of Mg_2Si .

(Modified from [30]: L. Lu et al, Formation of nanocrystalline Mg_2Si and Mg_2Si dispersion strengthened Mg-Al alloy by mechanical alloying, 1998)

Praticamente, una riduzione dell'energia di attivazione significa che la reazione:
 $2 \text{Mg} + \text{Si} \rightarrow \text{Mg}_2\text{Si}$, avviene a temperature più basse quanto maggiore è l'energia meccanica applicata.

Possibilità di drogaggio

Il siliciuro di magnesio è, infine, estremamente interessante perché le sue proprietà di semiconduttore *n* possono essere aumentate tramite drogaggio con elementi come antimonio, bismuto e stagno. Ed è possibile ottenere semiconduttori di *tipo p* tramite drogaggio con elementi come calcio e argento.

Sintesi del siliciuro

Sperimentalmente si è proceduto nel seguente modo:

Una miscela stechiometrica (2 Mg, 1 Si) delle polveri dei costituenti è stata macinata per 5 e 10 ore (tempo effettivo) in un mulino a sfere ad alta energia (Retsch® PM100). 30 minuti di milling sono stati alternati a 5 minuti di pausa per evitare sovrappressione e surriscaldamento all'interno del mulino. Da notare, inoltre, che il magnesio è stato conservato in una glovebox sotto atmosfera di argon. Dentro la quale sono avvenute tutte le manipolazioni e il caricamento delle polveri nel contenitore di milling, assicurando quindi che il milling sia stato condotto in atmosfera inerte.

Gli altri parametri sono: -velocità = 400 rpm; -rapporto massa sfere : massa polvere = 10 : 1; - le sfere hanno un diametro di 20 mm e sono costituite dal minerale Agata, così come le pareti del "contenitore di macinatura"; -è stato utilizzato esano come fluido di processo per evitare attaccamento del materiale più duttile (magnesio) alle pareti del contenitore e alle sfere.

Successivamente al milling, analisi DSC è stata condotta sulle polveri macinate e non macinate. I risultati sono mostrati in "Figure 5.10". La reazione di formazione, come detto in precedenza, è esotermica. L'analisi DSC condotta, infatti, mostra alcuni chiari picchi esotermici.

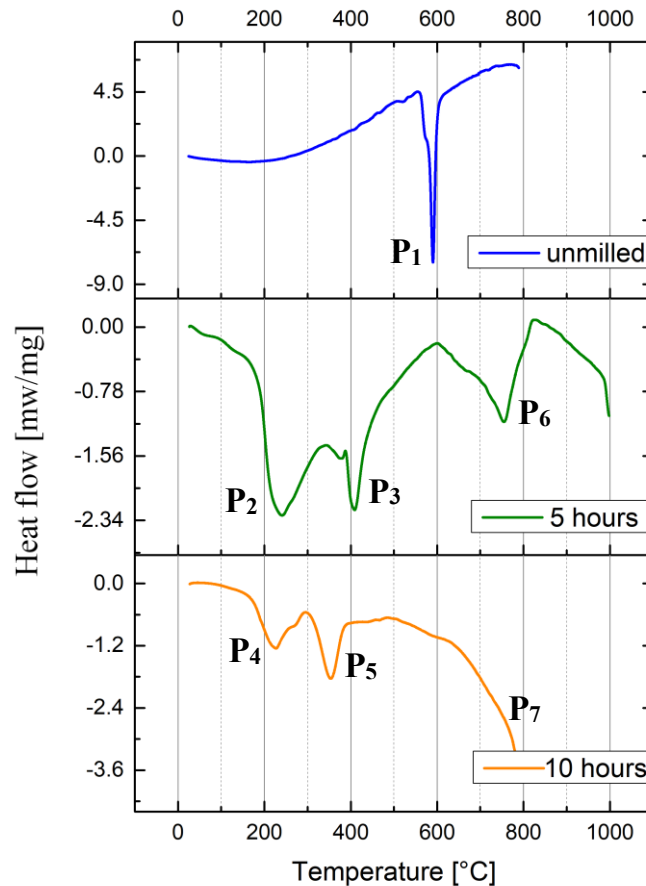


Figure 5.10: DSC results comparison

Per quanto riguarda la polvere non macinata è visibile un chiaro e ben definito picco esotermico P₁ a circa 590 °C, indice dell'avvenimento della reazione di formazione del siliciuro a quella temperatura. Per quanto riguarda le polveri macinate, invece, i picchi relativi alla reazione di formazione sono meno definiti, più larghi e sono spostati verso temperature via via più basse con l'aumento del tempo di milling (P₂, P₃ e P₄, P₅). I picchi P₆ e P₇ sono probabilmente riferibili alla formazione di nitrato di magnesio (l'analisi è stata condotta in atmosfera di azoto), anche se questa ipotesi non è stata verificata sperimentalmente.

Con base su questi dati le polveri non macinate e quelle macinate per 5 ore sono state soggette ad un trattamento termico. In particolare, il trattamento è avvenuto in un forno tubolare, con temperatura che in 15 minuti è stata innalzata fino alla temperatura di set point (590 °C per la polvere non macinata, 410 °C per quella macinata); temperatura che è stata mantenuta per 75 minuti lasciando poi raffreddare fino a temperatura ambiente, prima di estrarre le polveri.

Per quanto riguarda le polveri macinate sono state sperimentate tre diverse atmosfere inerti (vuoto, azoto e argon) mentre la polvere non macinata è stata trattata solo in atmosfera di azoto. Dall'analisi di diffrazione ai raggi x (risultati mostrati in "Figure 5.22" per quanto riguarda le polveri macinate) si evince che la formazione nel siliciuro non avviene neanche in minima parte in seguito al processo di milling, ma solamente successivamente al trattamento termico. In ogni caso una percentuale (in massa) bassa ma non trascurabile di MgO (mediamente 5 %) è stata rilevata in seguito ai trattamenti termici nelle varie atmosfere testate. Percentuale che prima del

trattamento si attestava a valori inferiori all'1 %. Nelle tre atmosfere testate inoltre è sempre stata rilevata una percentuale di silicio non reagito considerevole (tra il 10 e il 13 %), indicando che è avvenuta una perdita di magnesio (probabilmente per evaporazione) che ha costretto ad operare in difetto di tale elemento.

I picchi sono stati identificati nel seguente modo:

- Silicio
- Magnesio
- △ Siliciuro di magnesio
- * Ossido di magnesio

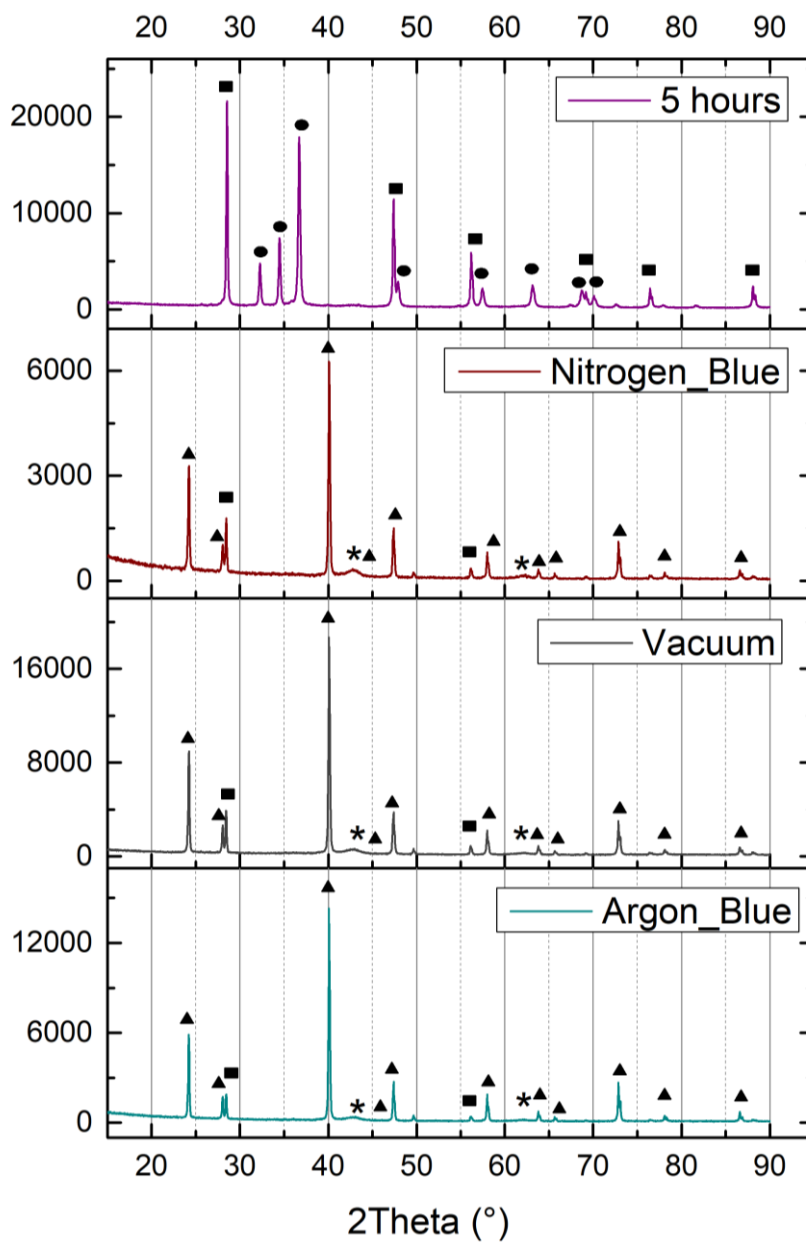


Figure 5.22: XRD patterns of powder milled 5 hours, before any thermal treatment and powder (previously milled 5 hours) annealed in the three different atmosphere tested (N_2 , argon and vacuum)

Tali analisi sono anche state affiancate da spettroscopia Raman e IR per supportare ulteriormente i dati ottenuti e microscopia SEM per analizzare la morfologia e dimensione delle particelle, risultati che non sono riportati in questo riassunto.

Per quanto riguarda le polveri non macinate, le analisi hanno provato l'effettiva formazione di siliciuro dopo trattamento termico a 590 °C. Insieme a Mg₂Si come fase principale sono stati rilevati ossido di magnesio (4-5 % in massa) e silicio non reagito (3-4 % in massa).

Stampaggio 3d delle polveri di silicio e siliciuro di magnesio

La seconda parte del lavoro sperimentale è consistita nello stampaggio 3d per estrusione di una pasta del siliciuro prodotto (utilizzato il siliciuro prodotto per macinatura di 5 ore con successivo trattamento termico in atmosfera di azoto).

Come primo passo è stato condotto uno studio preliminare utilizzando sola polvere di silicio (la stessa che è stata utilizzata come materia prima per la sintesi del siliciuro). L'obiettivo di questo studio è stato quello di individuare i materiali (in particolare solventi e leganti polimerici) più consoni e promettenti. Una pasta estrudibile consta nella mistura delle polveri del materiale in oggetto, con un solvente ed un legante polimerico. La pasta viene inserita in una siringa (per quanto riguarda la stampante utilizzata in questo lavoro), che viene a sua volta inserita in un cilindro. Un pistone applica una forza costante ma regolabile forzando quindi la pasta a fuoriuscire dall'ago della siringa (ugello). Il movimento su tre assi del piatto su cui avviene la stampa permette l'ottenimento dei pezzi desiderati.

Durante lo studio preliminare numerosi materiali sono stati testati e sono riassunti in "Table 6.1".

Table 6.1: Lists of the experimented materials

| SOLVENTS | BINDERS | ADDITIVES |
|-------------------------------------|--|------------------|
| Ethanol Xylene Dodecanol | Ethyl cellulose (EC) Polystyrene (PS) | Oleic Acid |
| Acetone Dimethylacetamide (DMAc) | Cellulose acetate (CA) | Oleic Acid |

I principali parametri testati sono stati: la percentuale di legante polimerico disciolto nel solvente organico e la proporzione tra soluzione polimerica e polvere. Alla fine dello studio preliminare i materiali selezionati sono stati: -xilene come solvente; polistirene ed etilcellulosa come leganti. Pezzi stampati con le formulazioni più promettenti (3 di PS in xilene e 2 di EC in xilene) state sottoposte ad analisi DSC-TGA. Questo, per studiare la temperatura di de-binding. Come spiegato in precedenza, infatti, i pezzi stampati devono essere soggetti ad un trattamento termico a due step: il primo per eliminare il legante polimerico e il secondo per la sinterizzazione del pezzo. La "fuoriuscita" del polimero è un processo endotermico a cui

corrisponde contestualmente una perdita di massa. Due parametri facilmente riscontrabili tramite analisi DSC-TGA. I risultati ottenuti (temperatura di de-binding del polistirene e dell'etilcellulosa) sono riassunti in "Table 6.14".

Table 6.14: Resume of the deduced Tbo

| | |
|-----------------|--|
| PS formulations | $T_{bo} \sim 460-470 \text{ }^{\circ}\text{C}$ |
| EC formulations | $T_{bo} \sim 360 \text{ }^{\circ}\text{C}$ |

Stampaggio del siliciuro

Delle 5 formulazioni selezionate, la più promettente è stata utilizzata come base per lo stampaggio del siliciuro. Il rapporto soluzione : polvere è stato modificato e adattato al nuovo materiale. Purtroppo, data la scarsità di siliciuro a disposizione, non è stato possibile ottimizzare la stampa, anche se comunque i risultati ottenuti (in termini di definizione e precisione dei pezzi stampati) sono stati complessivamente soddisfacenti.

Per quanto riguarda il post-trattamento trattamento termico (avvenuto in vuoto), diversi parametri sono stati sperimentati. Come detto in precedenza, la temperatura di de-binding polimerico è stata determinata sperimentalmente. Gli altri parametri importanti per questa fase sono: le varie rampe di riscaldamento, il tempo di mantenimento alla temperatura di de-binding e alla temperatura di sinterizzazione e la temperatura di sinterizzazione stessa. Sono stati fatti diversi tentativi, ma nessuno di questi ha portato alla consolidazione sperata dei pezzi. In particolare, i primi tentativi sono stati fatti raggiungendo una temperatura massima di 800 °C (per limitazioni operative del foro utilizzato). Un successivo ed ultimo tentativo è stato fatto grazie all'utilizzo di un altro forno che ha permesso il raggiungimento di una temperatura più elevata (950 °C), considerata più consona al materiale in oggetto, essendo circa l'87 % della temperatura di fusione dello stesso. Il profilo di temperatura utilizzato è riassunto in "Figure 6.39".

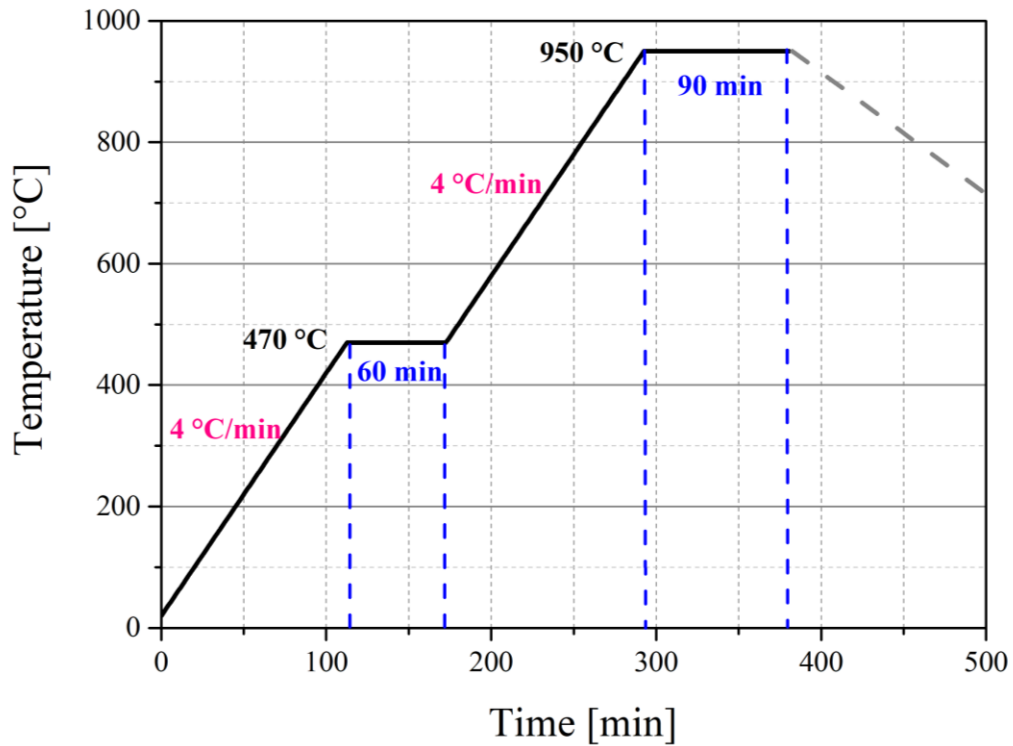


Figure 6.39: Scheme of the temperature perfil used for the last sintering attempt.

Anche in questo caso, tuttavia, il consolidamento meccanico dei pezzi non è avvenuto rendendo quindi impossibili successive caratterizzazioni elettriche o termoelettriche.

I risultati dell'analisi di diffrazione ai raggi x, effettuata in seguito all'ultimo tentativo, hanno parzialmente chiarito quest'aspetto. Durante il trattamento termico (effettuato in vuoto), una grande quantità di forsterite (Mg_2SiO_4) si è formata, la quantità di ossido di magnesio presente è aumentata e contestualmente non è stata più rilevata la presenza del silicio che quindi si è trasformato in altro durante il trattamento.

1 Introduction

One of the most important today challenge is a more sustainable and efficient use of resources. Climate change, environmental pollution and resources depletion are issues that cannot be avoided anymore. The overall world population is constantly increasing and consequently the resource demand is growing too. As an example, it's expected that the world's power demand will rise 60 % by 2030. However, electricity still mainly comes from non-renewable sources. Fossil fuels and nuclear processes represent approximately 90 % of the world's electricity production sources. [1]

Beside this, it must be considered that in many sectors low-efficient processes very often leads to the waste of a large amount of resources and energy. For instance, a tremendous amount of heat is daily produced in industry and in the transportation sector, but a big percentage is not exploited; it is dissipated as waste heat into the environment.

This large amount of waste heat, though, can be exploited and directly converted into electricity by thermoelectric (TE) solid-state generators. TE materials are, in fact, able to convert thermal energy into electricity. The thermoelectric effect is that phenomena by a difference of temperature (ΔT) across the material creates an electric potential (ΔV) and vice versa. The appearance of an electrical voltage caused by a temperature gradient is named "Seebeck effect" [2].

In this context, this thesis proposes the development of eco-friendly printable thermoelectric materials; they may be used in a very broad field of applications and hence, effectively answer to some of the presented issues. Typically, this kind of devices are based on material such as Tellurium (Te) and Germanium (Ge) that are scarce or Lead (Pb) that is toxic.

The aim of this project is to develop Silicon (Si) and Magnesium (Mg) based TE materials. Si and Mg are abundant and non-toxic elements. The intermetallic compound magnesium silicide (Mg_2Si) presents a positive combination of chemical and physical properties such as lightweight (density: 1.99 g/cm³), high melting point (1102 °C) and oxidation resistance in the application temperature field. In addition, the TE properties good can be significantly enlarged by doping. Values of $ZT_{max}=0.7$ up to $ZT_{max}=1.5$, when doped, have been already reported by *Liu et al* [3].

The dimensionless figure of merit ZT (better described in "Chapter 2") is used as a measure of the thermoelectric performance. It is function of the Seebeck coefficient α , of the electrical conductivity σ and of the thermal conductivity κ . It is also function of the temperature. The higher the figure of merit, the better the TE performances. Considering that the "last generation" of Te-Pb based bulk thermoelectrics achieved ZT of 1.8 at about 850 K (577 °C), the previously presented values of ZT are very promising values. [4, 5]

Moreover, both *n-type* and *p-type* features are achievable doping Mg-Si based compounds. Mg_2Si is intrinsically a *n-type* semiconductor and its electrical properties can be enhanced by doping with elements such as Al, Bi and Sb. However, doping with Ca or Ag leads to obtain a *p-type* semiconductor. All these reported characteristics make Mg_2Si a very promising material for applications at intermediate temperatures, in the range of 500 to 800 K.

Magnesium silicide fabrication is challenging, because the melting point of Si (1414 °C) is much higher than the boiling point of Mg (1090 °C), so it is not easy to have both Mg and Si liquid at the same conditions; that leads to difficulties in using traditional and easy-to-use techniques such as arc melting. Magnesium silicide could be synthesized by different

techniques, usually starting from powders of the components. Mechanical Alloying (MA), Hot Pressing (HP), Spark Plasma Sintering (SPS) and Microwave Heating are effective methods that consent to obtain the Mg_2Si phase.

In this work of thesis, it was decided to combine mechanical action, using a planetary ball mill, followed by a thermal treatment, in controlled atmosphere, to complete the formation of the alloy. An effective combination of parameters in term of: -milling parameters; -annealing temperature, atmosphere and time was studied to develop an efficient and effective process. Magnesium silicide was successfully obtained with the indicated methods, starting from powder constituents.

The second part of the thesis is about the 3D printing of the obtained magnesium silicide. Additive manufacturing (AM) or 3D printing is widely known to be a very versatile method and it allows to obtain complex objects in a relatively short time. In the specific case, it may be a route suitable for mass-production and low-cost fabrication of TEGs (thermoelectric generators).

Among other 3D printing techniques, an extrusion-based technology was used. An extrudable TE paste is prepared blending the TE powder with a viscous liquid solution. The components of the solution are a solvent and a polymeric binder. In this work, formulation of a paste was studied to obtain optimized printing and after-printing behaviour. The critical parameters are the proportions powder to solution and the composition of the solution. A preliminary study was performed on silicon commercial powder and then adapted to the magnesium silicide synthesized. Notice that the manufacture of Mg_2Si -based pastes is challenging because of its reaction with water. This limited the use of solvents and binders. Some water-free formulations were experimented, and different solvents and binders tested. Mg_2Si was successfully printed using a formulation containing xylene as a solvent and polystyrene as a binder.

The printed pieces are then, subject to a two-steps thermal treatment, in order to achieve the de-binding of the polymeric binder and mechanical consolidation of the pieces. However, even though various combinations of parameters were tested the post-processing didn't lead to the hoped results. The sinterization of the pieces didn't succeed; consequently, it wasn't possible to measure the thermoelectrical properties of the fabricated devices.

Despite this, this work presents an effective procedure for Mg_2Si fabrication and its 3d printing by paste-extrusion method. This is considered as the innovative contribution of this thesis: were not found in literature, in fact, any studies for 3d printing of Mg_2Si -based devices; that is so a new research topic. Moreover, even though the post-processing didn't lead to mechanical consolidation of the pieces, the tested combinations of parameters are important piece of information for further works on this subject.

1.1 Thesis Structure

The next chapters of this Master Thesis are structured as follows:

The aim of **Chapters 2, 3 and 4** is to give the reader an overview about the theoretical principles on which this work is based and to show briefly the analytical instrumentations used to analyse and characterize the outputs of the experimental part.

In particular:

- **Chapter 2** deals about some theoretical aspects of thermoelectricity: the thermoelectric effects (Seebeck, Peltier and Thomson), the Seebeck coefficient, the dimensionless figure of merit ZT and the thermoelectric efficiency. *N-type* and *p-type* thermoelectric materials are also described. Then the chapter gives an overview about the practical applications of thermoelectric materials: the thermoelectric generators (TEGs) and some fields of application. It concludes dealing about some of the most commonly used and performing thermoelectrics, emphasizing their disadvantages and the reasons that limited their diffusion.
- **Chapter 3** gives an overview about magnesium silicide. The materials proposed by this work such as a novel, eco-friendly and performing TE material. Its physical, chemical and thermodynamic properties are presented especially focusing on that ones that could influence the synthesis of the material and the devices production. Then, the state of the art about fabrication techniques and doping is presented, to provide a small review regarding the researches and manuscripts found in literature.
- **Chapters 4** describes the analytical techniques used in this work, in specific:
 - Scanning Electron Microscopy (SEM)
 - X-ray Diffraction (XRD)
 - Raman Spectroscopy
 - Fourier-Transform Infrared Spectroscopy (FT-IR)
 - Differential Scanning Calorimetry (DSC)
 - Thermo-gravimetric Analysis (TGA)

Chapters 5 and 6 are about the experimental part of the thesis. The synthesis of Mg_2Si , its 3d printing and electrical characterization are described.

In detail:

- **Chapter 5** regards the fabrication route of magnesium silicide, obtained by ball milling followed by the application of a thermal budget. The description of the used instrumentation, with a focus on the ball milling/mechanical alloying process, is also presented. The exploration and comparison of different inert atmospheres are described and the results of the analysis, that proved the success of the alloy formation, showed.

- **Chapter 6** deals about the printing of the fabricated magnesium silicide, showing the preliminary study performed using only silicon powder. A short description of the used printer is also provided. Then, it follows the presentation of the post-process treatments.

Chapter 7 concludes the thesis, presenting and summarizing the overall conclusions.

The experimental work has been performed in the materials department of the “Faculdade de Ciências e Tecnologia” of the “Universidade Nova de Lisboa” (FCT NOVA) at the campus of Caparica, Portugal. The practical work was also done, in collaboration with Politecnico di Torino (Italy), “CTN – Campus Tecnológico e Nuclear” of the “Instituto Tecnico de Lisboa” (Portugal) and “Universidade of Aveiro” (Portugal).

2 Thermoelectricity

Thermoelectricity studies the direct conversion of heat into electricity and vice versa. Two related mechanisms, the Seebeck effect and the Peltier effect are the basis of thermoelectricity. These phenomena happen in every material; however, they are appreciable only in the so-called thermoelectric materials.

2.1 Thermoelectric effects [6, 7]

The **Seebeck effect** is the first thermoelectric phenomenon observed in 1821 by Thomas Johann Seebeck. For many years it was considered the starting point of thermoelectric studies. However, the history of thermoelectricity starts earlier, in 1794 with Alessandro Volta [6]. The Italian scientist already in that year made some experiments, finding a correlation between an applied temperature gradient on a metallic spire with the formation of electricity. Seebeck in 1821 observed the movement of a compass needle when two dissimilar materials were joined together and were subjected to a difference of temperature. He firstly associated this behaviour with the earth's magnetic field. Two years later Hans Christian Ørsted understood that it was due to the flowing inside the material of electrical carriers. The voltage is proportional to the gradient of temperature and the constant of proportionality is the **Seebeck coefficient α** , as shown in Equation (2.1).

$$\Delta V = -\alpha \Delta T \quad (2.1)$$

In 1834 Jean Charles Athanase Peltier observed the formation of a difference of temperature, not referable to the Joule effect, while two conductive materials were joined and crossed by electricity, this phenomenon is called **Peltier effect**. It is the reverse counterpart of the Seebeck effect. The heat is generated or absorbed according the direction of the current; it is also proportional to the current by a proportionality coefficient called **Peltier coefficient**.

Willian Thomson in 1851 correlated Peltier and Seebeck effects and propose a third thermoelectric effect: the so-called **Thomson effect**. When a homogeneous conductive material has his extremities at two different temperature T_1 and T_2 and an electric current is flowing along the material, then it will absorb or produce heat according to the current direction.

The Seebeck coefficient α of a material gives the magnitude of the thermoelectric voltage that forms by the Seebeck effect. The SI unit is Volt per Kelvin (V/K), even though more often is given in microvolt per Kelvin ($\mu\text{m/K}$). For metals α values are typically 1-10 $\mu\text{m/K}$ while semiconductors can present α values up to 10^{12} - 10^{13} $\mu\text{m/K}$. The Seebeck coefficient is not constant along the temperature and it is influenced by many factors. It is expressed by Equation (2.2).

$$\alpha = \frac{8 \pi k_B^2}{3 e h^2} m^* T \left(\frac{\pi}{3n} \right)^{2/3} \quad (2.2)$$

Where:

- k_B is the Boltzmann constant,
- m^* is the density of states effective mass,
- h is the Planck constant,
- n is the carrier concentration,
- e is the electron charge

2.2 P-type and n-type semiconductors [8]

When a difference of temperature is applied over a material, the electrical carriers (electrons or holes) move from the hot extremity to the cold one. So, a voltage creates along the material. Consequently, an electric field is created too. P-type semiconductors that presents positive electrical carriers (holes) have positive values of α , while n-type ones have negatives values of α . That is because from a vector point of view the electric field points from the higher voltage to the lower one. The gradient of temperature is oriented from the lower temperature to the higher. “Figure 2.1” shows the described behaviour.

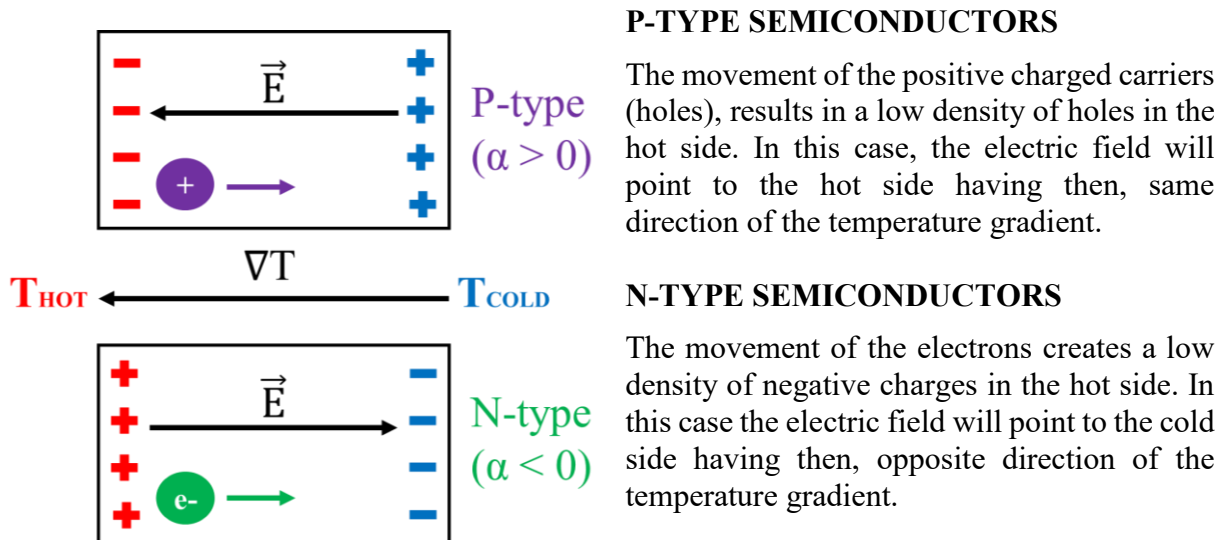


Figure 2.1: Representation of p-type ($\alpha > 0$) and n-type ($\alpha < 0$) thermoelectric semiconductors

In order to exploit the voltage that creates it is necessary to couple the n-type and the p-type: this is at the base of the functioning of thermoelectric generators as explained in paragraph 2.5.

2.3 ZT Figure of merit and TE efficiency [8, 9]

ZT is a dimensionless figure of merit, proposed in 1909 by Edmund Altenkirch. It is reported in Equation (2.3) and determines in large part the TE performance of a material.

$$ZT = \frac{\alpha^2 \sigma}{\kappa} T = \frac{\alpha^2}{\rho \kappa} T \quad (2.3)$$

Where:

- α is the Seebeck coefficient
- σ is the electrical conductivity
- ρ is the electrical resistivity
- κ the total thermal conductivity
- The product $\alpha^2 \sigma$ is also defined as Power Factor (PF).

In addition, for power generation, the thermoelectric efficiency η is defined by combining the Carnot efficiency ($\Delta T/T_{hot}$) and the figure of merit ZT , as shown in Equation (2.4).

$$\eta = \frac{\Delta T}{T_{hot}} \frac{\sqrt{1 + ZT_{avg}} - 1}{\sqrt{1 + ZT_{avg}} + \frac{T_{cold}}{T_{hot}}} \quad (2.4)$$

Where:

- T_{hot} and T_{cold} are the temperatures of the hot and cold ends
- ΔT the difference of temperature
- ZT_{avg} the average figure of merit (ZT at the T_{avg})

Increasing TE efficiency requires both high ZT values and a large temperature gradient across the material. The challenge in creating high ZT thermoelectric materials is in achieving simultaneously high Power Factor (PF) and/or low thermal conductivity (κ), as visible from Equation (2.3). However, obtaining these results at the same time is really challenging. An increase of PF is usually obtained by doping the material; doping, however, leads to an increase of σ and, as suggested by Equation (2.2), to a decrease of α .

Moreover, usually, electrical and thermal conductivity go hand in hand. The thermal conductivity κ , in fact, presents two contributions: a contribution from lattice vibrations and an electronic one, as reported in Equation (2.5).

$$\kappa = \kappa_{LAT} + \kappa_{EL} \quad (2.5)$$

The electronic contribution increases linearly with the electrical conductivity as shown by the Wiedemann–Franz law (Equation (2.6)).

$$\kappa_{EL} = \sigma L T \quad (2.6)$$

Where: L is the Lorentz number, T is the temperature and σ the electrical conductivity.

Lattice thermal conductivity κ_{LAT} is the only parameter that is independent of carrier concentration. Then, strategies to enhance the thermoelectric performance, by decreasing the thermal conductivity, include the development of materials with intrinsically low thermal conductivity, solid-solution alloying and the realization of nanostructured materials.

According to ZT and efficiency, TE materials can be divided into three generations. In the first, ZT is about 1.0, and the devices can operate at an efficiency of approximately 4-5 %. The

second generation starting in the 1990s, ZT was pushed to about 1.7, by the introduction of nanostructures; the efficiency reached 11-15 %. The third generation of bulk thermoelectrics has been investigated recently; new concepts led to obtain ZT of 1.8 and even higher. The predicted device conversion efficiency increases up to 15-20 %. These high- ZT devices, as reported by *Champier* [10], are so far limited to laboratory applications. The currently best commercially available devices have a ZT of ~ 1 . However, many improvements have been made in the last decade and more are expected in the next years.

2.4 Thermoelectric generators (TEGs) [10]

A thermoelectric generator (TEG), is a solid-state device able to convert heat directly into electrical energy exploiting so, the Seebeck effect. TEGs are made of a set of thermoelectric (TE) modules and each TE module consists in many pairs of TE couples connected together electrically in series and thermally in parallel. A possible configuration of a TE module is a circuit consisting of two joined different thermoelectric materials (*n-type* and *p-type*) that form a TE pair. The structure of TE module is shown in “Figure 2.2”.

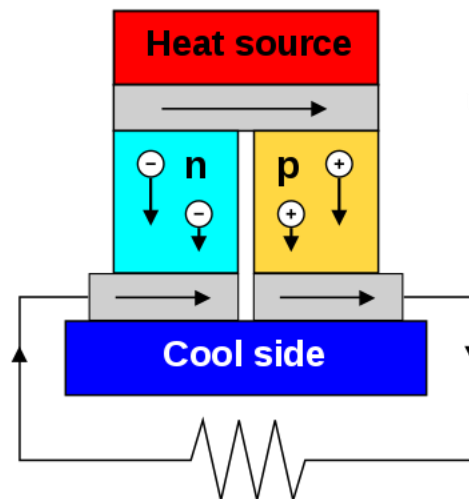


Figure 2.2: Structure of a TEG module
(Source: www.wikipedia.org)

The generated electrical current is introduced in the external circuit thanks to the movement to the cold side of -in the n-type semiconductor- electrons, and -in the p-type- holes. That makes possible the exploitation of the voltage generated after the application of a temperature gradient. The structure of a TEG is shown in “Figure 2.3”.

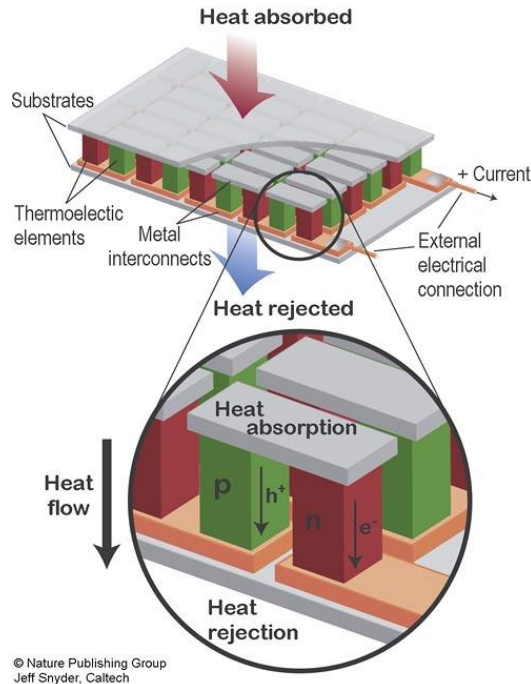


Figure 2.3: Structure of a TEG composed by many TE modules
(Source: www.thermoelectrics.caltech.edu)

TEGs present several advantages and big potentiality:

- The energy conversion is direct, with no intermediate step. Traditional heat engines, in fact, convert thermal energy into mechanical and then to electricity by using an alternator.
- There aren't involved moving parts and working fluids. It means less maintenance needed and so, lower maintenance cost. It also means noiseless functioning.
- They have a long lifetime, particularly when working at -more or less- constant heat sources.
- TEGs can be used for a big variety of applications: from microgeneration to kilowatts production.

Low efficiency and high cost, however, have been a barrier to mass development. Despite their clear advantages, TEGs are being limited to few applications such as space ones. In spatial applications TEGs reliability justified their use despite the high cost.

To overcome the disadvantages that limited the TEGs diffusion, researchers and manufacturers have tried find new solutions: improving ZT, increasing the operating range for working with higher temperature gradient and looking for low-cost raw materials. Efficiency is defined as the ratio of the electrical energy produced, to the energy entering, as heat, in the hot face. Efficiency expression was already presented in Equation (2.4), where it has to be considered that the figure of merit ZT should take in account the contribution of both p-type and n-type materials Seebeck coefficient as illustrated in Equation (2.7).

$$\alpha_{pn} = \alpha_p - \alpha_n \quad (2.7)$$

In the calculation of ZT, it also has to be considered the eventual differences in thermal (κ) conductivity and electrical resistivity (ρ) as shown in Equation (2.8).

$$ZT = \frac{\alpha_{pn}^2}{(\sqrt{\kappa_p \rho_p} + \sqrt{\kappa_n \rho_n})^2} T \quad (2.8)$$

“Figure 2.4” compares the Carnot efficiency with the TE efficiency in function of the most common values of ZT.

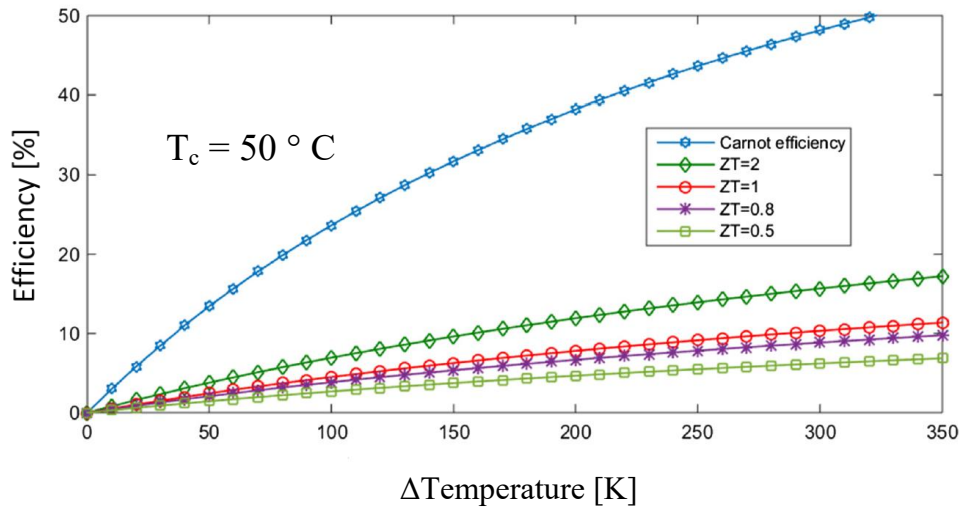


Figure 2.4: Comparison of Carnot efficiency with TEGs efficiency in function of ZT (Modified from [10]: D. Champier, *Thermoelectric generators: A review of applications*, 2017)

2.5 TEGs applications [10]

As it has been previously stated, many are the potential application fields of TEGs. Use conditions and nature of heat sources are two possible parameters to classify the possible applications. Champier [10] classified them into five categories:

1. electricity generation in extreme environments
2. waste heat recovery
3. decentralized domestic power and combined heat and power generation systems
4. micro-generation for sensors and microelectronic devices
5. solar TEGs

1. Electricity generation in extreme environments, remote areas and space

Electricity production in these environments, in which weather conditions can be extreme and access is limited or none, is a critical application that should satisfy strict specifications. It requires extremely reliable source of energy over long time and maintenance must be as low as possible.

Space industry used TEGs since the beginning of spatial exploration. Radioisotope thermoelectric generators (RTGs) provided electrical production to many satellites and probes sent to space in conditions in which sunlight wasn't enough to feed solar panels. RTGs showed a perfect solution for spatial applications due to low mass, high reliability and long lifetime (from few years up 30 years). In this case, clearly, the economic aspect is secondary: expensive materials can be used with no big issues.

2. Waste heat recovery

A key challenge in industry and transportations is to recover thermal energy lost or waste heat and convert it into electricity.

In industry in general, heat is often a by-product of many processes. Part of it is reused or converted into electrical power by steam turbines or engines, however most of the time it is released into the environment.

Automotive and more in general transportation industry, is one of the most attractive sector for waste heat recovery from TEGs. So far, only scarce solutions have been developed for waste heat recovering from exhaust gas of engines.

The FIAT Research Center estimated that on a small-medium gasoline engine, a TEG with a $ZT \approx 1.2$ with an efficiency of 4-5% may lead to a 6-7 g/km CO₂-emission reduction, a remarkable value for automotive manufacturers. Then, higher ZT values (2 or more) are welcome but not strictly necessary [11].

In these fields, the economic aspect is fundamental: only low-cost, abundant, non-toxic and performing materials can be serious candidates to mass production and gain a key role in industry and transportations.

3. Domestic TEG

In developing countries, a large amount of people doesn't have access to electricity grid. In these contexts, power production by decentralized autonomous systems is the only economically viable solution. Solar energy needs big storage capacity for periods without sunlight. TEGs, applied on cookers or stoves, may be a solution to provide power for small applications.

TEGs are not limited to the domestic use in developing countries but may find application in developed countries too. Heating production systems such as stoves or boiler can be heat source for TEGs.

4. Micro-generation for sensors and microelectronic devices

Thermoelectric generators may be used to produce low-power devices such as sensors. Intelligent sensors require only a hundred microwatts or few milliwatts. The power source must be compatible with the lifetime of the sensor. Sometimes batteries don't fulfil this specification, while TEGs can guarantee a longer lifetime.

5. Solar thermoelectric generator (STEG)

Solar thermoelectric generators use the heat from the sun as a heat source. The solar flux must be directly concentrated on the TE modules by mean of thermal, optical or classical solar concentrators otherwise the efficiency would be too low.

2.6 Traditional Thermoelectric Materials [12, 13]

Some of the most used and performing materials are the binary intermetallic semiconductor systems: Bi_2Te_3 , PbTe , SiGe . However, several authors [12, 13] already illustrated serious problems and limitations related to a further development of devices based on these materials. “Figure 2.5” lists the most used and investigated TE materials and some of their characteristics.

Bismuth Telluride (Bi_2Te_3)

Probably the most spread TE material is Bi_2Te_3 , for low temperature applications, up to 523 K. Modules based on Bi_2Te_3 are widely spread in industrial applications. Devices with $ZT = 1.1$, showed an efficiency of respectively 6.7 % and 9.5 % in the range 320 – 470 K and 270 – 470 K. A wide range of different devices is available: from small modules, with very low output powers for sensor applications (magnitude of mW), to TEGs with output powers of 1 kW or more. However, in terms of availability on the earth, Tellurium is a “limiting material”. Moreover, the price of this element has become very volatile. In this scenario, an increase in use of Tellurium based materials is not likely.

Lead telluride (PbTe)

PbTe is a very good material for thermoelectric generators (TEGs) in terms efficiency and durability in the temperature range up to about 823 K. Though, the considerations about Tellurium already presented, and the toxicity of Pb are elements that reduce considerably the potential of these materials.

Silicon-germanium (SiGe)

SiGe based modules present good performances in the temperature range between 1023 K and 1273 K. The application is, however, limited to specific applications such as spatial ones. The scarcity of germanium is a serious limitation to the mass application.

Ternary and quaternary systems

Recent approaches to high-performance bulk TE materials focus on ternary and quaternary chalcogenides such as $\text{Bi}_{2-x}\text{Sb}_x\text{Te}_{3-y}\text{Se}_y$, CsBi_4Te_6 , $\text{Ag}_n\text{Pb}_m\text{M}_n\text{Te}_{m+2n}$ ($M = \text{Sb}, \text{Bi}$). Other reaserches focused on materials called half-Heusler alloys. They present a general formula MNiSn , where $M = \text{Zr}, \text{Hf}, \text{Ti}$.

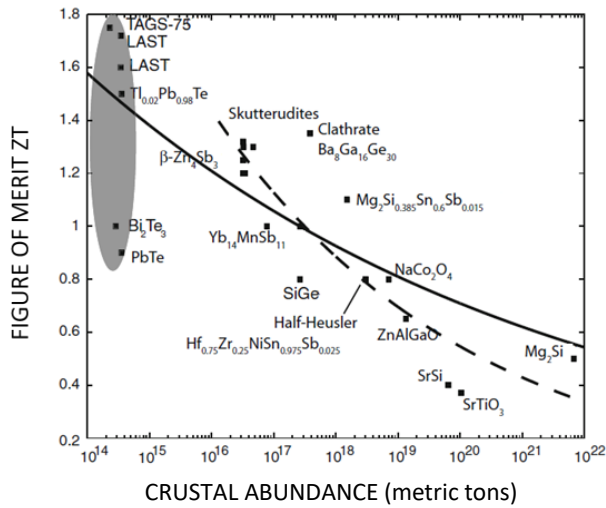
Skutterudites

Skutterudites are some of the widely investigated thermoelectric materials. Occurring naturally in CoAs_3 -type structure, skutterudites are formed by transition metals (Co, Rh, Ir) and group V elements (P, As, Sb). Rhodium (Rh) and Iridium (Ir) are two of the rarest elements in the Earth’s crust.

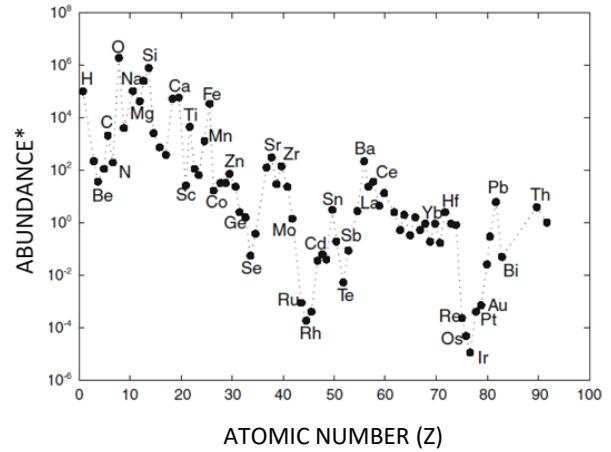
| Material | ZT | Weighted Crustal Abundance (Metric Tons) |
|---|--------------|--|
| Bi ₂ Te ₃ | 1 (300 K) | 2.8×10^{14} |
| SiGe | 0.8 (1000 K) | 2.6×10^{17} |
| PbTe | 0.9 (750 K) | 3.5×10^{14} |
| AgPb ₁₈ SbTe ₂₀ (LAST) | 1.72 (800 K) | 3.4×10^{14} |
| (GeTe) ₇₅ (AgSbTe ₂) ₂₅ (TAGS-75) | 1.75 (700 K) | 2.3×10^{14} |
| Sr _{0.16} Yb _{0.03} Co ₄ Sb ₁₂ (skutterudite) | 1.32 (850 K) | 3.2×10^{16} |
| Ba ₈ Ga ₁₆ Ge ₃₀ (clathrate) | 1.35 (900 K) | 3.8×10^{17} |
| Yb ₁₄ Mn _{1-x} Al _x Sb ₁₁ (Zintl phase) | 1 (1200 K) | 7.7×10^{16} |
| β -Zn ₄ Sb ₃ | 1.3 (670 K) | 4.6×10^{16} |
| Hf _{0.75} Zr _{0.25} NiSn _{0.975} Sb _{0.025} (half-Heusler) | 0.8 (1025 K) | 3×10^{18} |
| NaCo ₂ O ₄ (oxide) | 0.8 (1050 K) | 7.1×10^{18} |
| Mg ₂ Si _{0.4-0.015} Sn _{0.6} Sb _{0.015} (silicide) | 1.1 (800 K) | 0.5×10^{18} |

Figure 2.5: High ZT bulk thermoelectric materials listed with their weighted crustal abundance. (Modified from [12]: R. Amatya, R. J. Ram, *Trend for Thermoelectric Materials and Their Earth Abundance*, 2012)

It is clear that, in order to have competitive and viable TE devices with a real impact on today's issues, TE performances are not the only parameters to be considered. High ZT and TE efficiency are of course crucial characteristics but, abundance on earth (showed in "Figure 2.6"), low and relatively fixed price, non-toxicity are fundamental points too. Without responding to these characteristics, the mass production of TE devices could not happen and consequently no effective impact could follow the enormous potential of thermoelectricity.



(a)



(b)

Figure 2.6: ZT vs crustal abundance for bulk TE materials
 Abundance* (atoms of element per 10^6 atoms of Si)
 (Modified from [12]: R. Amaty, R. J. Ram, Trend for
 Thermoelectric Materials and Their Earth Abundance, 2012)

Some of the materials that show a good balance between TE performance and abundance and low cost are: FeSi_2 , ZnO and Mg_2X ($\text{X}=\text{Si}, \text{Ge}, \text{Sn}$). In this work, magnesium silicide (Mg_2Si) has been investigated. It has been synthesized and 3d printed.

3 Magnesium Silicide: A Novel Thermoelectric Material

The intermetallic compound magnesium silicide (Mg_2Si) is a very promising novel thermoelectric material for the development of eco-friendly and efficient TE devices. An interesting combination of chemical, physical properties and TE performance make Mg_2Si a very promising material for applications in the range of 500 to 800 K. The wide disposability and abundance in the earth of constituent elements, Mg and Si, are a major reason for Mg_2Si based compounds to gain importance as TE materials. Magnesium silicide is intrinsically a n-type semiconductor and his properties can be enhanced by doping with element such as Al, Bi and Sn. In addition, doping elements such as Ca or Ag make possible the obtaining of p-type properties. Then, by using the same material and only doping with different elements, it is possible to obtain p-type and n-type, crucial condition for the development of TEGs. The synthesis of Mg_2Si could be obtained by different techniques, such as Mechanical alloying (MA), hot pressing (HP) and spark plasma sintering (SPS). All techniques that start from components powder.

3.1 Magnesium Silicide: structure and physico-chemical properties

Mg_2Si is an intermetallic inorganic compound, constituted by silicon and magnesium. It crystallizes in the antifluorite configuration as shown in “Figure 3.1”, with cubic crystal lattice cell parameters $a = b = c = 6.404 \text{ \AA}$ [14] (other authors report 6.351 \AA [15]) and $\alpha = \beta = \gamma = 90^\circ$. The Si atoms occupy the corners and face-centered lattice sites, while Mg atoms occupy eight tetrahedral positions inside of the unit cell. The distance between Mg and Si atoms has been found to be 2.77 \AA . The coordination number of Si and Mg are eight and four respectively [14]. The cubic lattice of Mg_2Si transforms to hexagonal lattice at high pressure ($> 25 \text{ kbar}$) and temperature ($> 900^\circ\text{C}$) [15].

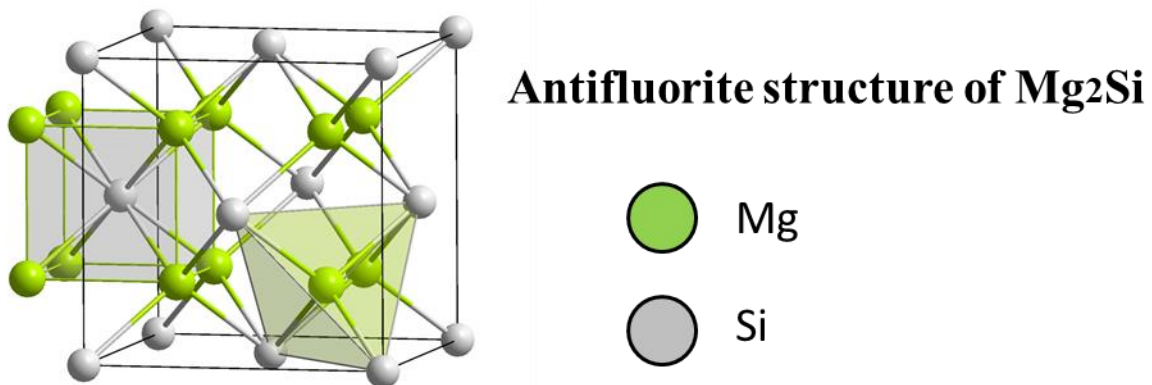


Figure 3.1: Antifluorite structure of magnesium silicide
(Source: www.wikipedia.org)

In magnesium silicide, silicon atoms present filled s- and p-electron orbitals and each Si atom forms four covalent sp^3 -bonds. Mg subshells are only half-filled and there is no bonding between the two magnesium atoms. Bonds in this compound are mainly covalent with a 25 % of ionic component [14]. The Mg_2Si narrow energy band gap is 0.77 eV .

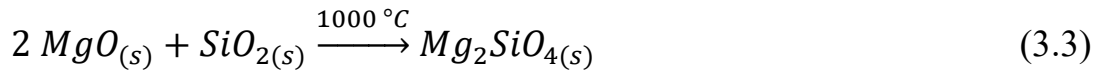
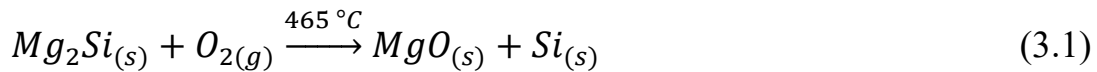
The melting temperature is reported to be in a range $1355/1375 \text{ K}$ ($1082/1102^\circ\text{C}$), and the vapour pressure is lower than 0.001 bar at 20°C . It has a molecular mass of 76.71 g/mol and it

is light-weight, with a density of 1.99 g/cm³. Mg₂Si also exhibits good mechanical properties with high young's modulus (120 GPa) and elevated compressional strength (1640 MPa) [15].

3.2 Chemical reactivity of Magnesium Silicide

Magnesium silicide reacts with releasing flammable gas and with acids for giving silanes. At room temperature no reaction occurs with alkali solutions.

It shows a good oxidation resistance, starting to oxidize at ~ 450-465 °C [16, 17] with an oxidation kinetic that rapidly increase above these temperatures. The oxidation mechanism, as reported by *Stathokostopoulos et al.* [16], is described by reactions reported in Equation (3.1), (3.2) and (3.3):



Below 465 °C, a protective MgO thick layer creates protecting the underlying Mg₂Si. Above this temperature, the oxide layer is not protective to Mg₂Si permitting the penetration of oxygen. Then gradually, Mg₂Si reacts with oxygen forming MgO and Si (3.1). Above 710 °C, Si reacts with oxygen and forms SiO₂ (3.2). Finally, at high temperature (~ 1000 °C) the solid-state reaction between MgO and SiO₂ leads to the formation of forsterite phase (Mg₂SiO₄) (3.3).

Understanding the oxidation mechanism is important both for the final application of the material and the fabrication route. The presence of other phases, apart from the magnesium silicide one, reduces considerably the electrical properties of the material. The presence of MgO, that easily forms, is indicated by many authors as one of the main problem in the magnesium silicide production. The formation of magnesium oxide considerably decreases the electrical conductivity of the material and so, the TE properties.

de Boor et al. [18] demonstrated that the carrier concentration is unaffected by MgO, but the carrier mobility is reduced, especially at lower temperatures. This results in a clear decrease of ZT, and so of TE properties, in function of magnesium oxide content, as shown in "Figure 3.2".

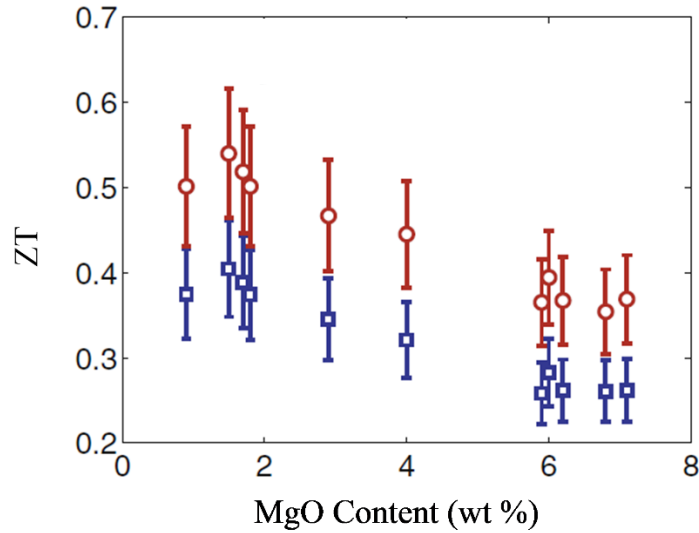


Figure 3.2: Correlation between MgO wt % and ZT at 320 K □ and 500 K ○
 (Modified from [18]: J. de Boor et al, Microstructural effects on thermoelectric efficiency: A case study on magnesium silicide, 2014)

This limits the upper operating temperature of Mg₂Si based devices. For this reason, they are devices that can be used in an intermediate range (500-800 K, 227-527 °C). On the other hand, also the fabrication route should take in account the oxidation process. During the synthesis, before obtaining the alloy, the operations must be performed in controlled atmosphere. However, even after obtaining the alloy and when producing devices, such as TEGs, the oxidation must be considered. Sinterization or other thermal treatments above 700 °C could not be performed in air. In fact, even if the material is fabricated at lower temperatures, compaction usually has to be performed at T > 850 °C, so that MgO is frequently encountered in the final devices, even starting from MgO-free powder.

3.3 Mg₂Si Fabrication Routes and State of the Art

The reaction between magnesium and silicon showed in equation (3.4), has free Gibbs energy of formation negative in the interval 298 - 923 K (25/650°C) [19, 20]. The reaction is self-propagating, this because the standard formation enthalpy of Mg₂Si is -77.3 kJ/mol (exothermic reaction) [20].



“Figure 3.3” shows the magnesium-silicon phase diagram. Magnesium silicide, the only possible binary phase of Mg-Si system, is called “line compound” because, as it visible in the figure, it forms only with the right stoichiometric proportions between Mg and Si. A small fluctuation of the stoichiometric composition leads to inclusion of other phases in the compound.

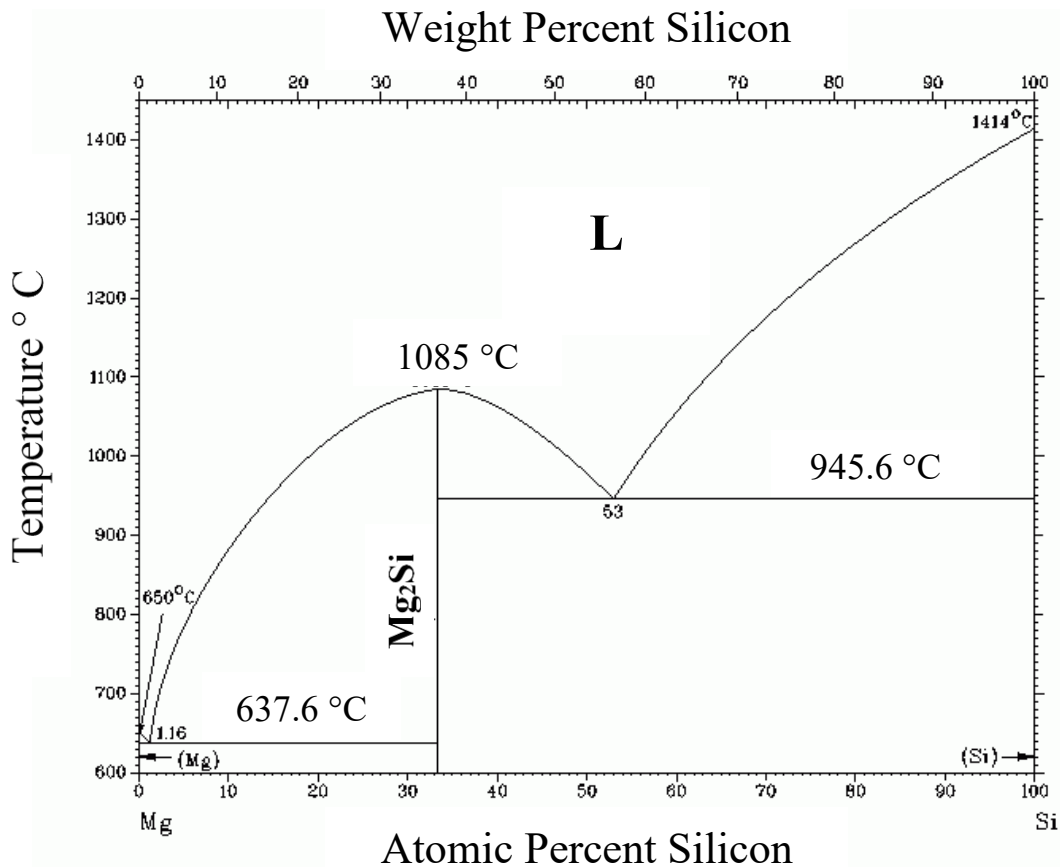


Figure 3.3: Phase diagram magnesium-silicide

(Modified from [21]: G.H. Li et al, *Magnesium Silicide Intermetallic Alloys*, 1993)

Major challenges of the magnesium silicide fabrication are [22]:

- the large differences between Mg melting temperature (650 °C) and Si melting temperature (1414 °C)
- Mg boiling point (1110 °C) is lower than Si melting point
- the proximity of the boiling point of Mg to the melting point of Mg₂Si

The consequences are: the impossibility of having both Mg and Si liquid at the same conditions and a high Mg vapor pressure at the working conditions. That could lead to Mg evaporation, resulting in non-stoichiometric compounds.

3.3.1 Fabrication Routes: Melting Techniques

Melting of the elements is a traditional approach for the fabrication of Mg₂Si. In this approach, the elements are sealed together in a vessel and heated above the melting point of Mg₂Si. The liquid is maintained above it, for enough time in order to obtain a complete reaction. After that it is cooled, ending up in a polycrystalline ingot material. This method is rather simple but has some disadvantages. Due to the high temperature applied, very good vacuum is required to prevent Mg oxidation. But in these conditions, evaporation of Mg is inevitable, even though the reaction happens in a closed vessel. To compensate excess of Mg is typically added but, finding the correct amount of excess Mg is really challenging.

de Boor et al. [23] fabricated Sb-doped Mg₂Si with nominal composition Mg₂Si_{0.9875}Sb_{0.0125} by induction melting of the elements. The obtained ingot was reduced to a powder (hand-crushed or ball-milled). Then, pellets of 15-mm diameter were fabricated using current assisted sintering. The influence of different sintering temperatures was investigated, and it was obtained a $ZT_{\max}=0.75$ at 820 K (547 °C).

3.3.2 Fabrication Routes: Solid-state synthesis

Solid-state syntheses present the benefit of requiring lower temperatures than liquid routes. The approach mainly consists in starting by elemental powders and applying a treatment to provide the energy necessary for the reaction (thermal treatment, spark plasma sintering, microwaves radiation). Some different routes have been proposed:

Combustion synthesis

Godlewska et al. [24] fabricated magnesium silicide devices by self-propagating reaction and hot pressing. Stoichiometric proportion of the powder constituent were mixed, homogenized and cold pressed to obtain small cylinders. The cylinders were then, subjected a self-propagating reaction by global heating to 550–579°C K. This can happen thanks to the exothermicity of the reaction. The reaction product was Mg₂Si powder that was compacted using hot-pressing with maximum applied pressure of 25 MPa, temperature of 860 °C and time of 2 h. The obtained material was almost single phase, with small Si and MgO impurities. Thermoelectric properties are not reported.

Microwave radiation

Microwave radiation was used as an energy source to synthesize nanoscale Mg₂Si powder. *Savary et al.* [25] obtained nanocrystalline Mg₂Si by a fast process carried out using microwave radiation. The starting materials were Mg turnings and Si chunks. They have been milled in a high-energy ball mill. The resulting mixture of powders of Mg and Si was cold pressed and then heated by microwave irradiation, with power from 125 W up to 300 W. The total process is quite fast; for example, with two hours milling and 2 minutes of microwave heating (175 W) Mg₂Si with particle size smaller than 100 nm was produced. No information is reported about the thermoelectric properties of the material.

Spark plasma sintering (SPS)

Spark plasma sintering was used by *Yang et al.* [26] to fabricate magnesium silicide. Off-stoichiometric mixture of the constituents' powder (with an excess of magnesium) are the starting materials, while the optimum sintering parameters are found to be 550 °C K - 0 MPa - 10 min.

Two-steps solid reaction and SPS consolidation

Liu et al. [27] fabricated Mg₂(Si, Sn) by using a two-steps solid-state reaction from elemental powders. The constituents were mixed, pressed into cylinders, and then annealed at 700 °C. To complete the solid reaction and to increase the homogeneity of the products, the pellets were ground into powders, cold-pressed and then annealed in vacuum for the second-stage solid state reaction, at a temperature below 700 °C. Then, SPS consolidation followed.

Ball milling

As an alternative Mg_2Si can also be synthesized employing mechanical energy from high-energy ball milling (BM) (“mechanical alloying”). Moreover, BM can also be used to include secondary phases or dopants into the material, and to reduce grain sizes and consequently effect material microstructure and TE performance. Si is hard and brittle, Mg is relatively soft and ductile. It tends to agglomerate during the BM process. To overcome this inconvenient, organic media (such as hexane) are used as milling aids. However, long milling times (more than 20 hours milling) are usually needed to obtain the alloy. In many cases, a complete alloy formation doesn’t happen only by mechanical alloying. So, often, a thermal treatment follows the BM. In this situation it is of no interest obtain a complete alloy formation after the BM. Then, considerably lower milling times are needed, because the reaction between magnesium and silicon happens/concludes in the second step. The advantage of this approach lays in the fact that, BM reduce the energy activation of the reaction letting it to happen at lower temperatures.

A work of *Lee et al.* [28] showed that Mg_2Si didn’t form after 60 hours of milling and only started to form only after 180 hours of milling. Even after 260 hours the alloy formation was not complete. The magnesium silicide was then obtained by annealing the 60 hours milled powder at 620 °C.

Wang and Qin [29] couldn’t obtain a complete alloy formation after 20 and 60 hours milling. However, it was proved how the activation energy of the alloy formation reaction is substantially smaller for the milled powder than for the unmilled. That resulted in sensible decrease of the temperature reaction. As shown in “Figure 3.4”, DSC performed on unmilled and milled powder, presents exothermic peaks at different temperatures: lower for the milled powder. Unmilled powder shows only one sharp peak at ~500 °C while the milled powders show two peaks (~180-250°C and 370-450 °C). The exothermic peaks are associated with the exothermicity of the reaction between magnesium and silicon.

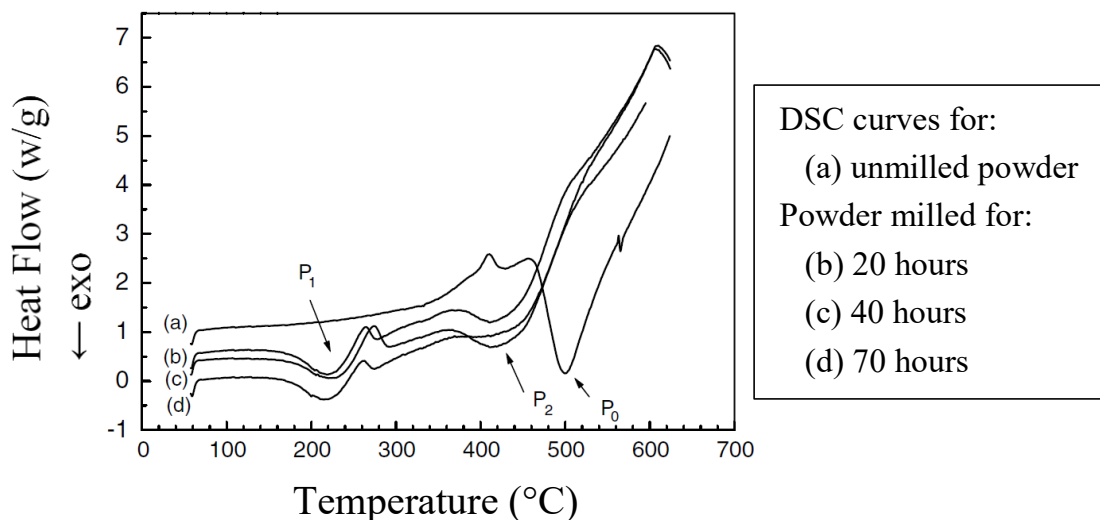


Figure 3.4: Comparison of DSC curves on milled and unmilled powders: Shifting of the exothermic peak.

(Modified from [29], L. Wang and X.Y. Qin, *The effect of mechanical milling on the formation of nanocrystalline Mg_2Si through solid-state reaction*, 2003)

In 1998, Lu et al. [30] managed to obtain a single phase of magnesium silicide after 50 hours of MA, even though with some MgO contaminations. It was also observed that the Mg₂Si phase formation started to form after 10 hours of mechanical alloying. For milling times lower than 50 hours it was needed a thermal treatment to complete the reaction. However, it has been proved one more time that, the reaction occurs at lower temperatures, increasing the milling time. On the other side, it has been observed that the longer the milling time, the higher the probability of contaminations. It is also important to notice that in their experimental work the authors used stearic acid as a milling fluid. It may have been source of oxygen for the formation of magnesium oxide; the milling in fact was performed (as in all the presented cases) in inert atmosphere. The authors so suggested, the use of an oxygen-free milling vial, such as hexane. Anyhow, the main conclusion is that is advised to combine the mechanical action with the thermal action: MA alloying itself could lead to a complete alloy formation only after very long milling time so, even though it is a room-temperature process, it is preferable to combine it with the dispense of thermal energy afterwards. As it has been stated by the authors, the milling process mechanically activates the powder. After 10 hours of milling, the amount of formed silicide is very small; however, the silicon particles are already embedded in the magnesium ones and so, the interdiffusion distance is minimized. At the same time many defects and residual stress are introduced. Consequently, the energy level of the powder particles is increased from an initial state of G₀ to an activated state of G₁, resulting in the reduction in the activation energy for diffusion (ΔG).

This is clear observing “Figure 3.5” (where the dashed line refers to powder not subjected to MA and the solid one refers to powder that was milled). The MA powder particles have been activated, and the internal energy increased. So, the energy barrier ΔG is decreased and the internal energy tends to decrease by reorganisation of Mg and Si atoms.

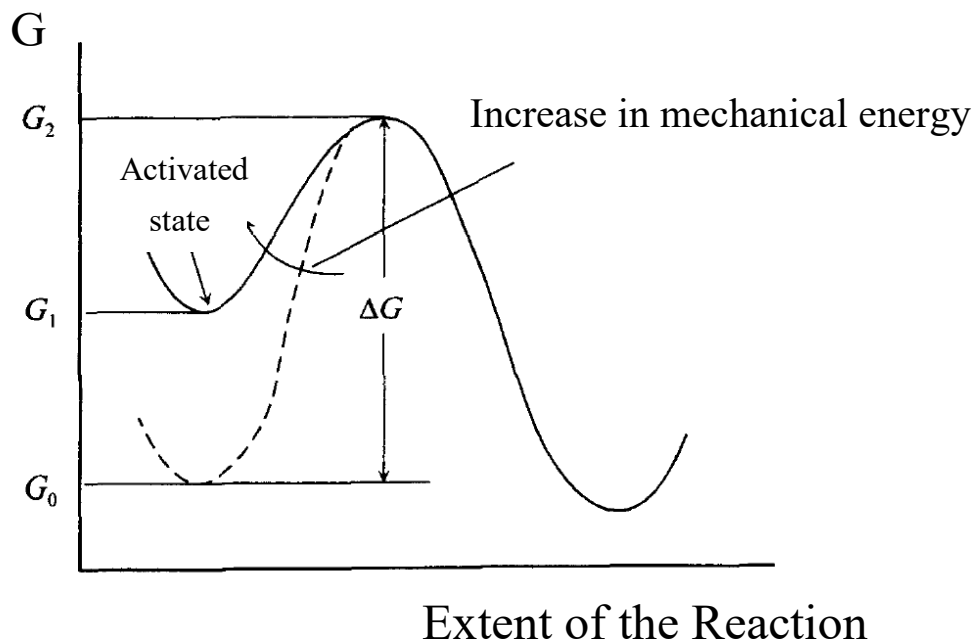


Figure 3.5: Increase of internal energy by mechanical action, resulting in decrease of the activation energy of the formation reaction of Mg₂Si.

(Modified from [30]: L. Lu et al, Formation of nanocrystalline Mg₂Si and Mg₂Si dispersion strengthened Mg-Al alloy by mechanical alloying, 1998)

An interesting approach it has been suggested by *Ioannou et al.* [31] in the manuscript: “*Solid-state synthesis of Mg₂Si via short-duration ball-milling and low-temperature annealing*”. In this work, very short dry milling sessions (30 and 60 minutes) were followed by thermal treatments at relatively small temperatures. The milling time is considerably shorter than the previous examples and interesting results have been reported regarding the annealing temperature. Partially alloy formation has been obtained at low temperatures (150 – 250 °C); 400 °C has been considered the best compromise in terms of synthesis temperature and time, to obtain complete alloy formation. On the other side 12 hours annealing at 300 °C, on powder that wasn't subjected to ball milling, weren't enough to obtain the wanted phase. A short annealing at 550 °C, again on unmilled powder, led only to obtain partial phase formation.

Significant results were obtained by *Bux et al.* [32], that to overcome the Mg aggregation in the vial, used an incremental milling technique. In which Mg was added incrementally to a stoichiometric amount. The powder was milled for less than one hour, then more magnesium was added and so on. According to the results reaction was completed in less than 8 hours and resulted in the synthesis of pure Mg₂Si. It was also possible to include Bismuth as a dopant in different concentrations.

3.4 Doped Magnesium Silicide and its Solid Solutions

Magnesium silicide is an n-type intrinsic semiconductor and its electrical properties can be enhanced by inclusion of doping elements such as Antimony (Sb), Bismuth (Bi), Tin (Sn) and Lanthanum (La). It is also possible obtain p-type magnesium silicide by doping with Silver (Ag) or Calcium (Ca).

Dopants can be considered impurities of different atoms that are added to change the electrical behavior. Due to the very low concentration of mobile charge carriers, in the intrinsic semiconductors if compared to metals, the electrical properties of semiconductors are tremendously affected by the presence of chemical impurities or defects in the crystal lattice. By increasing the quantity of added element, one starts talking about alloying.

3.4.1 N-type dopants

Bismuth (Bi)

Bux et al. [32] synthesized by mechanical alloying Bi-doped magnesium silicide with different dopant concentrations: Mg₂Si_{1-x}Bi_x ($0 \leq x \leq 0.021$).

Hall effect measurements proved that Bi is an effective n-type dopant. Bismuth presents one more valence electron than Silicon, forming a Bi³⁻ ion, realising consequently an e- when substituting the Si⁴⁺ ion. Bi, in fact, replaces Si as a substitutional dopant. Since Bi³⁻ is quite big (1.17 Å), unlikely goes to interstitial sites or substitute Mg²⁺ ions (0.85 Å).

The solubility limit of Bi in Mg₂Si seems to be 0.7 at%, this is in good accord with “Figure 3.6”, where the carriers concentration linearly increases with the atomic percentage of Bismuth, up to 0.7 at% where the carrier concentration stabilizes. At higher concentrations, the authors reported that thanks to SEM analysis, excess of Bi collects at the grain boundaries.

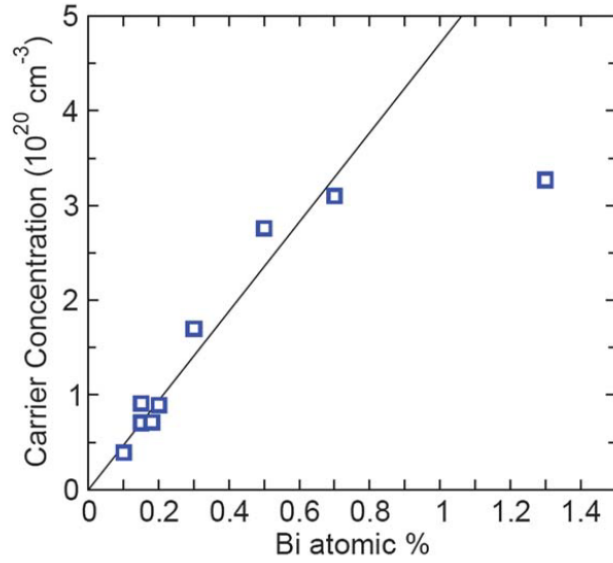


Figure 3.6: Carrier concentration [$10^{20}/\text{cm}^3$] vs Bismuth Atomic %
 (Modified from [32]: S. K. Bux et al, Mechanochemical synthesis and thermoelectric properties of high quality magnesium silicide, 2011)

However, more parameters are influenced by the doping concentration, such as mobility of the carriers, resistivity, Seebeck coefficient and thermal conductivity. All this consequently influences the TE performances. “Figure 3.7” shows ZT in function of the different doping concentrations, showing an optimum at 0.15 at%.

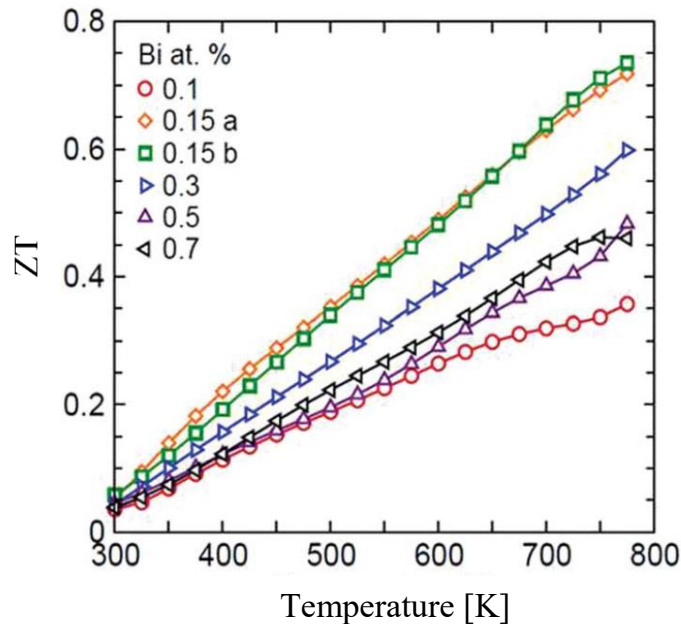


Figure 3.7: ZT function of Temperature and Bismuth atomic concentration
 (Modified from [32]: S. K. Bux et al, Mechanochemical synthesis and thermoelectric properties of high quality magnesium silicide, 2011)

Antimony (Sb)

As for Bismuth, Antimony (V group) substitutes Silicon (IV group) atoms, and acts as a donor. *Tani and Kido* [33] studied the effects on magnesium silicide TE properties by doping with Sb. The fabrication route was SPS. In their manuscript the authors studied the influence of the dopant concentration on various properties. The various concentrations experimented by the authors fall in the proportion: $\text{Mg}_2\text{Si} : \text{Sb} = 1 : x$ ($0.000 \leq x \leq 0.02$)

By increasing the dopant concentration:

- the electrical resistivity decreases
- the Seebeck coefficient increases
- the thermal conductivity has a bivalent trend, because:
 - the lattice contribution decreases
 - the electronic contribution increases

Overall, the combination of these parameters led to a $ZT_{\text{max}} = 0.56$ at 862 K (589 °C) with $x=0.02$. Anyhow, the addition of Sb considerably increased the ZT compared to undoped Mg_2Si , as shown in “Figure 3.8”.

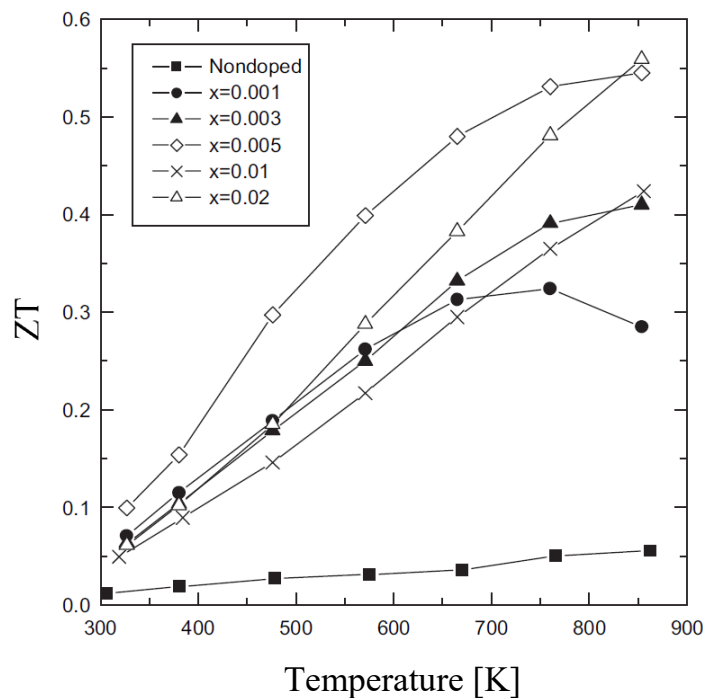


Figure 3.8: Dimensionless figure of merit (ZT) of Sb-doped Mg_2Si in function of dopant concentration and temperature.

(Modified From [33]: J. Tani and H. Kido, *Thermoelectric properties of Sb-doped Mg_2Si semiconductors*, 2007)

Tin (Sn): Solid Solutions ($\text{Mg}_2\text{Si}_{1-x}\text{Sn}_x$)

Several works [3, 27, 34-36] proved how solid solutions $Mg_2Si_{1-x}Sn_x$ are promising materials, giving higher ZT values than Mg_2Si alone. The following list presents briefly some of the best results encountered in literature:

- By doping with Sb (solution of composition $Mg_2Si_{0.4}Sn_{0.6}$) *Liu et al.* [27] obtained a $ZT_{max} \sim 1.11$ at 860 K (587°C)
- A solid solution $Mg_2(Si, Sn)$ was produced by *Zhang et al* [34], and doped with Lanthanum (La), achieving a $ZT_{max} \sim 0.81$ at 810 K (537 °C)
- Very high ZT have been obtained also by *Gao et al.* [35] that fabricated Bi-doped $Mg_2Si_{0.4}Sn_{0.6}$ with a $ZT_{max} \sim 1.55$ at 723 K (450 °C)
- *Luo et al.* [36] produced Bi-doped $Mg_2Si_{0.8}Sn_{0.2}$ with a $ZT_{max} \sim 1.17$ at 850 K (577 °C)

3.4.2 P-type dopants

Calcium (Ca)

Miyazaki et al. (2017) [37] synthesized bulk Ca-Mg-Si intermetallic compounds, with various compositions: $Ca_{33.3+x}Mg_{33.3-x}Si_{33.3}$ ($-12 \leq x \leq 3$). Ball milling and subsequent Pulse Current Sintering (PCS) were used. The authors proved the p-type behaviour ($\alpha > 0$) of these compounds. In a previous work *Zhang et al.* (2007) [38] observed a decrease of the TE properties in Ca-Mg-Si based compounds compared with Mg_2Si . In the manuscript the authors measured negative values of Seebeck coefficient ($\alpha < 0$) with lower values (in module) compared to magnesium silicide. The authors then, didn't recognize these compounds as p-type. However, this behaviour could be explained with the coexistence of Mg_2Si ($\alpha < 0$) and Ca-Mg-Si based compounds ($\alpha > 0$), overall resulting in a worsening of TE properties. Then, Ca-Mg-Si compounds, as observed by Miyazaki have a great potential, as a p-type thermoelectric, however the fabrication and final composition should be controlled carefully, in order to avoid an overlap of p and n-type behaviour.

Silver (Ag)

P-type Mg_2Si doped with silver was fabricated by *Berthebaud and Gascoin* [39], having the nominal composition $Mg_{1.99}SiAg_{0.01}$. The obtained ZT isn't very high (0.35 at 770 K). However, emerged one more possibility for fabricating magnesium silicide with p-type behaviour.

4 Characterization Techniques

This chapter briefly describes the techniques used to analyse and characterize the materials in the various steps of this work.

4.1 Scanning Electron Microscopy (SEM)

Scanning electron microscopy (SEM) [40-43] is a technique by which the surface of a sample is hit by an electron beam that is accelerated along the microscope column and focused by electromagnetic lenses. The electrons interact with atoms of the specimen, creating signals with information about the topography and composition of the examined material. The reflected beam is collected and displayed on a cathode ray tube. A fundamental condition for this technique is that the surface of the samples must be electrically conductive. So, in the case of non-conductive materials, a thin metallic surface coating is applied. Magnification goes from 10x up to 10^6 x. “Figure 4.1” schematize a scanning electron microscope. For this thesis, two different SEM were used: FEG-SEM Jeol JSM 7001F and a Vega 3 TESCAN.

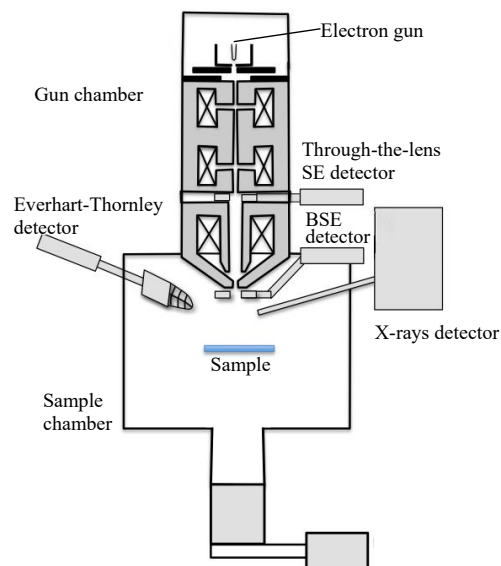


Figure 4.1: Scheme of a SEM

(Modified from: [40] A. M. Chiodoni and E. Tresso, Morphological and Structural Properties, 2013, Silicon Based Thin Film Solar Cells, Chapter 6)

After the interaction between the electrons beam (primary electrons) and the materials, different radiations are detectable (phenomena showed by “Figure 4.2”):

- Back scattered electrons (BSE), coming from the incident beam, are emitted with energy similar to the initial energy after elastic collision. Can give information of the compositional contrast, thanks to the capacity of the atoms to divert the beam.
- Secondary electrons (SE) are ejected from the surface of the sample and have lower energy than the initial beam. They give information about the surface morphology.
- X-rays are also produced giving information about the composition.

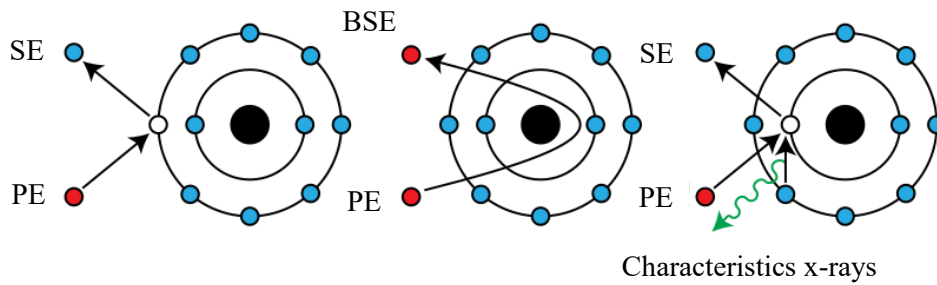


Figure 4.2: Generation of secondary electrons (SE), back-scattered electrons (BSE) and x-rays after interaction of the sample with the primary electrons beam (PE).

(Source: www.wikipedia.org)

4.2 X-ray Diffraction (XRD)

X-ray diffraction is a non-destructive and powerful technique used for examining the crystalline structure of materials [40, 43, 44]. It is based on the elastic scattering of x-rays by the electrons of the atoms constituting the crystalline structure of the material. X-rays have short wavelengths, in the magnitude of the atomic spacing of solids (\sim nm), and consequently high energies. When a solid material is invested by an x-ray beam, a portion of it is scattered in all directions by the electron clouds of the material atoms, that stand within the beam's path. In particular way, when the atoms are periodically spaced the scattered radiation undergoes destructive or constructive interference (diffraction). A diffracted beam is made by a big amount of scattered waves that mutually reinforce each other.

As shown by "Figure 4.3" when an x-rays beam (parallel, monochromatic, and coherent) of wavelength ' λ ' impinges (hitting angle ' θ ') two parallel planes of atoms (with interplanar spacing ' d '), two rays (A and B) of this beam interfere constructively and are diffracted, when the Bragg's law is satisfied ("Equation 4.1"), where ' n ' is an integer number.

$$2 d \sin\theta = n \lambda \quad (4.1)$$

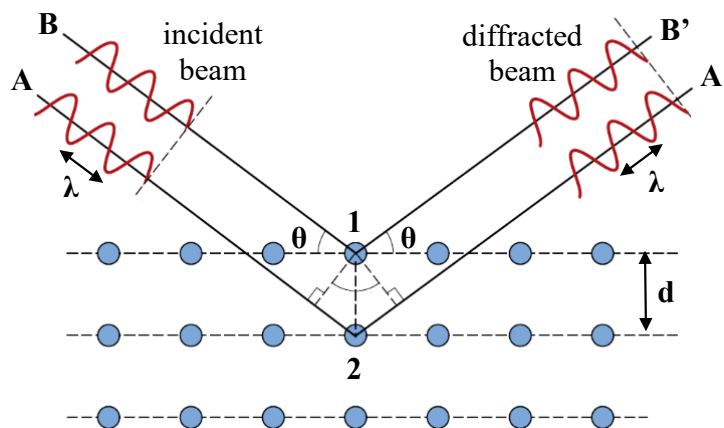


Figure 4.3: Interaction between the incident x-rays beam and the materials atoms.
(Modified from [43] W. D. Callister and D. G. Rethwisch, *Materials Science and Engineering. An introduction*, 2014)

An x-ray source (x-ray tube), an x-ray detector and a goniometer are the main components of a diffractometer. The x-rays are produced by the instrument because electrons from a hot filament are accelerated in a tube and hit the anode material (usually Cu). The rays that form are focused on the sample and the diffracted beam is collected by the detector. A typical diffractometer, with the widely employed Bragg-Bentano configuration, is schematized by “Figure 4.4”. In this configuration, the x-rays are directed to the sample with an angle θ and the diffracted beam is detected at the same angle θ .

The instrument used for XRD analysis showed in this thesis was X’Pert Pro Multipurpose Diffractometer® (MPD) by PANalytical using a Bragg-Bentano configuration. The x-ray source is a ceramic x-ray tube with Cu anode ($\lambda=1.540593 \text{ \AA}$).

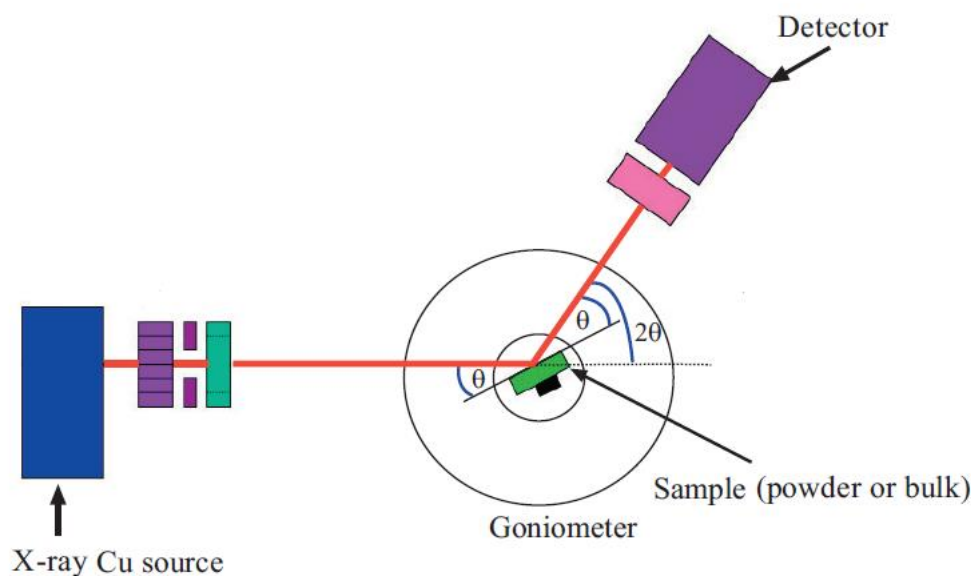


Figure 4.4: Scheme of the Bragg-Bentano congiguration

(Modified from [40]: A. M. Chiodoni and E. Tresso, *Morphological and Structural Properties*, 2013, *Silicon Based Thin Film Solar Cells*, Chapter 6)

4.3 Raman Spectroscopy

Raman spectroscopy is a technique based on inelastic light scattering [45, 46]. In these kind of analysis, polarized and monochromatic light, with known frequency, is scattered by a specimen. The scattered light is then examined and used to construct a Raman spectrum. Great part of the scattered radiation has equal frequency to the incoming one (Rayleigh Scattering). A small portion of the scattered radiation will show different frequency (“frequency-shifted”) of the monochromatic incident radiation. The "Raman shift" is an intrinsic property of the sample (not dependant from the incident frequency) that is related to the exchanged vibrational energy. A Raman spectrum is presented as an intensity-vs-wavelength shift. An experimental apparatus is showed by “Figure 4.5”. For the Raman spectra determination, it was used a Confocal Raman Spectrophotometer (Witec Alpha 300 RAS) using a laser with wavelength of 532 nm.

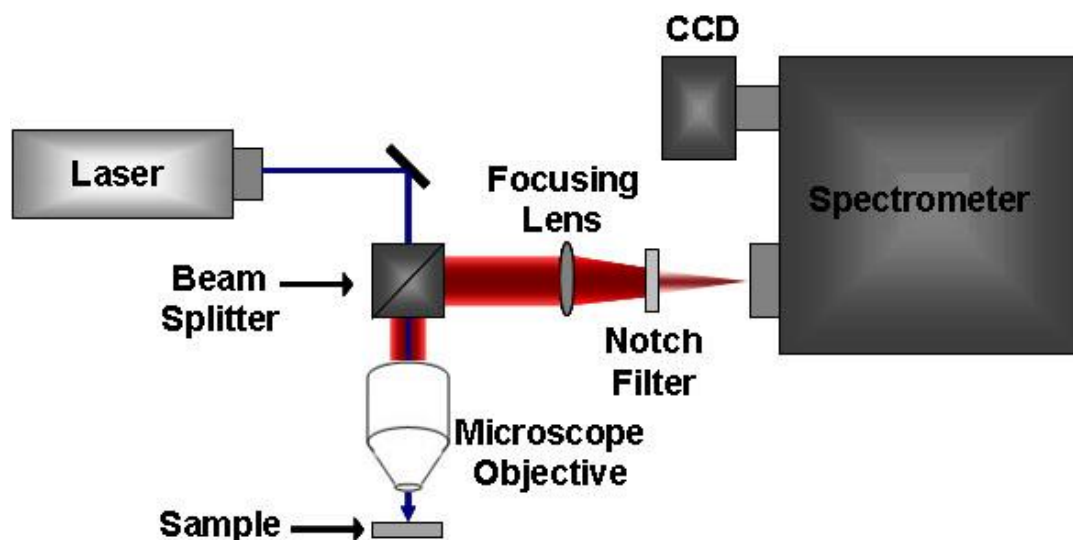


Figure 4.5: Scheme of Raman spectrometer.
 (Source: www.sciencefacts.net)

4.4 Infrared Spectroscopy (FTIR)

Infrared (IR) spectroscopy is based on the interaction of infra-red radiation with materials [45]. Infrared spectroscopy has common features with Raman spectroscopy. However, they are present important differences: they are based on different processes (absorption/transmittance for IR and scattering for Raman). Moreover, while in Raman spectroscopy a beam with a single frequency impinges the sample, in IR spectroscopy a polychromatic infrared radiation impinges the specimen.

Practically, a sample is impinged by a beam of infrared light. If the IR frequency is equal to the vibrational frequency of a molecular oscillator (in some cases collective vibrations, that is phonons), absorption occurs. Then the transmitted radiation is examined and provide information about the energy absorbed at specific frequencies. In the case of Fourier-transform infrared spectroscopy (FT-IR), an interferometer is used with a Fourier transform analysis aimed to provide the vibrational band of the specimen. The IR spectrometer used for this work was FT-IR spectrometer Mattson 7000 galaxy series: a Fourier transform infrared spectrometer equipped with a DTGS CsI detector and a ATR Golden Gate accessory.

4.5 DSC/TGA

Differential scanning calorimetry (DSC) and thermogravimetric analysis (TGA) are thermo-analytical techniques [47,48]. Often these two techniques are performed combined by the same instrument, such as in the one used in this work: Simultaneous Thermal Analyzer – STA 449 F3 Jupiter®.

- TGA monitors mass changes of the specimen while increasing or decreasing the temperature with a controlled rate. The mass is monitored continuously by a precision balance.
- DSC measures the changes in a material’s heat capacity in function of the temperature (heating or cooling with a controlled heating rate). The analysis is possible by comparing the specimen with a reference, while supplying heat to the two.

For DSC, two different possible configurations are possible:

- Heat flux DSC (showed by “Figure 4.6”): the sample is loaded in a crucible and another identical crucible is left empty and work as a reference. The two are heated in the same block of the furnace. Two thermocouples monitor eventual differences in temperature. The temperature of the reference is only function of the supplied heat; endothermic or exothermic processes may decrease or increase the specimen temperature differently.

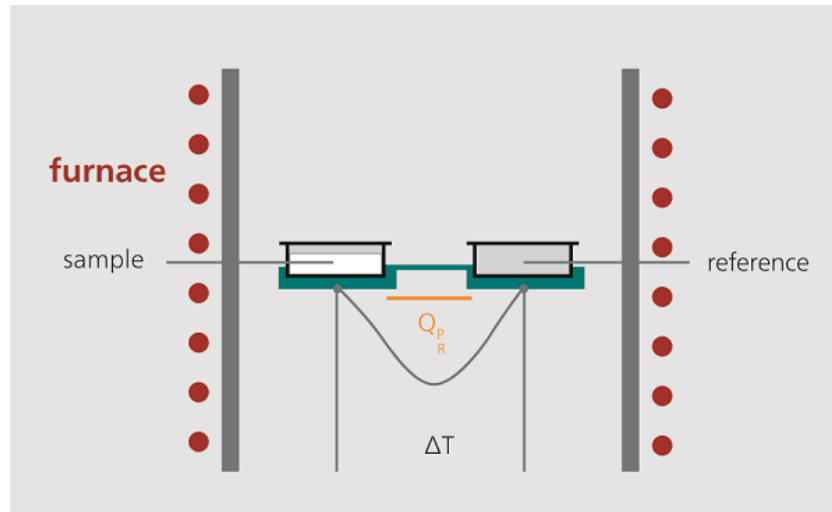


Figure 4.6: Heat flux configuration for DSC analysis.
(Source: www.netzsch-thermal-analysis.com)

- Power compensated DSC: the two crucibles are heated separately while a thermocouple assures to keep them at equal temperature ($\Delta T=0$). It is then monitored, the difference of energy given to the two systems to increase the temperature in the same way.

In any case the output is the quantity of heat necessary to increase the temperature of the sample (heat capacity). DSC provides information on the eventual happening of endothermic processes (vaporization, melting) or reactions that absorb heat or exothermic ones (crystallization, combustion or other reactions) that generate heat. The combination with simultaneous TGA provides complementary and important information. Those listed processes, in fact, are often matched with mass changes. For instance, during a vaporization process, simultaneously to the heat absorption, a mass loss is visible (due to the phase transformation from liquid state to vapour). Crossing the information obtained by DSC with the one given by TGA allows to understand better which kind of process or reaction is been detected.

5 Magnesium Silicide Synthesis

This chapter presents the experimental procedure followed to fabricate magnesium silicide and the analysis results. The first part of the chapter describes mechanical alloying by ball milling with reference on the alloying mechanism and all the practical parameters that influence the process.

5.1 Ball milling and mechanical alloying [49-54]

Ball milling, is a widely spread technique for materials size reduction, blending, homogenization of samples and also for mechanical alloying.

Mechanical alloying (MA) is process for which an alloy of two or more elements is formed, without the application of a thermal budget. MA is a solid-state process, where powders of the elemental alloy constituents are loaded into the mill and subjected to high-energy impacts from the milling balls. The process involves the repeated fracturing and cold welding of the powder, making possible the alloy synthesis. The mechanical energy is provided by the mill and transferred to the milling balls and to the materials. It activates chemical reactions, structural changes, and particle size reduction.

The application of mechanical energy for materials size reduction and materials treatments goes back of millennia in human history. However, it is only at the end of the 19th century that it was recognized the possibility of alloying different materials by the application of mechanical energy. Simultaneously it was introduced the term “mechanochemistry” [50]. The first successful attempts of MA were made in the 1960s, with the production of nickel-based superalloy and other heat-resistant alloys [51].

MA has been applied in several areas of material science, obtaining many different material systems, such as: nanocrystalline alloys, composites materials, intermetallic compounds, materials strengthened by oxides dispersion.

It is, in general, an effective technique that overcome the inconvenient of operating with materials with a big difference in melting temperatures.

5.2 Ball mill

The experimental setup of a ball mill is quite simple; it is composed by the milling machine, a container (known as vial, jar or bowl) in which the materials are loaded, the milling balls and, eventually, accessory such as security lid or others. Different mills, with different configurations are commercially available: attritors, horizontal mills, planetary mills. The following section explains the functioning of a planetary ball mill, since is the one used for this work.

5.2.1 Planetary ball mill

A planetary mill is composed by:

- A revolving disc
- One or more jars

The jar rotates around its own axis and simultaneously the disc rotates too. The movement is comparable with the planets motion: rotation and revolution. The centrifugal force is transferred to the balls and the powder mixture, inside the bowl. The functioning is schematized in “Figure 5.1”.

The impacts between the powder and the balls, the powder and the jar walls and through the powder itself lead to repeated fracturing and cold welding of the particles.

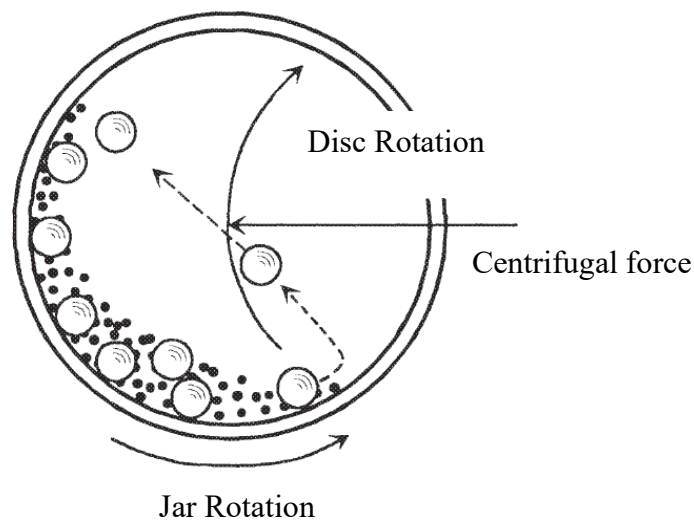


*Figure 5.1: Horizontal section of a planetary ball mill
(Modified from [49] L. Lü and M. O. Lai, Mechanical Alloying, 1998)*

5.2.2 Selection of tools materials

The impact energy could be dosed by changing the rotation speed of the disc: the higher the speed, the bigger the impact energy. However, at high speed it is possible that the efficacy of MA decreases, due to the reduction in the time for the materials diffusion [53].

This is not the only way to increase impact energy; the higher the density of the balls and of the internal bowl walls (that should be of the same material), the bigger the impact energy transferred to the powder. Choosing the suitable materials is a very important task, depending on the application. The main characteristics that must be considered when selecting the jar and balls are summarized in “Table 5.1”.

Table 5.1: Characteristics of materials milling tools [51]

| *referred to milling balls | | | | | |
|-----------------------------------|---|------------------------|----------------|-----------------------------|--|
| Material | Hardness | Density | Energy input* | Wear resistance* | Contamination by abrasion |
| Stainless Steel | 48 - 52 HRC (approx. 550 HV) | 7.8 g/cm ³ | very high | good (to certain extent) | Fe, Cr |
| Hardened Steel | 58 - 63 HRC (approx. 750 HV) | 7.85 g/cm ³ | very high | good | Fe, Cr, C (less than SS) |
| Tungsten Carbide | approx. 1250 HV | 14.8 g/cm ³ | extremely high | very good | W, C, Co (marginal) |
| Agate | hard and brittle 6.5 – 7 Mohs (approx. 1000 HV) | 2.65 g/cm ³ | very low | good (to certain extent) | SiO ₂ |
| Sintered Aluminum Oxide | hard and brittle 8 - 8.5 Mohs (approx. 1750 HV) | 3.9 g/cm ³ | low | good | Al ₂ O ₃ , SiO ₂ (low), no contamination with Fe, Cr, Ni or Co |
| Zirconium Oxide | hard and brittle, tougher than agate 7.5 Mohs (approx. 1200 HV) | 5.9 g/cm ³ | high | very good | ZrO ₂ and Y ₂ O ₃ (marginal), insignificant for analyses |
| Silicon Nitride | approx. 1500 HV | 3.2 g/cm ³ | low | excellent | Si ₃ N ₄ , Y ₂ O ₃ , Al ₂ O ₃ |
| PTFE (Polytetrafluoroethylene) | elastic Shore Hardness D 56 | 2.1 g/cm ³ | very low | poor | contamination with F, C |

As it has already been said, the interior walls of the jar and the balls should be made of the same material, otherwise the harder material could damage the softer one. For the same reason, this material should be, also, harder than the materials subjected to ball milling/mechanical alloying. Then, it must be considered possible contamination, due to the abrasion of the balls or walls. For that, the main features that must be considered are the wear resistance and the possible contaminating elements.

5.2.3 Ball dimension and number, mass ratio balls to powder

Commercially are available several types of mills, with different dimensions: from smaller ones for laboratory applications to bigger ones for bigger production. Then, are available jars with different capacity and balls with different dimensions. The balls dimension is another important feature to consider, when planning the milling. When dealing with size reduction, bigger balls are more indicated for a first grinding of big particles. For finer size reduction smaller balls are suggested. Small balls are also more effective, for size reduction, in the case of wet milling. In the first case (bigger balls) the grinding happens for impact, in the second (smaller balls) for friction.

In the case of MA, however, bigger balls are suggested [52].

The number of balls used, should be bigger enough for an effective process but at the same time leave enough space for the motion of balls and powder inside the jar. The correct amount is usually suggested by the producer. “Table 5.2” lists the right coupling of jar dimension and quantity of balls in function of their diameter. It also shows the percentage of empty space left inside the bowl, not considering the powder and eventual fluid process.

Table 5.2: Suggested number of balls per bowl. In red the number of balls and in blue the % of filled volume in the jar by the balls (without counting powder and eventual fluid process).

(Calculations made with reference in [49, 51, 52])

| | Capacity of bowls (ml) | | | |
|--------------|--|-------------|-------------|--------------|
| | 500 | 250 | 80 | 50 |
| Balls Ø (mm) | Recommended number of balls (% of filled volume) | | | |
| 5 | / | / | / | 160 (20,9 %) |
| 10 | 100 (10,5 %) | 50 (10,5 %) | 30 (19,6 %) | 16 (16,8 %) |
| 20 | 20 (16,8 %) | 15 (25,1 %) | 5 (26,2 %) | 3 (25,1 %) |
| 30 | 10 (28,3 %) | 6 (33,9 %) | / | / |
| 40 | 4 (26,8 %) | / | / | / |

The use of grinding balls of different diameters, even it was found to be effective [49], is not recommended by producers (the bigger ones can damage the smaller ones) [52].

In MA Another important parameter is the balls-to-powder ratio (mass to mass), normally used ratio are in the range 10:1 or 20:1 [49]. In general, higher ratios lead to faster MA, while lower ratios are less effective.

5.2.4 Dry and Wet Milling

Milling could happen in dry conditions (dry milling) or wet conditions (wet milling).

Alloying by milling is possible thanks to high energy transferred by collisions to the powder particles. They are subjected to two phenomena, that make possible MA:

- Cold welding
- Fracturing

In this way the particles are in intimate contact with each other with diffusion distance minimized. Cold welding and fracturing phenomena must be balanced, and one must not prevail on the other. However, it is not easy to obtain a balance. For instance, with soft and ductile materials cold welding is predominant: powder agglomerates may form, and powder can also coat the grinding tools (walls and balls). To overcome this problem, very often, a milling fluid (hexane, stearic acid and many others) -also called: process control agent- is used.

5.2.5 Overheating

While milling at high speeds for long times, pressure and temperature inside the jar easily increase. It may be advantageous, for the MA process. However, overheating and overpressure can be dangerous. Security lids are commercially available, but common strategy is to regularly stop the milling. Alternating milling intervals with breaks is an effective method to avoid overheating.

5.2.6 Inert Atmosphere

Very often powder oxidation is a major issue in MA: finer powders have a big surface-to-volume ratio. The oxidation is then facilitated. To overcome this, working in inert atmosphere is commonly done. The materials can be loaded inside the jar into a glovebox, with inert gas, and sealed (with security lids, rubber rings) before the milling process. Special lids with inlet and/or outlet valves allow to insert inert gases, after the loading of material.

5.3 Increase of internal energy and alloying mechanism

Mechanical alloying is non-equilibrium technique. It means that is a process that leads to obtain non-equilibrium or metastable phase(s). A non-equilibrium or metastable phase presents higher Gibbs free energy of the equilibrium state referred at that specific composition. It is known that, phases with lower Gibbs free energy are more stable than phases with higher free energy. The increase in internal energy is due to various reasons: increase of grain boundaries and accumulation of defects in the crystal lattice. This have been already briefly discussed in Chapter 3, Paragraph 3.3.2 with reference in “Figure 3.5”. This increase in the internal energy results in a decrease of the activation energy for the formation of Mg_2Si .

5.3.1 Alloying Mechanism

During mechanical alloying the particles are continuously cold welded and fractured. These processes are very dependent from the features of the starting powders. In a ductile/brittle system, such as in this work (magnesium/silicon): the ductile powder (Mg) form cold welds. Layered composites form; the brittle constituent (Si) tends to be incorporated by the ductile one. At the same time fracturing may happen. These competing events endure during the whole milling. All these processes lead to get a homogeneous and refined microstructure. The composition of the single particles tends to be the same as the proportion of the starting constituents. Some powder could also coat the inner walls and the milling balls. A thin coating may even be beneficial to avoid abrasion of the grinding tools and to prevent contamination from them. A thick layer, though, should be avoided because may lead to inhomogeneity in the particles composition [54].

5.4 Experimental setting

For the magnesium silicide synthesis was used a planetary ball mill Retsch® PM100, showed in “Figure 5.2”.



Figure 5.2: Picture of a planetary ball mill PM100 Retsch®
(Source: www.retsch.com)

The used jar has a capacity of 50 ml, the inner walls are made of Agate, so the balls. The milling balls have a diameter of 20 mm. “Figure 5.3” shows the milling tools (jar and balls) and the security lid. Agate is a quartz-mineral, composed at 99.9 % of silica (SiO_2). It belongs to the group of semi-precious stones. Reader can find some Agate’s features in “Table 5.1”.

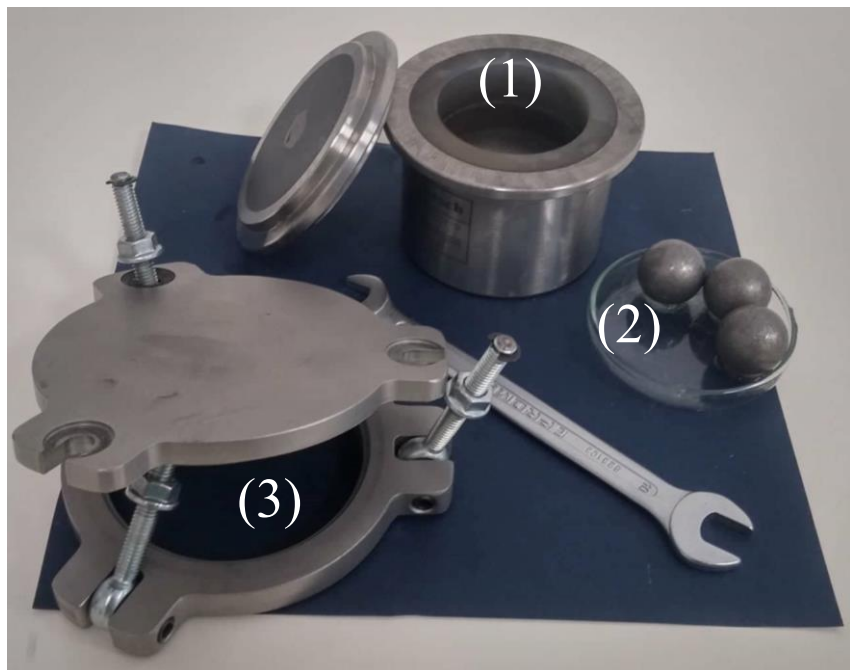


Figure 5.3: Picture of the milling tools: Jar (1), Balls (2) and security lid (3).

5.4.1 Materials and milling parameters

Reagents

The used reagents were:

- Silicon powder [55] (Alfa Aesar, 99.5 %, 325 mesh – 44 μm). Grey and flammable powder. Doesn't need inert atmosphere storage. Hard and brittle solid.
- Magnesium powder [56] (Alfa Aesar, 99.8 %, 325 mesh – 44 μm) Grey powder. Highly reactive with air and water. Must be stored under inert gas. Soft and ductile.

Control process agent

Hexane was used as fluid process (n-Hexane, supplier: Carlo Erba Reagents, 99 %). Hexane is a clear colorless liquid with a petroleum-like odor. It is insoluble in water and less dense than water. It is used as a solvent and chemical reaction medium. Its chemical formula is shown in “Figure 5.4”.

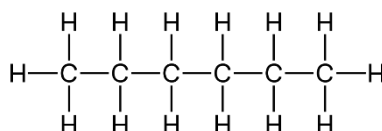


Figure 5.4: Hexane chemical formula
(Source: www.wikipedia.org)

It was selected as a fluid process because it is a “oxygen free” liquid. In this way a possible source of oxygen -that could react with magnesium for giving magnesium oxide- is eliminated.

Milling parameters

The used balls-to-powder mass ratio was 10:1, while the fluid-to-powder ratio was 2:1. Were used three balls with a diameter of 20 mm. Considering the total mass of the three balls is 33.16 g, then the used amount of powder was ~ 3.32 g each milling session, while the used amount of hexane was ~ 6.64 g. Initially, a stoichiometric composition (magnesium/silicon) was used. The calculations are reported in the following paragraph. However, after the first millings and treatments, it was found to be convenient working with a slight excess of magnesium (5-10 %) [26].

5.4.2 Calculations

The molar mass (MM) of magnesium silicide is 76.696 g/mol. That means that in one mol, the mass proportion between the elements is ~ 63.4 % Mg and ~ 36.6 % Si. This percentages were used to calculate the needed mass of elements. Considering 3.32 g of total powder mass, 1.216 g of silicon and 2.104 of magnesium were used (stoichiometric composition). “Table 5.3” resumes these calculations.

Table 5.3: Summary of the calculations for evaluating the needed mass of Si and Mg powder

| | MM [g/mol] | Mass % in one mol of Mg ₂ Si | Corresponding used mass [g] |
|--------------------|------------|---|-----------------------------|
| Mg ₂ Si | 76.696 | 100 % | / |
| Si | 28.086 | 36.62 % | 1.216 |
| Mg | 24.305 | 63.38 % | 2.104 |

5.4.3 Procedure

The materials were loaded into the milling jar inside a glovebox (“Figure 5.5”), filled with argon. The jar was sealed with the security lid showed in “Figure 5.3”. This assured to operate the milling in inert atmosphere.

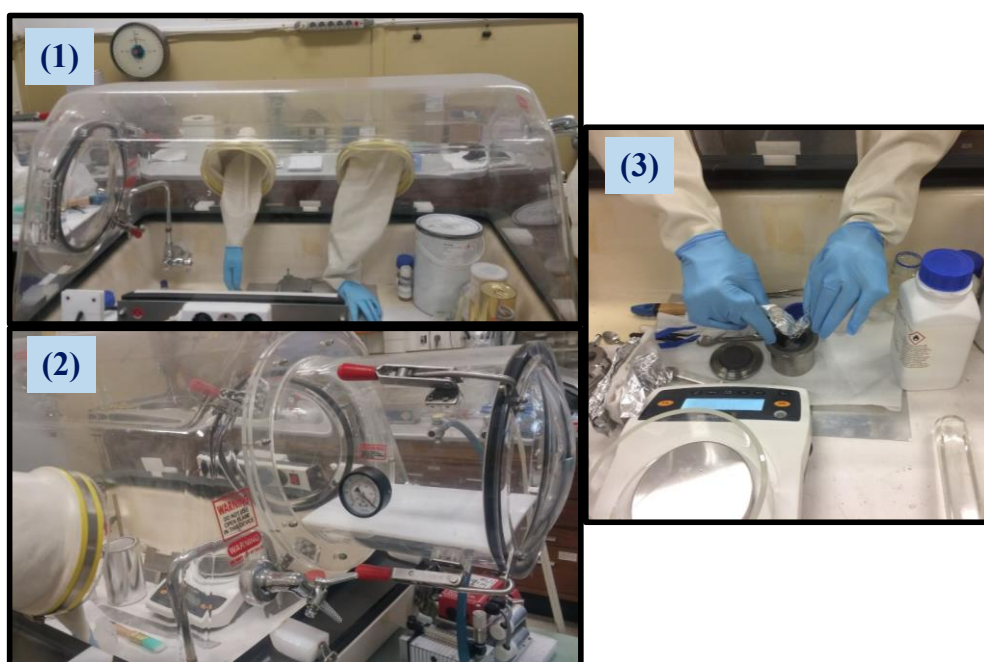


Figure 5.5: Picture of the glovebox (1), detail of the pre-chamber (2), preparation of a milling jar inside the glovebox (3)

Two different milling times were experimented: 5 hours and 10 hours (effective milling time). In both cases the mill speed was set to 400 rpm. In any case, the milling was stopped every 30 minutes for 5 minutes to avoid overheating. This procedure is schematized in “Figure 5.6”. After milling, the milled powders were transferred and stored in the glovebox.



Figure 5.6: Scheme of the operating routine for milling operation. Steps of half an hour milling are alternate with breaks of 5 minutes to avoid overheating.

DSC/TGA analysis was performed on the milled powders and on a stoichiometric proportion of unmilled powder. This analysis was performed to investigate the reaction temperature between Mg and Si (as explained in Chapter 3, Paragraph 3.3.2) and its evolution in function the milling time. Other analysis techniques (XRD, Raman spectroscopy and IR spectroscopy) were used to analyse and identify the evolution of the phase(s) at the various steps (after milling and after thermal treatments).

5.5 Annealing temperature choice by DSC/TGA analysis

As it has been anticipated the DSC/TGA analysis provided the reaction temperature(s) of magnesium and silicon to form magnesium silicide (exothermic reaction).

It was performed on the following powders, in the indicated temperature range:

- Unmilled powder (stoichiometric mixture), from room temperature to 800 °C
- 5 hours milled powder, from room temperature to 1000 °C
- 10 hours milled powder, from room temperature to 800 °C

In all cases the analysis was performed in nitrogen atmosphere with a heating rate of 10 °C/min.

5.5.1 Results:

DSC and TGA are performed simultaneously; the results are showed in the next paragraphs (from “Figure 5.7” to “5.9”), where the blue lines refer to the DSC (right ‘y’ axis) and the green ones to the TGA (left ‘y’ axis).

Unmilled powder

The outcome of DSC on unmilled powder (“Figure 5.7”) showed a sharp exothermic peak at 590 °C.

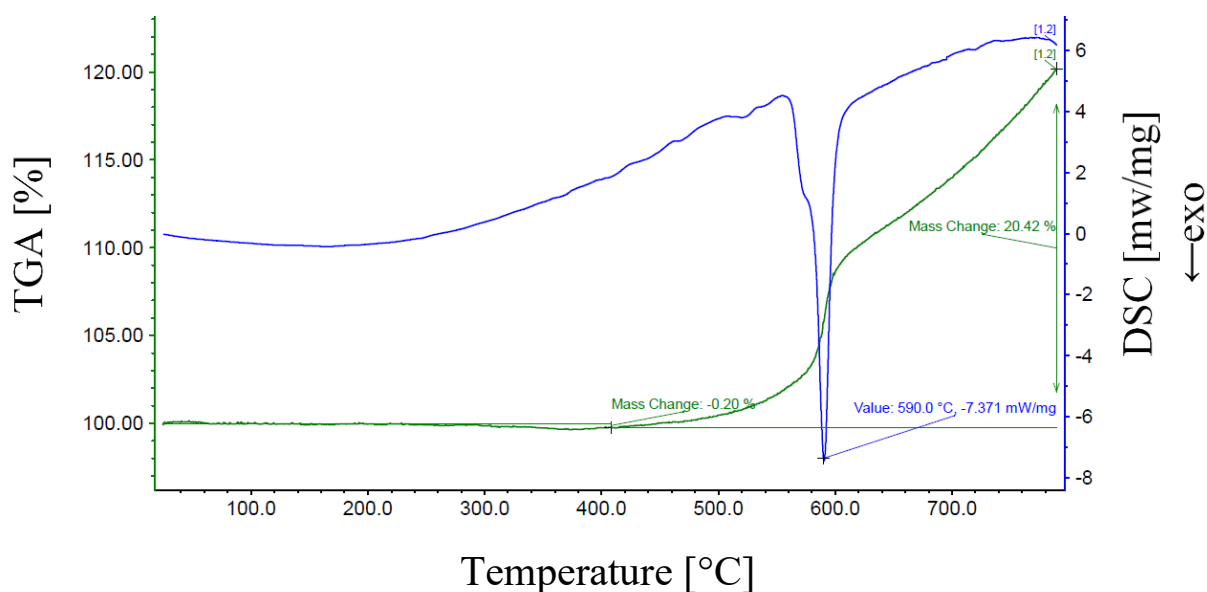


Figure 5.7: DSC/TGA results of unmilled powder

5 hours milled

For the powder milled for 5 hours (that was the only DSC performed up to 1000 °C) there are three visible exothermic peaks centred, respectively in:

- 241 °C
- 408 °C
- 756 °C

Outcome is showed in “Figure 5.8”. Another exothermic peak is visible at more or less 1000 °C, but it wasn’t considered since it is out of the working conditions in any step of this work.

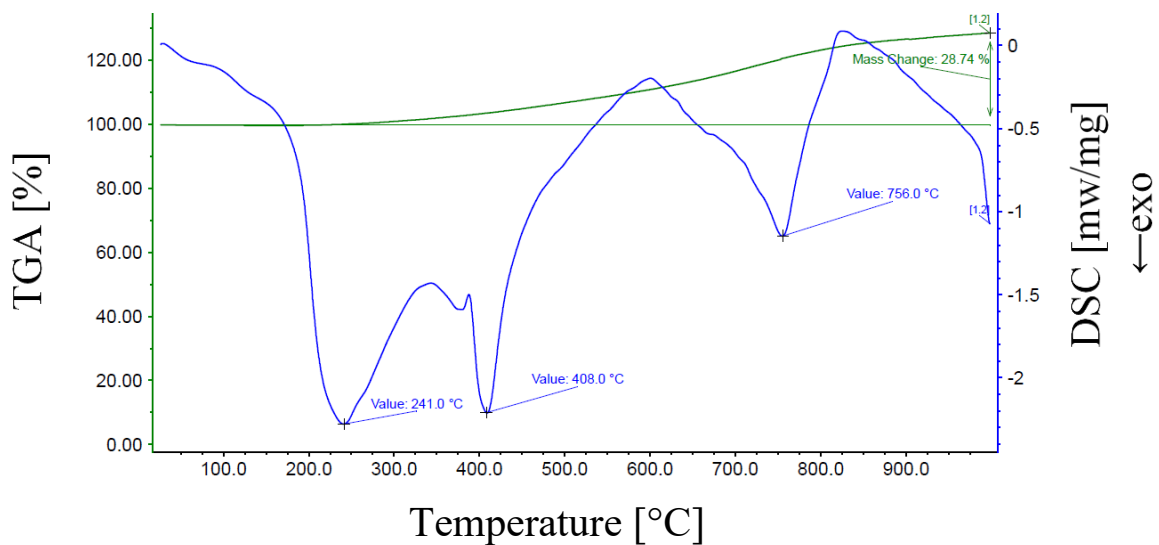


Figure 5.8: DSC/TGA results of 5hours-milled powder

10 hours milled:

Again, as showed by “Figure 5.9”, for 10 hours milled powder are visible three exothermic peaks centred in:

- 227 °C
- 354 °C
- 800 °C (the analysis only goes up to 800 °c, but it is clearly visible an exothermic peak around such temperature)

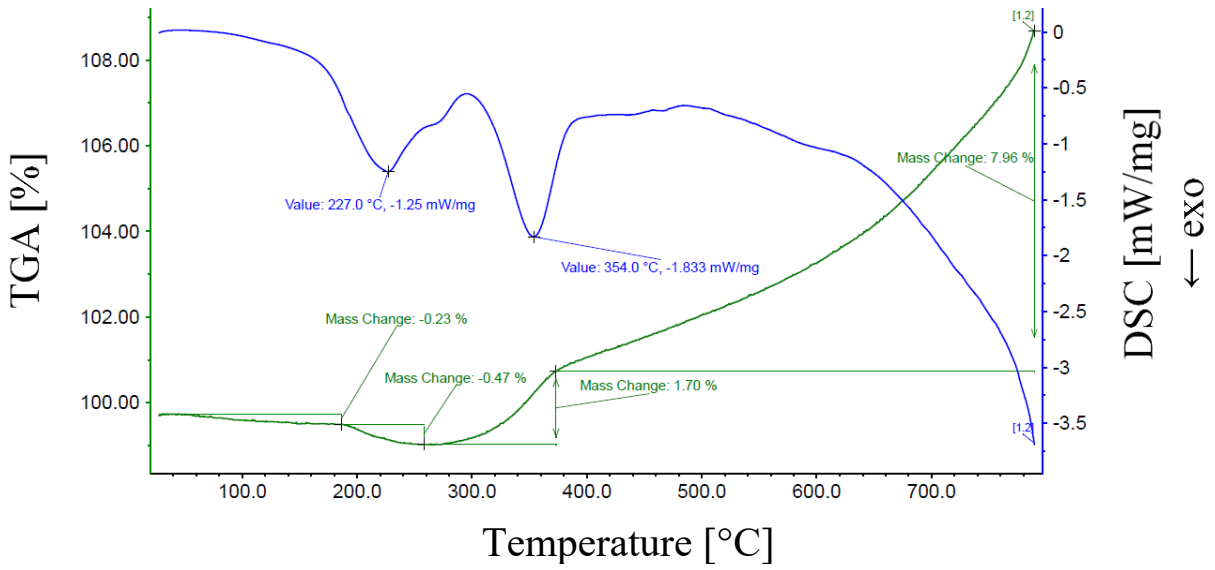


Figure 5.9: DSC/TGA results of 5 hours-milled powder

5.5.2 DSC results comparison and discussion:

The previous DSC results are grouped and showed by “Figure 5.10”.

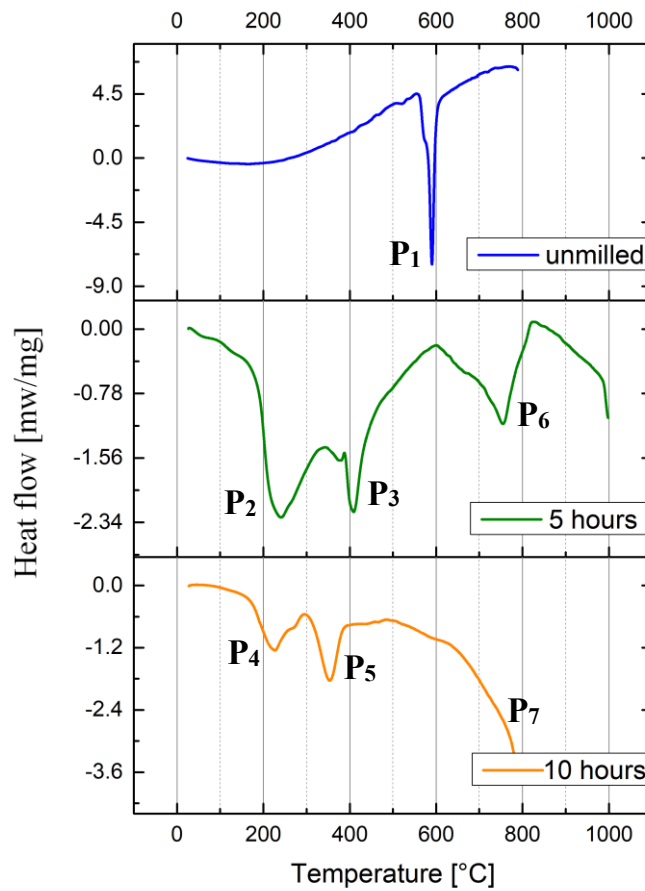


Figure 5.10: DSC results comparison

Considering temperature below 600 °C, the outcomes are very similar to many publications found in literature: one sharp peak (P₁) for unmilled powder, two broader peaks (P₃ and P₄, P₅ and P₆) for milled powder at temperatures lower with increased milled time. For instance, *Wang and Qin* [29] (reported in “Chapter 3”, “Figure 3.4”) observed a very similar behavior. The authors proved that those peaks are ascribable to alloy formation. However, the authors couldn’t obtain complete Mg₂Si formation with annealing operated at the lowest temperature peaks. Anyhow, assuming that those peaks are ascribable to magnesium silicide formation: it is clear that increasing milling time, reaction temperature decreases. This indicates that mechanical process activates the reaction, even it doesn’t lead to the Mg₂Si formation itself.

For temperatures above 600/700 °C were considered only Peaks P₆ and P₇. These peaks, according to [57, 58] are referred to the formation of magnesium nitride.

5.5.3 TGA results comparison and discussion:

Simultaneously with DSC also thermogravimetric analysis (TGA) was performed. Outcomes are showed in “Figure 5.11”. In all cases it was observed an increase of mass along the temperature, even though with some differences.

- For unmilled powder, it was risible (less than 1 %) up to ~ 470 °C, moderate (less than 3 %) up to ~ 480 °C, increasing then exponentially (~ 5 % at ~ 590 °C in correspondence of the exothermic peak, up to ~ 20 % at ~ 800 °C).
- For 5 hours milled, it was observed a faster increase of mass, compared with the other cases. However, in absolutes terms in correspondence of the second exothermic peak (~ 408 °C) the increase of mass was of ~ 3 %. The mass increased then exponentially reaching increase of ~ 23 % and ~ 28 % at respectively ~ 800 °C and ~ 1000 °C.
- The 10 hours milled powder showed the less marked increase of mass: practically none at ~ 354 °C, temperature of the second exothermic peak; moderate (~ 3 %) at ~ 590 °C. More important (~ 8 %) at ~ 800 °C.

At higher temperature (above 600/700 °C), it is thought that the increase of mass is due to nitrification [57, 58], however this hypothesis hasn’t been proved by analysis. For lower temperatures (operating annealing temperatures, described in the next paragraphs), no nitrides were found in the after-annealing powders. While some oxidation it was observed: so, at least up to 600 °C, it can be concluded that the rise of mass is due to the formation of oxides (especially MgO). This will be discussed more in detail in the following section though, it is already an indication of how challenging is avoiding the formation of magnesium oxide, even operating in inert atmosphere.

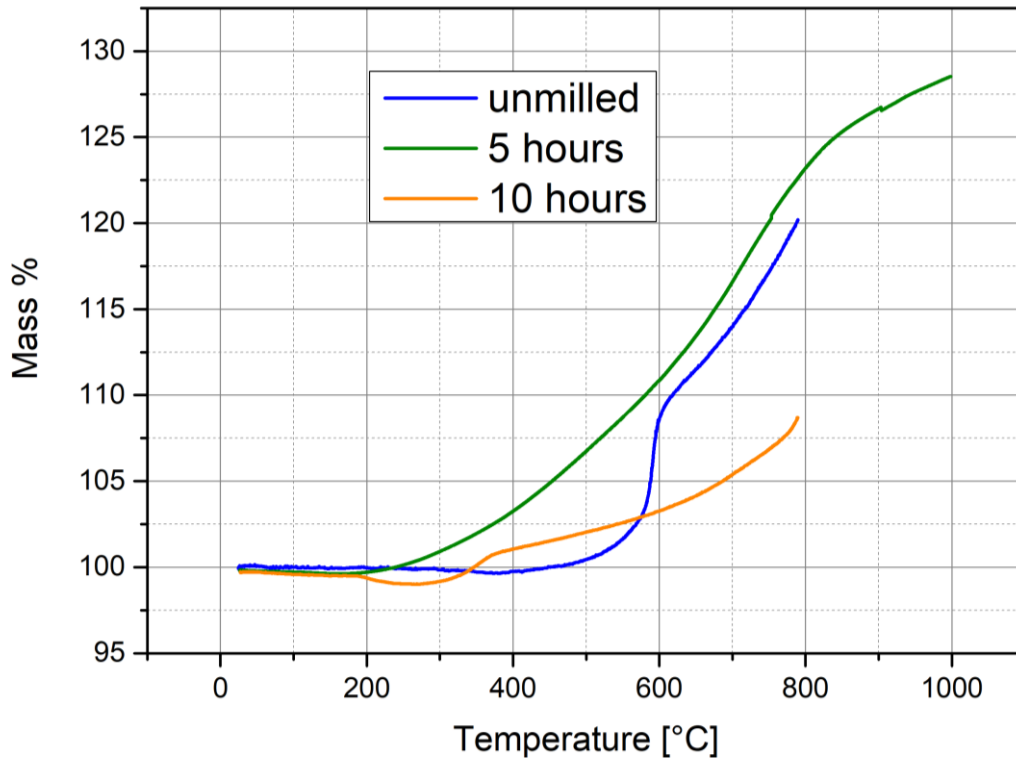


Figure 5.11: TGA results comparison

5.6 Mg₂Si formation reaction by thermal annealing and inert atmosphere comparison

According with the presented results, it was decided to perform annealing aimed: to prove the Mg₂Si formation, starting from 5 hours milled powder. It was decided firstly to test the Peak “P₃” (~ 408 °C), performing the annealing at this temperature. It was also decided to test and compare different inert atmospheres (vacuum, nitrogen and argon).

In a second time, another annealing in Nitrogen atmosphere was performed starting from unmilled powder, “testing” the peak “P₁”. This was done to verify if P₁ is really ascribable to magnesium silicide formation or if it has to be associated with nitride formation. As it will be further showed, it has been proved that the tested annealing temperatures lead effectively to formation of, mainly, Mg₂Si.

5.6.1 Experimental setting

For completing the formation reaction between magnesium and silicon a thermal treatment was performed, according with the DSC results. A tubular oven was used with a PID (proportional integral-differential) control unit. The temperature was also monitored by an external thermocouple. The oven is showed in “Figure 5.12”. The various crucibles used are showed by “Figure 5.13”.



Figure 5.12: Tubular oven used for annealing



Figure 5.13: Picture of the alumina crucibles used.

5.6.2 Five hours milled powder

Annealing temperature: 410 °C

There were tested three different inert atmospheres: vacuum, nitrogen and argon. The followed procedure was the same for the three atmospheres.

- 0.5 g of powder (5 hours milled) were loaded inside an alumina crucible (boat-type or cylindric). Since the powder was stored in the glovebox, this operation happened in argon atmosphere.

- The crucible was extracted out the glovebox and inserted into a quartz tube that was then connected to the vacuum system/gas inlet tube. This operation couldn't be avoided to be performed in air, but it lasted only few minutes; after that an inert atmosphere was loaded into the quartz tube and the tubular oven was set in position.
- The oven was set to go from room temperature up to 410 °C in 15 minutes, temperature that was held for 75 minutes. It was also programmed a cooling from 410 °C to room temperature in 30 minutes; however, in that amount of time it was never reached room temperature so, at the end of the 30 minutes, the oven was turned off, and “removed” leaving the quartz tube (still with inert atmosphere inside) in contact with external atmosphere until reaching room temperature (“Figure 5.14”).



Figure 5.14: Picture of the quartz tube still fixed on the support, after the oven was slid away in the end of thermal treatment. The tube was removed, and the crucible extracted only after reaching room temperature. The cooling, so, could happen while inside the tube the atmosphere was still inert.

- The quartz tube was then removed, the crucible extracted and then placed inside the glovebox, where the annealed powder was stored. Before storing, a small amount of powder was examined in air, where no pyrophoricity was observed in all cases.

Nitrogen atmosphere

The nitrogen flux inside the tube was ~ 0.35 L/min. During the thermal treatment, the external thermocouple measured $\sim 60/70$ °C more than the indicated temperature from the oven. After the thermal treatment, some observations were yielded:

- The powder showed two areas with two different colors (visible in “Figure 5.15” (2)); one grey/brown closer to the gas inlet. The other one (bigger), dark blue on the side of the crucible more far from the gas inlet.
Analysis showed that the blue powder is mainly magnesium silicide while the grey powder presents a huge amount of magnesium oxide. It was hypothesized that the gas, that is not pre-heated, flowing inside the tube creates a “cold zone” in the area proxime to the inlet. There, the temperature doesn't reach a value high enough for the reaction to happen, leaving behind unreacted Si and Mg that oxidized during the treatment or successively.

- It was observed a considerable increase of volume (observable in “Figure 5.16” (2) compared with (1));

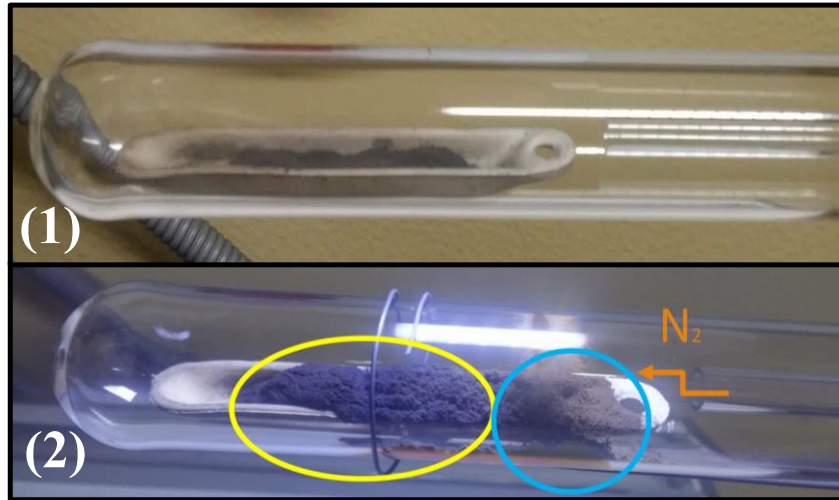


Figure 5.15: Pictures of the crucible inside the quartz tube before (1) and after (2) thermal treatment in N_2 atmosphere. After the annealing it is visible an increase of volume of the powder inside the crucible and at the same a color difference is visible (blue and grey/brown, left and right side).

Argon

The argon flux inside the tube was ~ 0.35 L/min. Again, during thermal treatment, the temperature measured by the external thermocouple was $\sim 60/70$ °C higher than the one indicated by the oven. The observations made in the previous case (nitrogen annealing) are valid for this case too. The crucible containing the powder before and after annealing is showed in “Figure 5.16”.



Figure 5.16: Pictures of the crucible inside the quartz tube, before (1) and after (2) argon annealing. After the treatment it is visible an increase of volume of the powder inside the crucible and at the same a color difference is visible (blue and grey/brown, left and right side).

Vacuum

There were performed three different annealing in vacuum atmosphere. In the first, it was used the same crucible of the previous treatments. In the second, a cylindric crucible was used. In these two situations 0.5 g of powder were used. The vacuum pressure varied between 10^{-5} and 10^{-6} mbar. For the third annealing 4 g of powder were loaded inside a bigger boat-type crucible. In this case it has been experienced to work with a vacuum grade lower than before, trying to avoid magnesium evaporation (working pressure between 10^{-3} and 10^{-4} mbar).

The major observations are:

- In all cases magnesium evaporation couldn't be avoided; as showed by "Figure 5.17" in all cases a "shroud" deposited on tube walls. This shroud is made of Mg. The tube was cleaned with an aqueous solution of nitric acid (that is reactive with magnesium), and the halos were successfully removed (almost instantaneously). Analysis will later confirm that.

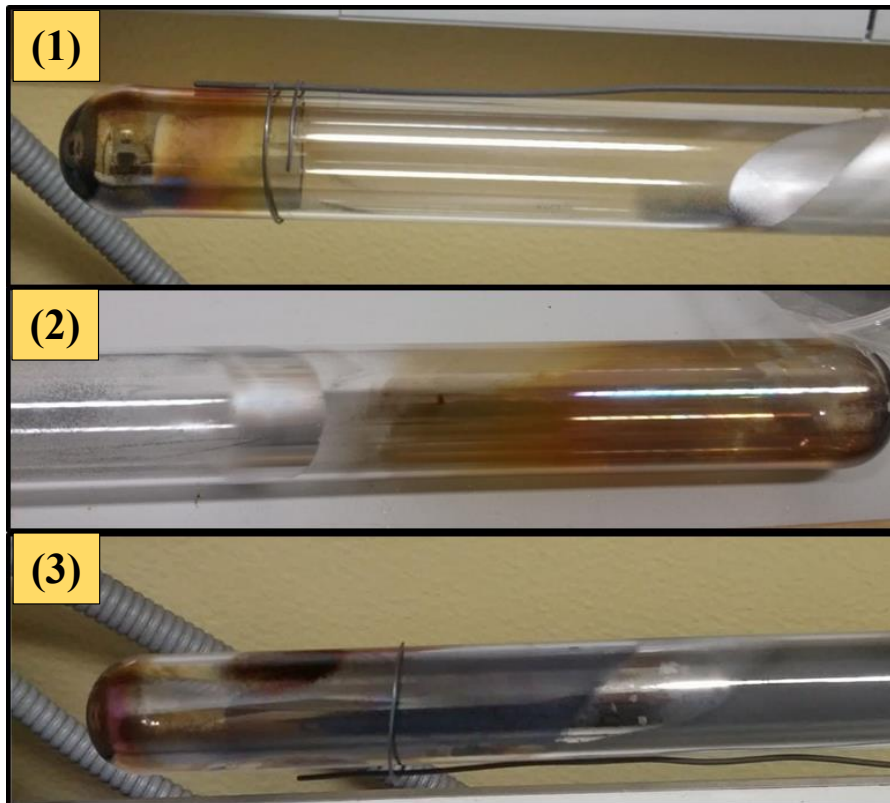


Figure 5.17: Quartz tube "dirty" after Mg being evaporated during annealing in vacuum (first vacuum annealing (1), second (2) and third (3)).

- In all cases, a certain amount of powder was found out the crucible along the tube, as shown in "Figure 5.18".

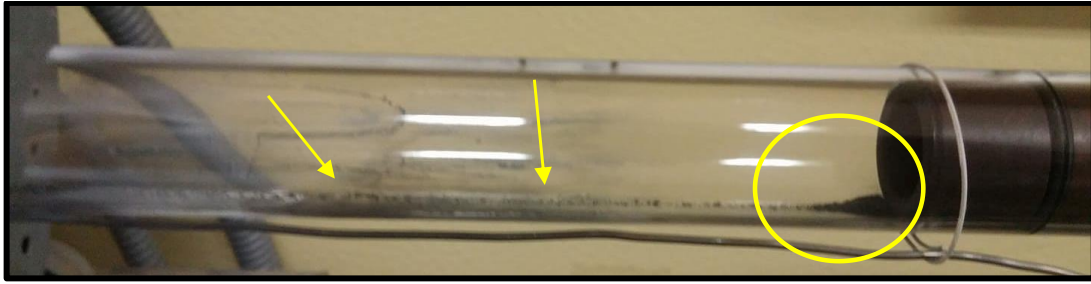


Figure 5.18: Powder that was dragged along the tube during annealing in vacuum.

- No difference in colors was observed (all the powder left inside the crucible looked dark blue), corroborating so, the hypothesis about the origin of the color difference in argon and nitrogen atmosphere. In vacuum, in fact, no “cold gas” is flowing inside the tube.
- No considerable amount of volume was observed even if, considering the amount of powder outside the crucible, it is hard to say.

5.6.3 Synthesis from commercial powder (unmilled)

Following the same procedure of the others thermal treatments, it has been performed another annealing starting from unmilled powder. The difference was that the used annealing temperature was 590 °C. The other parameters (heating time, hold time, cooling time) were maintained. The annealing was performed in nitrogen atmosphere.

The annealed powder was a stoichiometric composition (2 Mg, 1 Si); it was well blended inside the glovebox for 1.5h with a small mill/blender. 0.5 g of the blended powder were loaded inside the small boat-type crucible and 1g was inserted into the cylindric crucible. The two crucibles were then placed inside the quartz tube as showed in “Figure 5.19”.



Figure 5.19: Alumina crucibles containing a mixture of Mg and Si powder, inside the furnace quartz tube

After the annealing it was observed no difference in color, for the powder that was inside the cylinder (all blue), while a difference was observed in the powder that was inside the boat-type crucible. The difference was comparable to the previous cases (blue – grey/brown, far – close the gas inlet). No important and visible increase of volume was observed.

5.7 Characterization of annealed powder

5.7.1 XRD results

The results shown in this section compare the XRD patterns of:

1. Silicon powder, magnesium powder and a mixture (mol ratio 1:2) of them (“Figure 5.20”)
2. Mg-Si powder mixture: unmilled, 5 hours milled and 10 hours milled (“Figure 5.21”)
3. 5 hours milled powder and annealed powder (vacuum, nitrogen and argon, “Figure 5.22”)
4. Blue and grey powder of nitrogen and argon annealing (“Figure 5.23” and “5.24”)
5. In “Figure 5.25”, blue powder of nitrogen annealing (milled powder) and the powder obtained with unmilled (only mixed) powder (powder annealed in the cylinder-type crucible and blue and grey powder annealed in the boat-type crucible).

In all the presented patterns, peaks are identified in the following way:

- Silicon
- Magnesium
- Δ Magnesium Silicide
- * Magnesium Oxide

Outcomes:

1. The pattern of a powder mixture (mol: 2 Mg, 1 Si), is a combination of the patterns of silicon and magnesium.

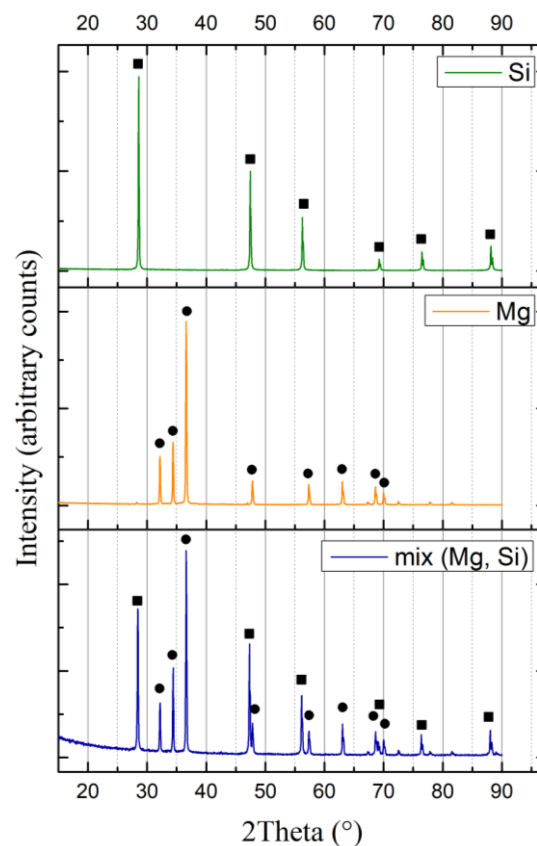


Figure 5.20: XRD patterns comparison between Si, Mg and mixture 2 Mg-1 Si

2. The unmilled mixture pattern was used to compare the pattern of the milled (5 hours and 10 hours) powder. The only peaks in the XRD patterns are ascribed to Mg and Si ones, indicating no formation of new phases. These results show that Mg_2Si didn't form by mechanical alloying. However, the effect of milling has been already discussed in "Paragraph 5.3".

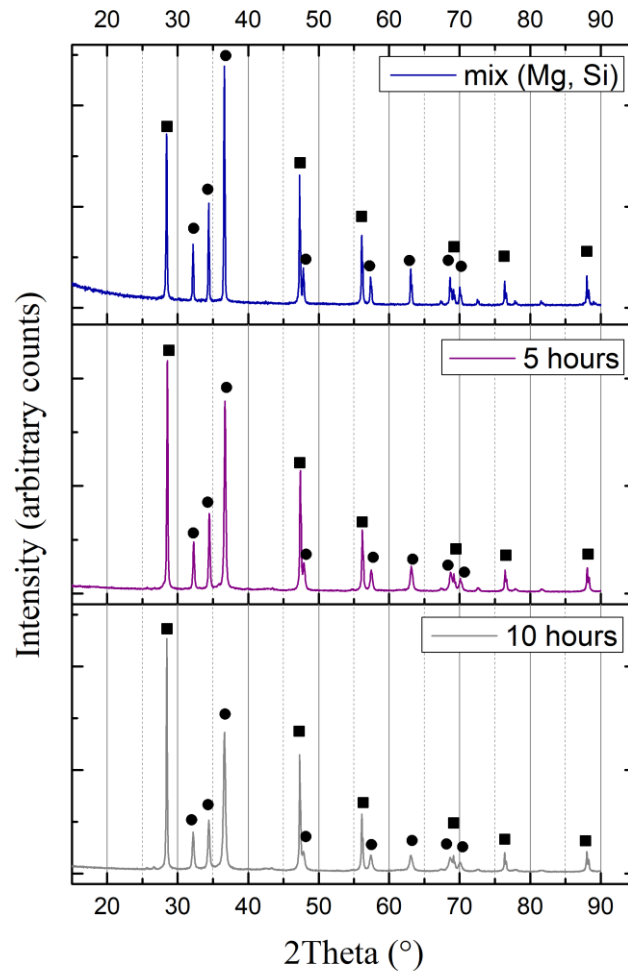


Figure 5.21: Comparison of mixture Mg-Si before milling and after 5 and 10 hours of milling.

3. The XRD showed that magnesium silicide formed after annealing in all the three different atmospheres tested, in particular.
- Peaks referable to Mg_2Si appear
 - Magnesium peaks disappear completely
 - Silicon peaks reduce considerably, even though two peaks ($\sim 28.8^\circ$, 56°) are still visible
 - Magnesium oxide peaks are slightly visible, even though very flat.

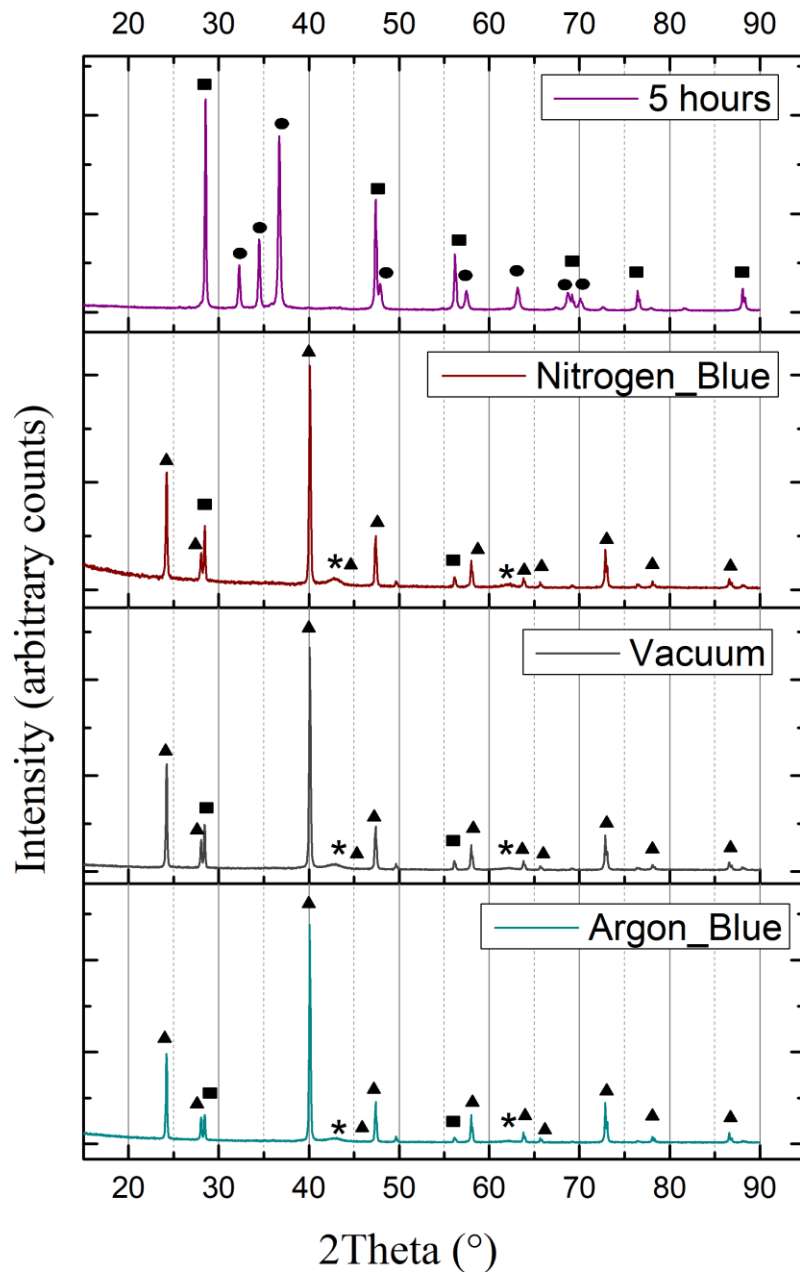


Figure 5.22: XRD patterns of powder milled 5 hours, before any thermal treatment and powder (previously milled 5 hours) annealed in the three different atmosphere tested (N_2 , argon and vacuum)

4. In the cases (nitrogen and argon atmosphere) where it was found a difference in powder color, the outcome (“Figure 5.23” and “Figure 5.24” respectively) of XRD analysis was similar. Grey powder presents an increase content of magnesium oxide. It is visible a correspondence with the peaks (Mg_2Si and Si) of “blue powder” with a remarkable increase of the ones related to MgO . These peaks are the only ones marked (*) in Figures “5.24” and “5.25”, since it is the only notable variation between “blue” and “grey” powder.

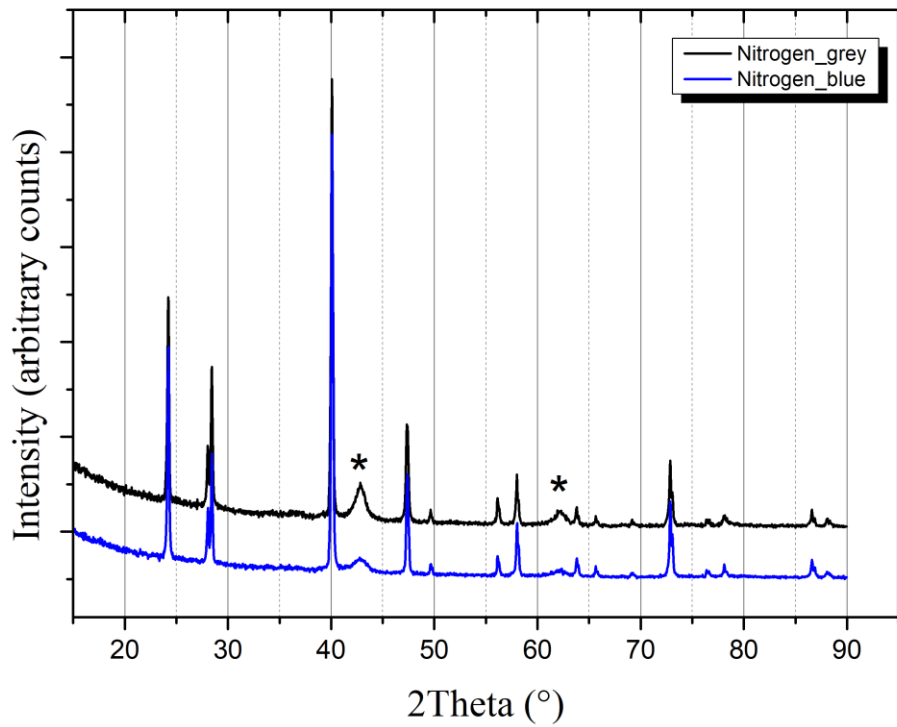


Figure 5.23: Comparaton between nle and grey powder after annealing in nitrogen atmosphere

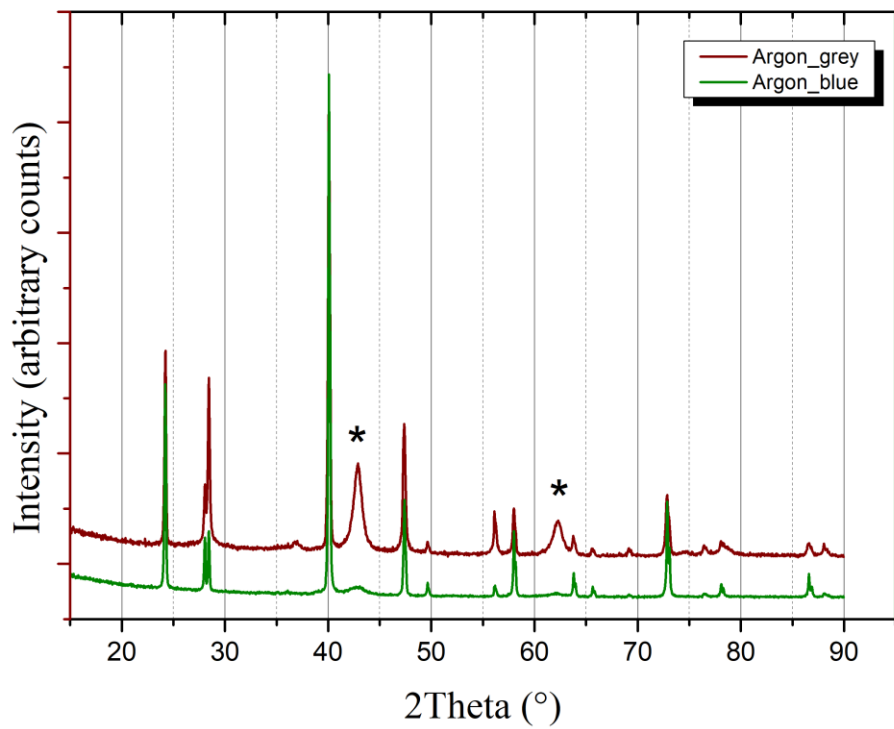


Figure 5.24: Comparaton between blue and grey powder after annealing in argon atmosphere

The data were plotted using the software ‘Origin Pro 9.1’, they were also analyzed by using the software ‘Match!’ and ‘Maud’ for the identification of the peaks. Maud allows also to quantify the percentage of the various phases presents in the powder, by Rietveld refinement. The calculated percentages are reported in “Table 5.4”.

Table 5.4: Weight percentage of phases calculated with the software Maud

| | Si wt % | Mg wt % | Mg ₂ Si wt % | MgO wt % |
|----------------------|---------|---------|-------------------------|----------|
| Mix 2Mg/1Si | 41.53 | 58.47 | / | / |
| 5hours | 40.05 | 59.32 | / | 0.63 |
| 10hours | 38.28 | 60.89 | / | 0.83 |
| Vacuum | | | | |
| Vacuum | 11.39 | / | 83.58 | 5.03 |
| Nitrogen_blue | 13.22 | / | 80.43 | 6.35 |
| Nitrogen_grey | 13.77 | / | 55.56 | 30.67 |
| Argon_blue | 7.41 | / | 88.47 | 4.12 |
| Argon_grey | 14.81 | / | 35.91 | 49.28 |

After milling (5 and 10 hours), the amount of MgO is rather low (less than 1 %), even though no magnesium oxide is detected in the unmilled powder. However, the amount of oxide increases considerably after annealing in the three different atmospheres.

After annealing, the predominant phase is Mg₂Si with some differences:

- Blue powder of argon and nitrogen annealing, and vacuum-annealed powder have similar outcomes. Predominant phase is Mg₂Si, with a certain percentage of silicon. Magnesium oxide is found to be in a percentage from 4 to 6 %.
- For grey powder (Ar and N₂ annealing) the amount of magnesium oxide is significant. The magnesium that oxidize is not available anymore for reacting with silicon. Consequently, the amount of unreacted Si results to be bigger and the amount of formed Mg₂Si lower.

In “Table 5.5” are reported the characteristics values of the Mg₂Si peaks of “Figure 5.22”. In detail, the peaks have been fit using the automatic function ‘Pseudo Voigt’ of the software ‘Origin Pro 9.1’. Then, the full-width-at-half- maximum (FWHM) has been reported in the table and the position of the peaks (2θ) was used to calculate the interplanar distance (d_{exp}) by using the Bragg law, already presented in Chapter 4, Equation (4.1) but reported for simplicity again in Equation (5.1).

$$d_{exp} = \frac{\lambda}{\sin\theta} \quad (5.1)$$

The peaks were also identified by using the miller indexes (h, k, l) from which it was possible to calculate the theoretical interplanar distance (d_{hkl}). Knowing that magnesium silicide has cubic crystal system, it is possible then to use Equation (5.2).

$$d_{hkl} = \frac{a}{\sqrt{h^2+k^2+l^2}} \quad (5.2)$$

By the same equation, it was possible also to calculate a_{exp} (experimental lattice parameter) substituting d_{hkl} with d_{exp} for each peak.

It is important to notice that in the table (in which are reported only the Mg_2Si peaks) the peaks are progressively numbered from 1 to 11. This numbers are not expressly reported in the patterns; however, it is not difficult to match them: notice that, in every case magnesium silicide peaks are marked (with a triangle), they are always eleven. The first one corresponds to number 1 in the table and so on. It may also helpful look at 2θ values in the table for an easier match.

Table 5.5: Characteristics values of the fitted magnesium silicide peaks (referring to “Figure 5.22”)

| $a = 6.351 \text{ \AA}$ $\lambda = 1.540593 \text{ \AA}$ | | ΔMg_2Si peaks | | | | | | | | | | |
|---|-------|-----------------------|-------|-------|-------|-------|-------|-------|-------|-------|-------|-------|
| Peaks identification | | 1 | 2 | 3 | 4 | 5 | 6 | 7 | 8 | 9 | 10 | 11 |
| Planes (hkl) | | 111 | 200 | 220 | 311 | 222 | 400 | 331 | 420 | 422 | 511 | 440 |
| 2θ | N_2 | 24.21 | 28.05 | 40.11 | 47.39 | 49.69 | 58.04 | 63.79 | 65.65 | 72.89 | 78.08 | 86.62 |
| | Ar | 24.21 | 28.05 | 40.10 | 47.40 | 49.66 | 58.02 | 63.82 | 65.65 | 72.86 | 78.08 | 86.61 |
| | Vac | 24.22 | 28.05 | 40.10 | 47.39 | 49.66 | 58.02 | 63.81 | 65.67 | 72.93 | 78.08 | 86.63 |
| FWHM | N_2 | 0.180 | 0.207 | 0.208 | 0.250 | 0.269 | 0.243 | 0.179 | 0.070 | 0.170 | 0.119 | 0.169 |
| | Ar | 0.162 | 0.157 | 0.191 | 0.223 | 0.081 | 0.139 | 0.224 | 0.090 | 0.114 | 0.120 | 0.124 |
| | Vac | 0.160 | 0.168 | 0.198 | 0.255 | 0.155 | 0.181 | 0.137 | 0.160 | 0.361 | 0.134 | 0.233 |
| $d_{exp} [\text{\AA}]$ | N_2 | 3.673 | 3.178 | 2.246 | 1.917 | 1.833 | 1.588 | 1.458 | 1.421 | 1.297 | 1.223 | 1.123 |
| | Ar | 3.673 | 3.179 | 2.247 | 1.916 | 1.834 | 1.588 | 1.457 | 1.421 | 1.297 | 1.223 | 1.123 |
| | Vac | 3.672 | 3.178 | 2.247 | 1.917 | 1.834 | 1.588 | 1.457 | 1.421 | 1.296 | 1.223 | 1.123 |
| $d_{hkl} [\text{\AA}]$ | | 3.667 | 3.176 | 2.245 | 1.915 | 1.833 | 1.588 | 1.457 | 1.420 | 1.296 | 1.222 | 1.123 |
| $a_{exp} [\text{\AA}]$ | N_2 | 6.361 | 6.356 | 6.354 | 6.357 | 6.351 | 6.352 | 6.354 | 6.355 | 6.352 | 6.354 | 6.353 |
| | Ar | 6.362 | 6.358 | 6.354 | 6.356 | 6.354 | 6.354 | 6.352 | 6.355 | 6.355 | 6.354 | 6.353 |
| | Vac | 6.360 | 6.357 | 6.354 | 6.357 | 6.354 | 6.354 | 6.353 | 6.353 | 6.349 | 6.355 | 6.352 |

In “Table 5.6” are reported the mean values of the experimental lattice parameters calculated with their standard deviation and compared with the theoretical value.

Table 5.6: Mean experimental lattice parameters calculated values

| a_{theo} [Å] | N_2 / a_{exp} [Å] | Ar / a_{exp} [Å] | Vac / a_{exp} [Å] |
|----------------|---------------------|---------------------|---------------------|
| 6.351 | 6.3544 ± 0.0029 | 6.3552 ± 0.0026 | 6.3544 ± 0.0029 |

5. Analysis proved that magnesium alloys form even starting with unmilled powder. These results (“Shown in “Figure 5.25”) are important because shows that nitrides (the annealing was performed in N_2 atmosphere) don’t form, even annealing at ~ 600 °C. XRD shows that blue and grey powder have similar spectrum to the previous cases. The comparison made by Figure 5.25 is between milled powder and subsequently annealed in nitrogen atmosphere (previously it has been referred to this with ‘Nitrogen Blue’) with the only mixed (unmilled) powder annealed at 590 °C in nitrogen atmosphere. Are reported analysis on the powder that was inside the cylinder-type crucible and the blue and grey powder that were inside the boat-type crucible (see “Paragraph 5.6.3”).

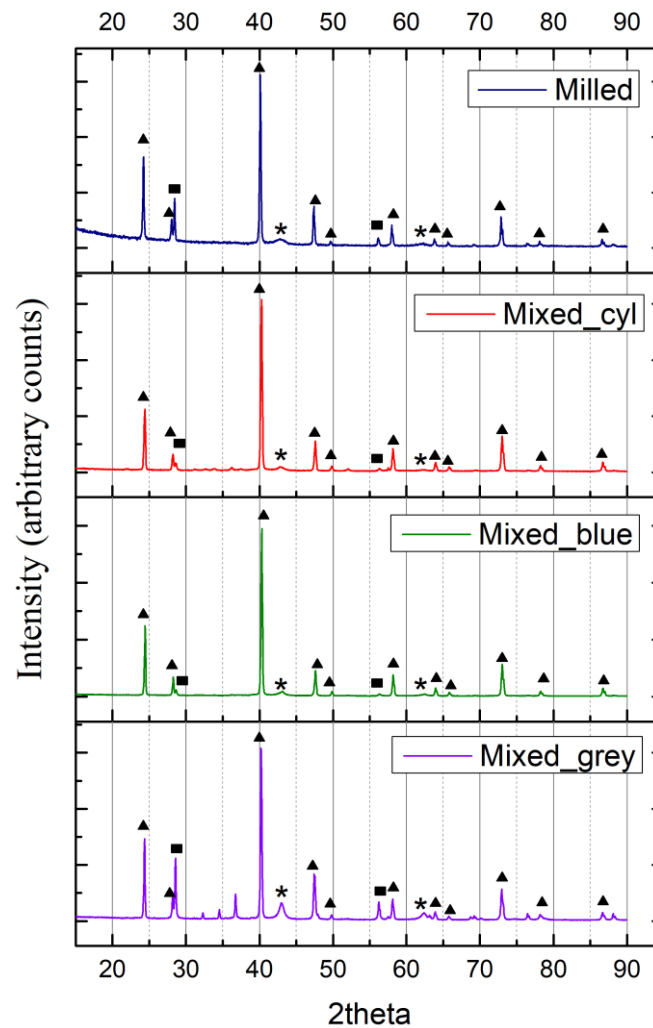


Figure 5.25: XRD Patterns of milled and unmilled subjected to thermal treatment in N_2 atmosphere.

Table 5.7: Phase percentages in the magnesium silicide obtained from unmilled powder, calculate by using software Maud

| | Si wt % | Mg wt % | Mg ₂ Si wt % | MgO wt % |
|----------------|---------|---------|-------------------------|----------|
| Mixed_cylinder | 4.22 | / | 91.87 | 3.91 |
| Mixed_blue | 3.27 | / | 90.89 | 5.84 |
| Mixed_grey | 17.69 | / | 53.18 | 29.13 |

Following the same procedure presented before, also for the Mg₂Si obtained from unmilled powder were calculated the characteristics values of the XRD peaks. All the considerations made are still valid. They are reported in “Table 5.8” and compared with the values of Mg₂Si obtained by milling and annealing in nitrogen atmosphere.

Table 5.8: Characteristics values of the fitted magnesium silicide peaks (referring to “Figure 5.25”)

| | | Mg ₂ Si peaks | | | | | | | | | | |
|----------------------|----------|--------------------------|-------|-------|-------|-------|-------|-------|-------|-------|-------|-------|
| Peaks identification | | 1 | 2 | 3 | 4 | 5 | 6 | 7 | 8 | 9 | 10 | 11 |
| Plane (hkl) | | 111 | 200 | 220 | 311 | 222 | 400 | 331 | 420 | 422 | 511 | 440 |
| 20 | Milled | 24.21 | 28.05 | 40.11 | 47.39 | 49.69 | 58.04 | 63.79 | 65.65 | 72.89 | 78.08 | 86.62 |
| | cylinder | 24.39 | 28.23 | 40.27 | 47.58 | 49.83 | 58.18 | 63.97 | 65.84 | 73.05 | 78.27 | 86.76 |
| | boat | 24.43 | 28.27 | 40.30 | 47.60 | 49.85 | 58.21 | 63.99 | 65.85 | 73.07 | 78.30 | 86.79 |
| FW HM | Milled | 0.180 | 0.207 | 0.208 | 0.250 | 0.269 | 0.243 | 0.179 | 0.070 | 0.170 | 0.119 | 0.169 |
| | cylinder | 0.231 | 0.331 | 0.244 | 0.274 | 0.300 | 0.307 | 0.311 | 0.358 | 0.365 | 0.589 | 0.267 |
| | boat | 0.187 | 0.185 | 0.216 | 0.252 | 0.154 | 0.280 | 0.331 | 0.305 | 0.357 | 0.404 | 0.454 |
| d _{exp} [Å] | Milled | 3.673 | 3.178 | 2.246 | 1.917 | 1.833 | 1.588 | 1.458 | 1.421 | 1.297 | 1.223 | 1.123 |
| | cylinder | 3.647 | 3.159 | 2.238 | 1.910 | 1.829 | 1.584 | 1.454 | 1.417 | 1.294 | 1.220 | 1.122 |
| | boat | 3.640 | 3.155 | 2.236 | 1.909 | 1.828 | 1.584 | 1.454 | 1.417 | 1.294 | 1.220 | 1.121 |
| d _{teo} [Å] | | 3.667 | 3.176 | 2.245 | 1.915 | 1.833 | 1.588 | 1.457 | 1.420 | 1.296 | 1.222 | 1.123 |
| a _{exp} [Å] | Milled | 6.361 | 6.356 | 6.354 | 6.357 | 6.351 | 6.352 | 6.354 | 6.355 | 6.352 | 6.354 | 6.353 |
| | cylinder | 6.316 | 6.318 | 6.329 | 6.334 | 6.334 | 6.337 | 6.339 | 6.339 | 6.341 | 6.341 | 6.344 |
| | boat | 6.305 | 6.310 | 6.325 | 6.331 | 6.332 | 6.335 | 6.337 | 6.338 | 6.339 | 6.339 | 6.342 |

5.7.2 Raman results

The outcomes of Raman spectroscopy are showed by “Figure 5.26”, where the various spectra are numbered as follow:

- (1) Powder milled for 5 hours before any thermal treatment
- (2) Powder 5-hours-milled and subsequently annealed in vacuum
- (3) Powder 5-hours-milled and subsequently annealed in nitrogen atmosphere (Grey powder)
- (4) Powder 5-hours-milled and subsequently annealed in nitrogen atmosphere (Blue powder)
- (5) Powder 5-hours-milled and subsequently annealed in argon atmosphere (Blue powder)
- (6) Powder 5-hours-milled and subsequently annealed in argon atmosphere (Grey powder)

The orange spectrum in (1) refers to the Raman analysis performed on milled powder before thermal treatment. In this spectrum the marked peaks (with orange line) refers to crystalline silicon. These peaks do not disappear from the spectra measured on the powder that was subjected to annealing. This is in agreement with the XRD analysis, where in all cases a certain amount of unreacted silicon has been always observed.

According to literature [72-74], the characteristic fingerprint of magnesium silicide shows peaks at Raman shifts in the ranges: $256\text{-}266\text{ cm}^{-1}$ and $345\text{-}357\text{ cm}^{-1}$ (measured with laser power between 3-5 mW and $\lambda=488\text{ nm}$). Then, in “Figure 5.26”, the two black lines refer to characteristic phonon peaks of Mg_2Si . These peaks have been detected in the annealed powder in many cases, with some differences:

- (4) many grains analysed presented mainly characteristics peaks referable to magnesium silicide and few showed a coexistence of Mg_2Si with silicon
- (3), (6) sharp and defined magnesium silicide peaks have been found in all grains scanned but always coexisting with peaks corresponding to silicon
- (2), (5) it has been more difficult to track grains presenting defined Mg_2Si related peaks, while silicon was more easily detectable

It has also been measured the spectrum of the glass sample-holder to evaluate eventual contribution in light scattering from it. However, this was not observed, leading to conclude that in no cases the measured spectra were influenced by that.

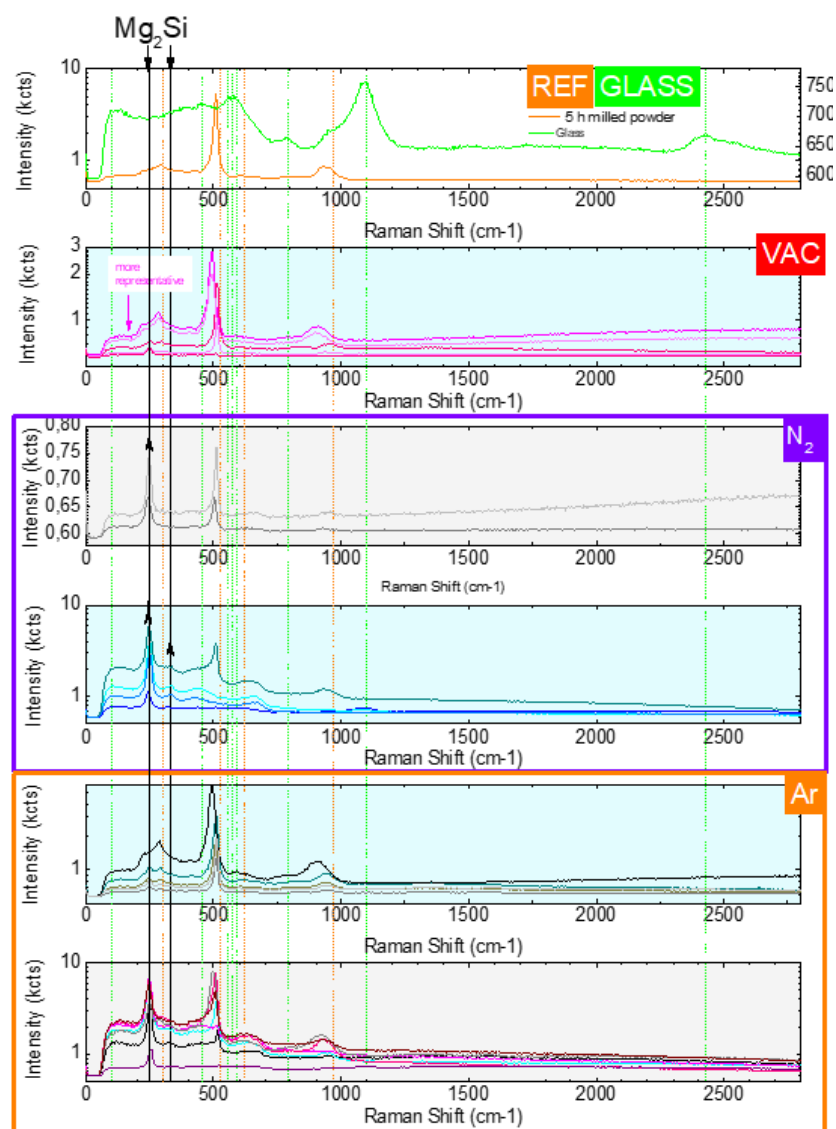


Figure 5.26: Raman spectra of annealed and non-annealed powder

5.7.3 IR results

Infrared spectroscopy was also performed, in Attenuated Total Reflection (ATR), on the same combination of samples that were analysed by Raman spectroscopy. Results are showed in “Figure 5.27”, “5.28” and “5.29”. This analysis gave complementary information of the previous analysis. The functional groups individuated are summarized by “Table 5.9”. In particular:

- At 397 cm^{-1} a peak (marked with A), referring to stretching vibrational mode of the bond Mg—O, has been detected both in the blue powders (including the one annealed in vacuum) and in the grey ones. Moreover, the spectra associated with grey powder present more intense peaks at this wavenumber, compared with blue powder spectra. This indicates a higher presence of magnesium oxide, in accord with XRD results. Furthermore, the milled powder at that wavenumber present a very small and slightly visible peak indicating a quantity of oxide sensibly lower.
- At 858 cm^{-1} and 995 cm^{-1} (peaks B and C), the functional group (SiO_4^{2-}) has been detected in the annealed-powder spectra, suggesting that formation of silicates happened

during the thermal treatments. The silicate that may have formed is Forsterite (Mg_2SiO_4). However, presence of Forsterite hasn't been detected by the others performed techniques.

- In the annealed-powder spectra, it has also been detected visible peaks (peak D) at $\sim 1434 \text{ cm}^{-1}$, associable with the bond C—C. This is may due to contamination from the milling fluid process (hexane).

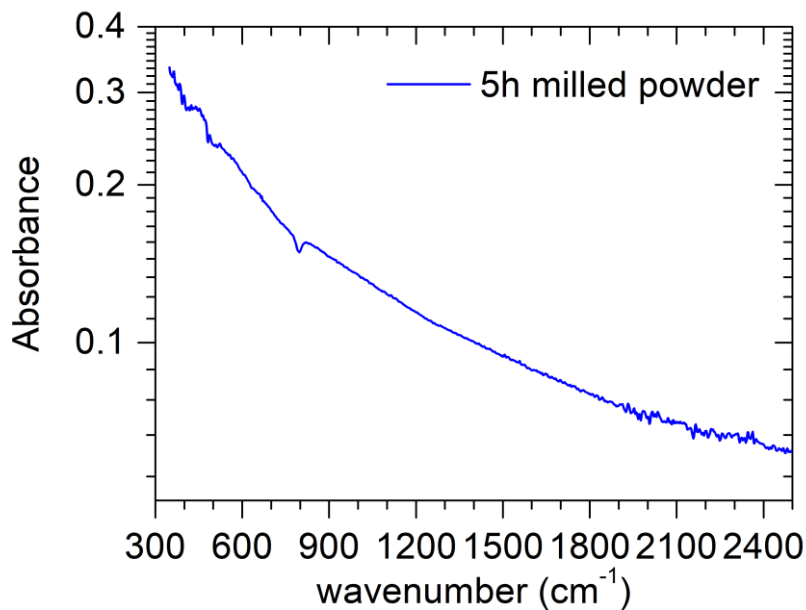


Figure 5.27: FTIR-ATR spectrum of 5hours milled powder

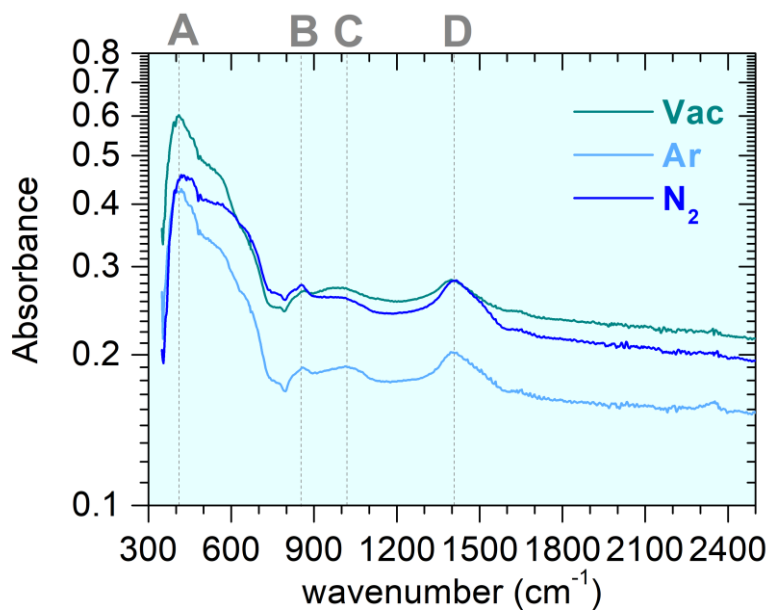


Figure 5.28: FTIR-ATR spectrum of annealed powder after milling. Comparison between nitrogen and argon blue and vacuum

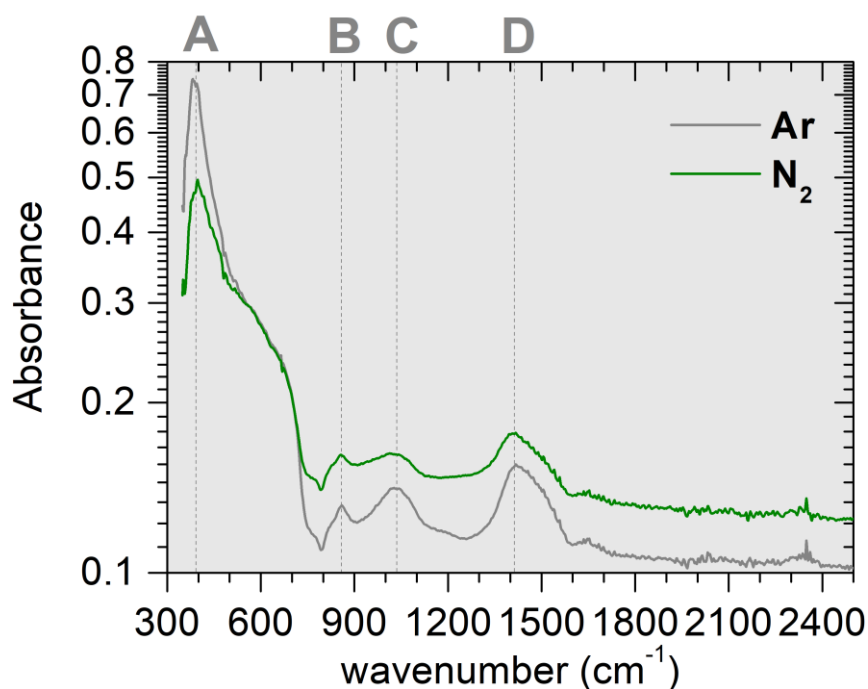


Figure 5.29: FTIR-ATR spectrum of nitrogen and argon grey powder

Table 5.9: comparison of the detected peaks positions with values reported in literature

| Symb. | Peak (cm ⁻¹) | | Functional group |
|-------|--------------------------|-----------------|--------------------------------|
| | measured | Literature [75] | |
| A | 397-410 | 400-430 | Mg-O |
| B | 858 | 860-890 | SiO ₄ ²⁻ |
| C | 1020-1037 | 980-1000 | SiO ₄ ²⁻ |
| D | 1400-1414 | | C-C |

5.7.4 SEM results

This section illustrates the images obtained by SEM analysis performed on:

- Silicon commercial powder (“Figure 5.30”)
- 5 hours milled powder before annealing (“Figure 5.31” and “5.32”)
- Blue powder obtained after N₂ annealing (“Figure 5.33” and “5.34”)
- Grey powder obtained after N₂ annealing (“Figure 5.35”)
- Blue powder obtained after argon annealing (“Figure 5.36” and “5.37”)
- Grey powder obtained after argon annealing (“Figure 5.38”)
- Powder after vacuum annealing (“Figure 5.39” and “5.40”)

Some of those images were analysed with the software ‘ImageJ’ to determine the size of the particles. Operation that was performed at least on 30 particles for each image analysed. Anyhow, it is not an easy operation due to the irregularity of the shape particles, of which was considered only the largest dimension. The results obtained are reported in “Table 5.10”.

Table 5.10: Resume of the particle size analysed

| | | |
|--|--|--|
| Silicon $13.50 \pm 7.50 \mu\text{m}$ | | |
| Mg-Si - 5h milled $8.83 \pm 5.28 \mu\text{m}$ | N ₂ annealing (Blue) $2.28 \pm 0.71 \mu\text{m}$ | N ₂ annealing (Grey) $2.54 \pm 0.87 \mu\text{m}$ |
| vacuum annealing $2.02 \pm 0.49 \mu\text{m}$ | Ar annealing (Blue) $2.19 \pm 0.73 \mu\text{m}$ | Ar annealing (Grey) $1.76 \pm 0.53 \mu\text{m}$ |

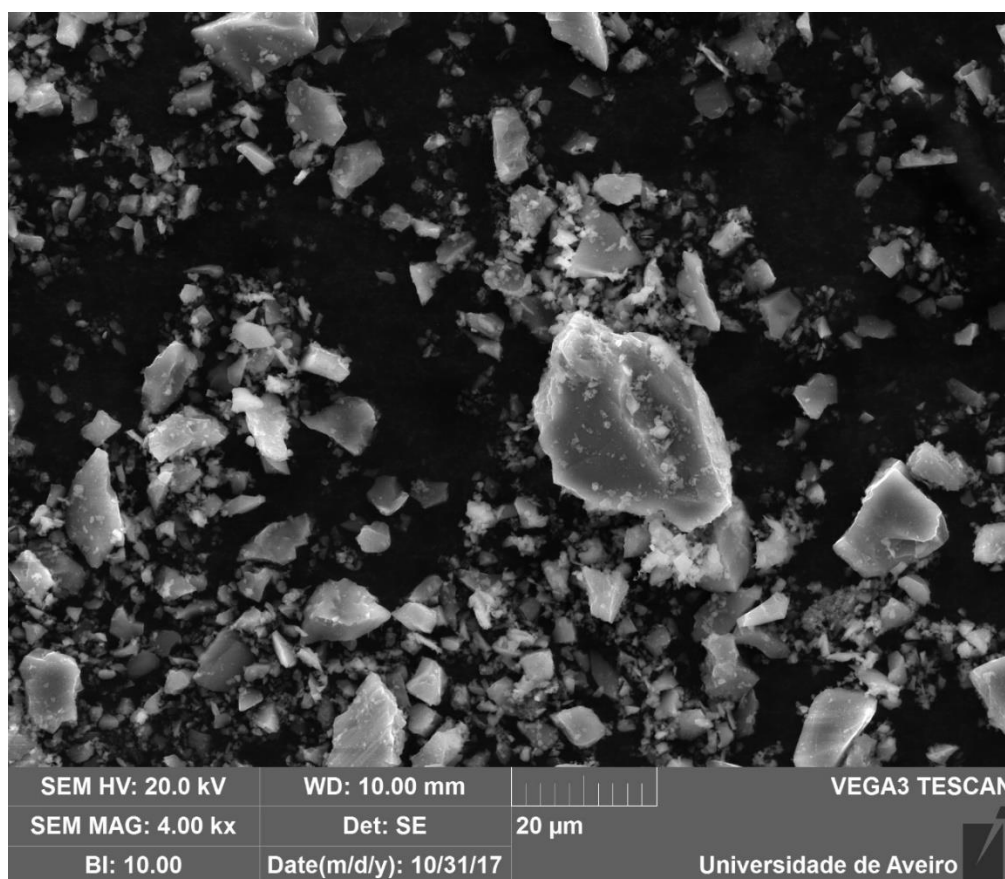


Figure 5.30: SEM image of commercial silicon powder

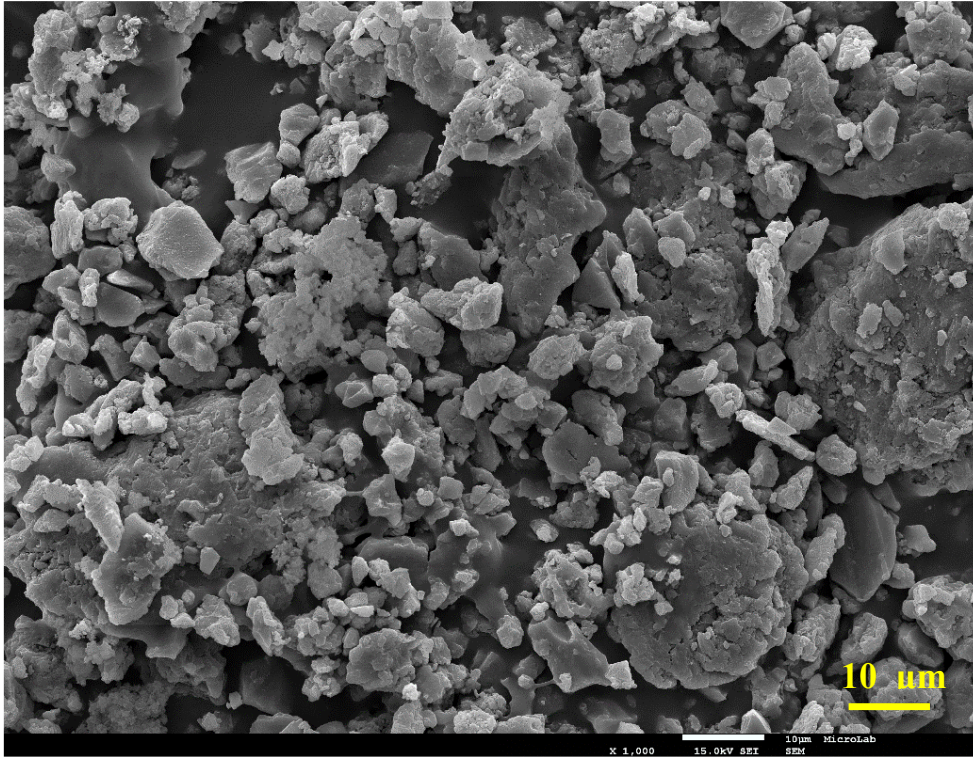


Figure 5.31: SEM image of 5 hours milled powder (magnitude 1000x)

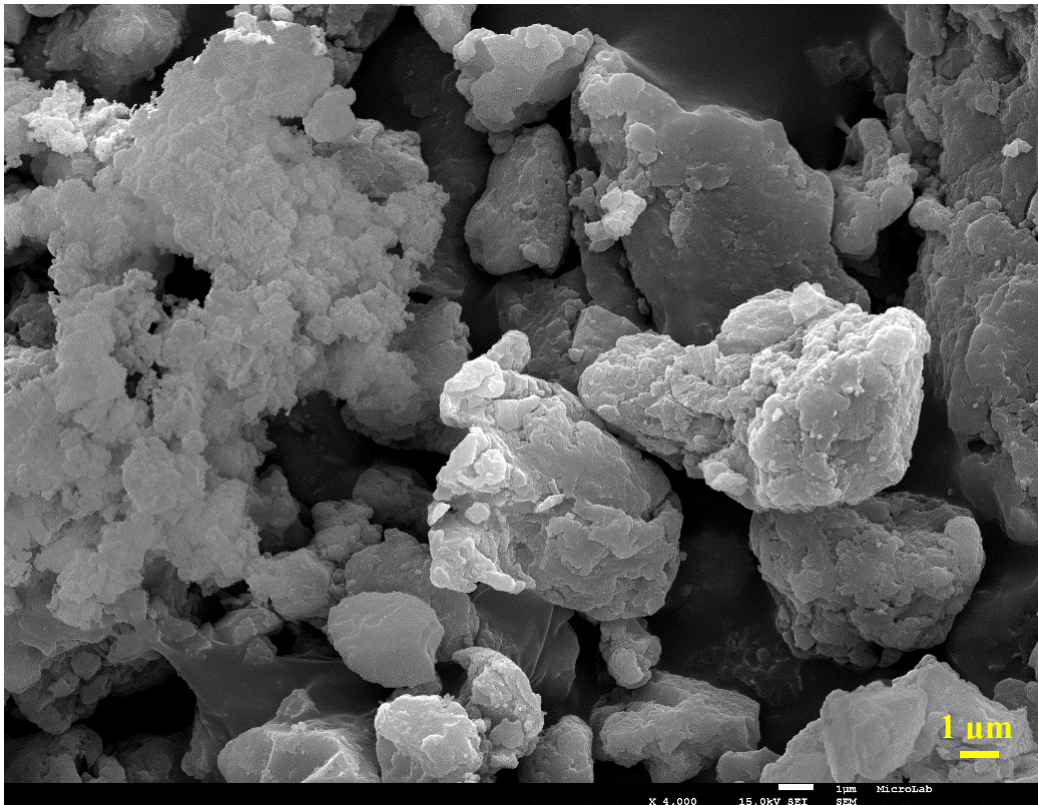


Figure 5.32: SEM image of 5 hours milled powder (magnitude 4000x)

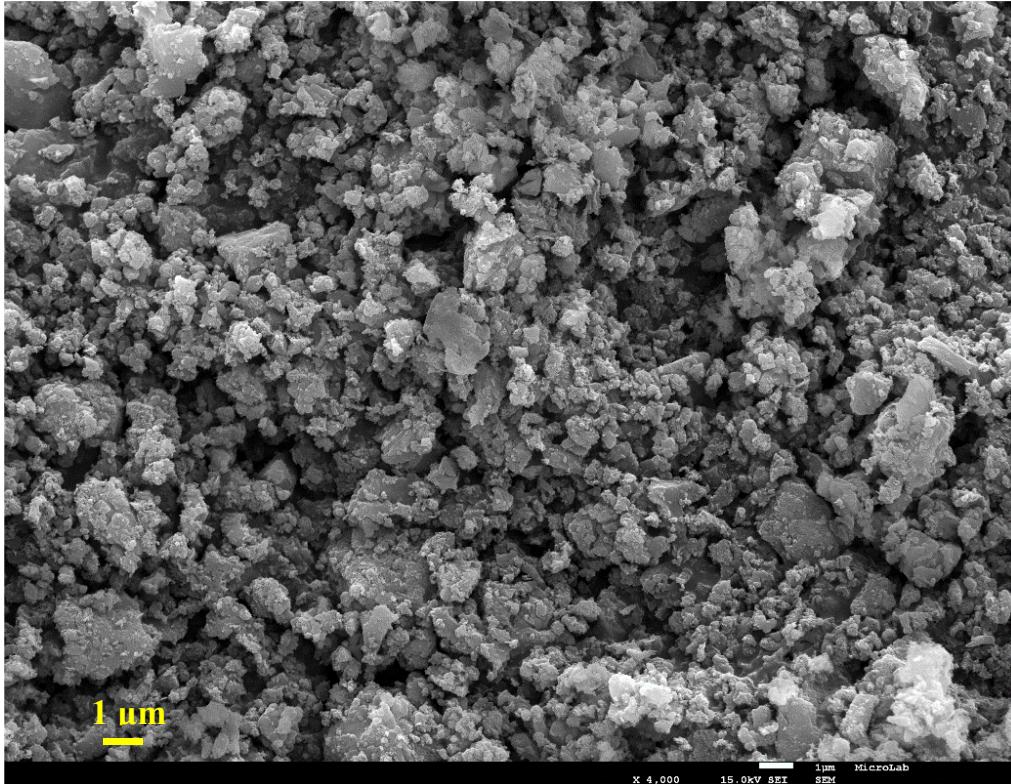


Figure 5.33: SEM image of powder subject to annealing in nitrogen atmosphere (blue powder) after 5 hours milling powder (magnitude 4000x)

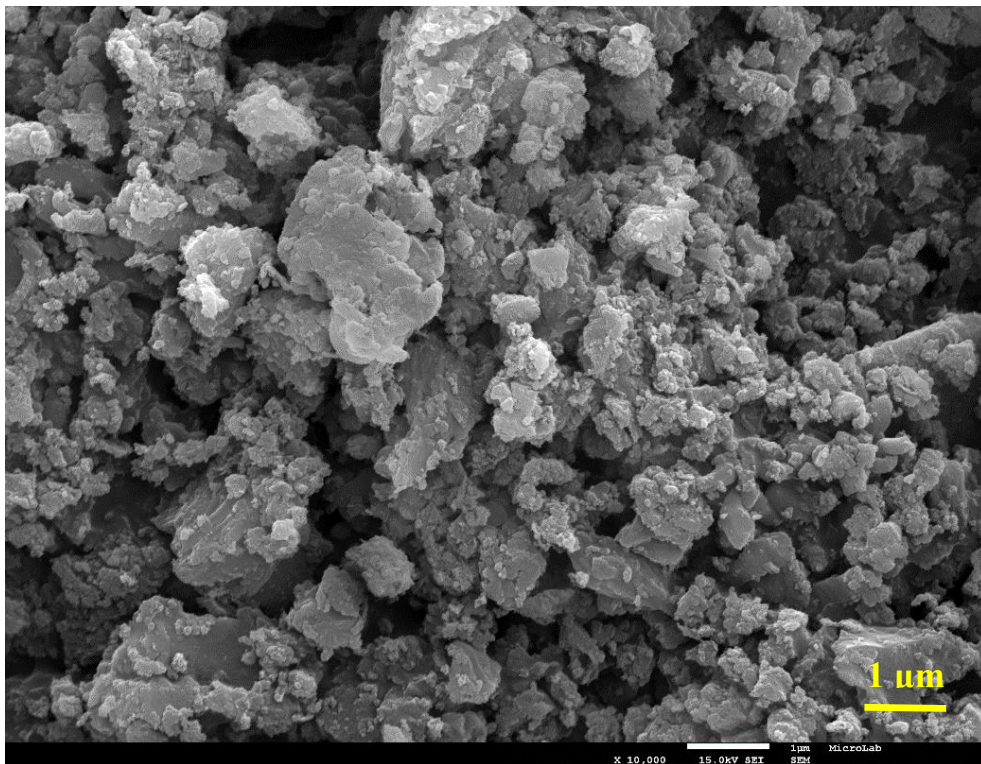


Figure 5.34: SEM image of powder subject to annealing in nitrogen atmosphere (blue powder) after 5 hours milling powder (magnitude 10000x)

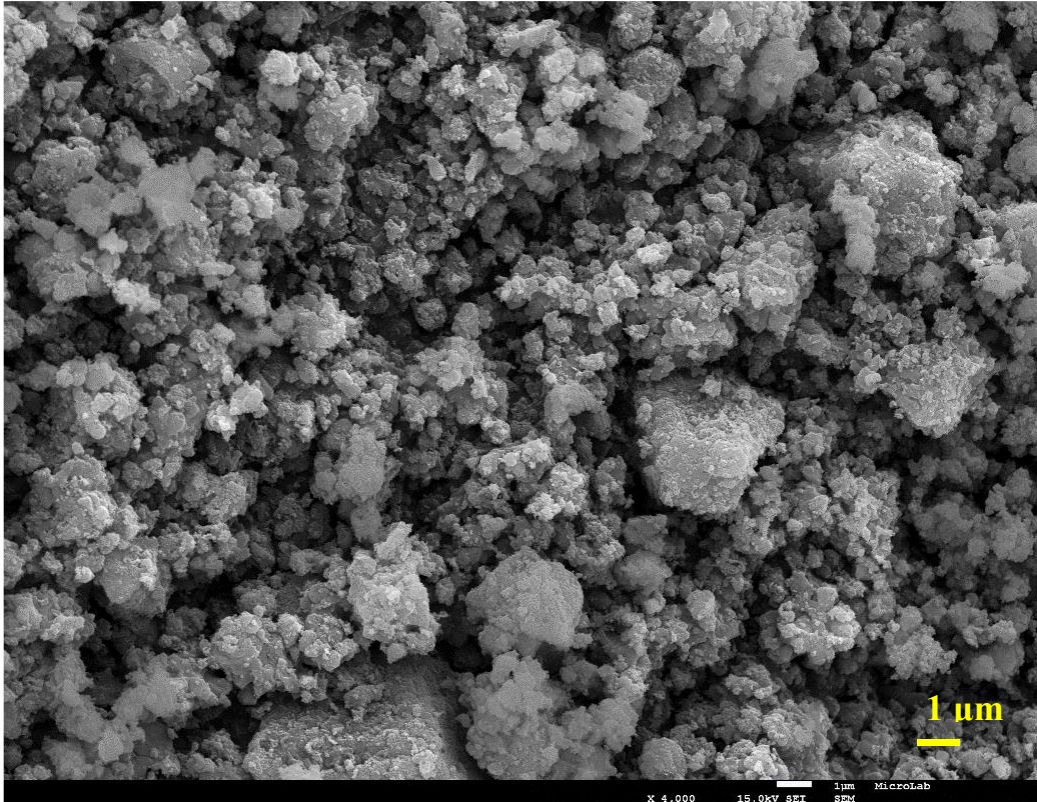


Figure 5.35: SEM image of powder subject to annealing in nitrogen atmosphere (grey powder) after 5 hours milling powder (magnitude 4000x)

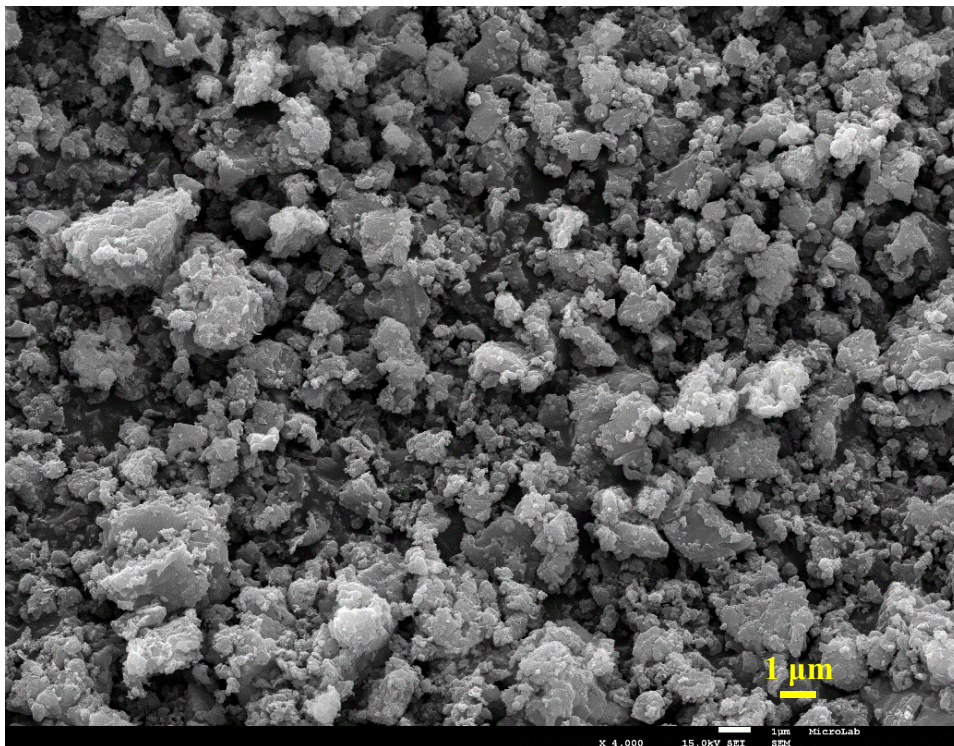


Figure 5.36: SEM image of powder subject to annealing in argon atmosphere (blue powder) after 5 hours milling powder (magnitude 4000x)

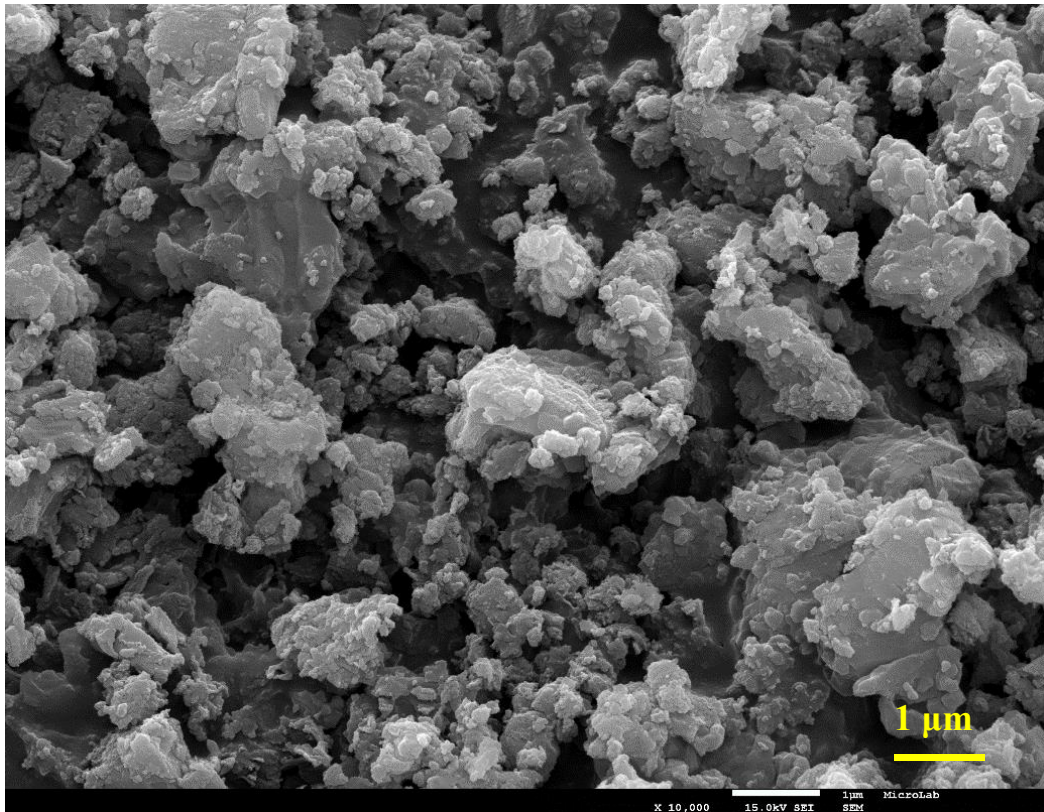


Figure 5.37: SEM image of powder subject to annealing in nitrogen atmosphere (blue powder) after 5 hours milling powder (magnitude 10000x)

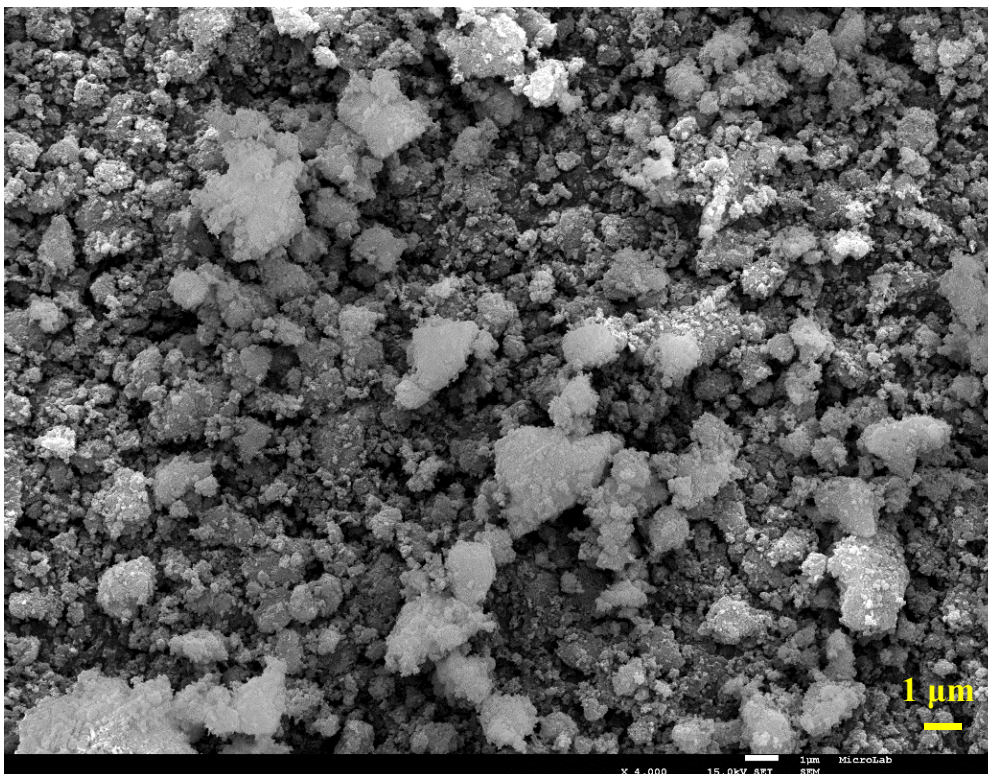


Figure 5.38: SEM image of powder subject to annealing in argon atmosphere (grey powder) after 5 hours milling powder (magnitude 4000x)

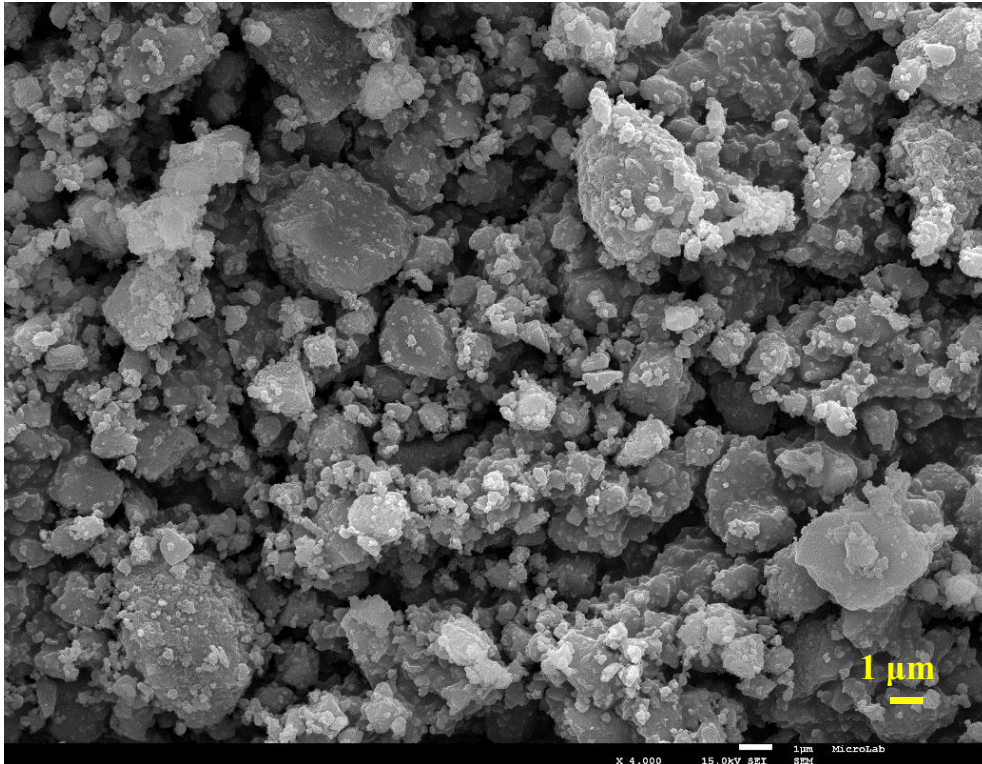


Figure 5.39: SEM image of powder subject to annealing in vacuum atmosphere (grey powder) after 5 hours milling powder (magnitude 4000x)

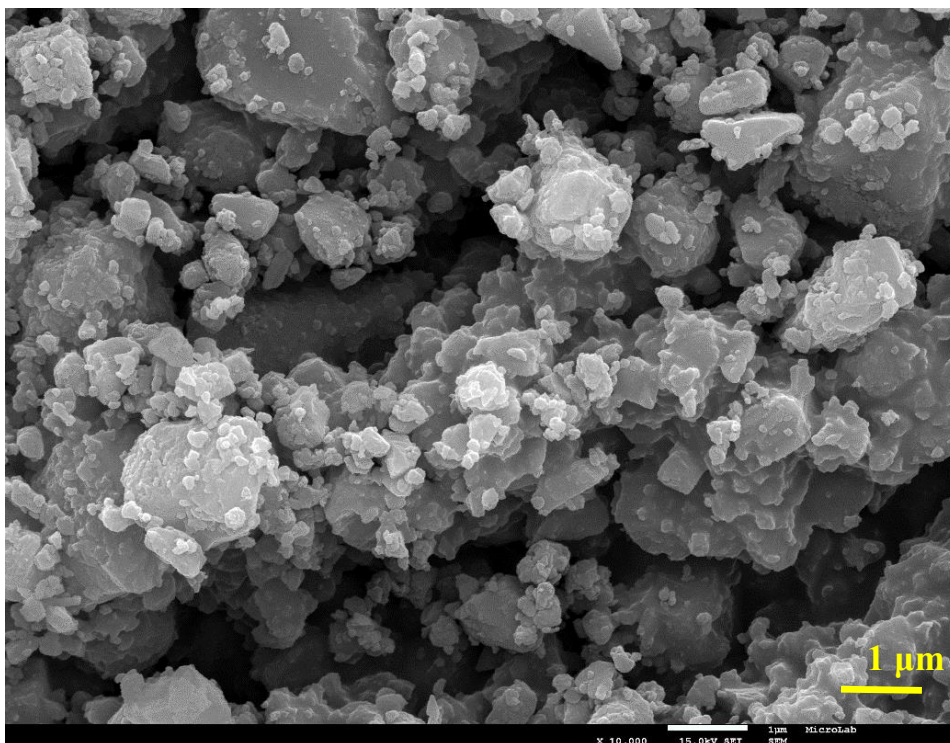


Figure 5.40: SEM image of powder subject to annealing in vacuum atmosphere (blue powder) after 5 hours milling powder (magnitude 10000x)

6 3d Printing of silicon and magnesium silicide powder

6.1 3d printing technologies

Additive manufacturing (AM) or 3D printing, known also as Rapid Prototyping (RP), is the process of producing three-dimensional objects directly from a three-dimensional Computer Aided Design (3D CAD) model [60-62]. AM fabricates parts by adding material layer by layer and each layer is a small cross-section derived from the CAD model. AM consists the production of objects from metals, ceramics, and polymers. It is, then, a very versatile method and it allows to obtain complex objects in a relatively short time. There are already available several and quite different AM technologies, classified in the following categories [60]:

- binder jetting
- material jetting
- direct energy deposition
- sheet laminations
- material extrusion
- powder bed fusion
- vat photo-polymerization

In this work, it has been used an extrusion-based system. It consists in the extrusion of a material in a fluid-like state from a nozzle, that dries or solidify after printing in a relatively short time.

There are different possible approaches for extrusion processes. A common one consists in manipulating the material state by controlling the temperature. The material is liquefied inside a tank or inside the printer itself, then it flows out the nozzle and bond with the material already extruded before solidifying. This is similar to conventional polymer extrusion processes.

Another possible approach, that is the one selected for this master thesis work, consists in the extrusion of a paste in a semi-solid state. The paste consists in a mixture of:

- inorganic powder (the material of interest), indicated with letter 'P'
- polymeric solution (solvent + polymeric binder) that confers the adequate viscosity to the paste, indicated with letter 'S'

Later on, it will be explained more in detail; the aim of this section is only to give the reader a better understanding of the used 3D printing system.

6.2 Experimental Setting: 3D Printer

The used printer is a self-assembled 3d printer. The functioning is quite simple and schematized in “Figure 6.1”; the printing paste is loaded into a syringe (1), that is inserted inside the printing cylinder (2). Pressure is applied to the material by a plunger (3), forcing the paste out the needle (1 mm or 1.5 nominal diameters). The pressure is kept constant, so the extruded material flows at a constant rate.

“Figure 6.2” and “Figure 6.3” show more in detail the printer, equipped with a hot bed and the syringe.



Figure 6.1: Detail of the printing cylinder and syringe

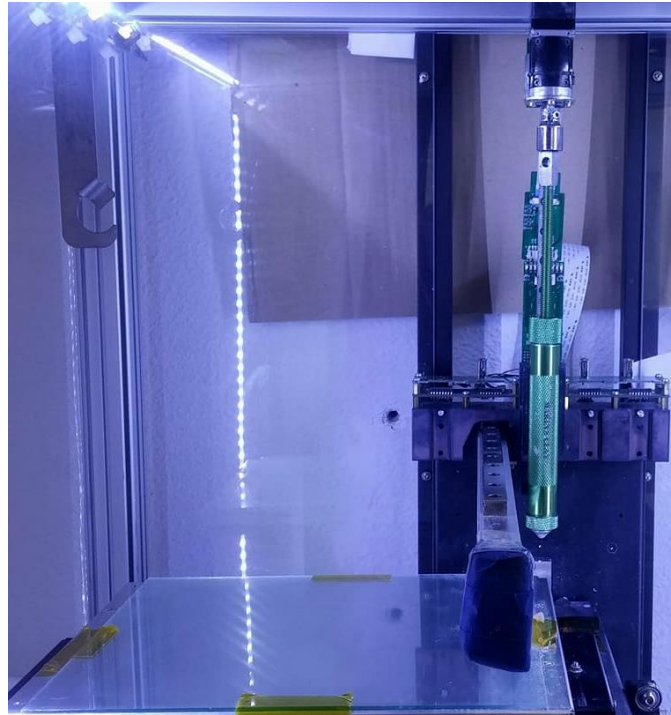


Figure 6.2: Picture of the 3D printer: the printing plate is equipped with a hot bed



Figure 6.3: Detail of the syringe

After extrusion, the material should completely solidify in order to maintain the printed shape. The solidification happens thanks to the evaporation of the solvent. After that, the printed pieces only consist of the inorganic powder bind together by the polymeric binder. The evaporation, depending on the volatility of the solvent used, could happen at room temperature or it may be needed the use of the hot bed, of which is equipped the printing plate.

As it has been already said, the material is extruded, and the piece is formed layer by layer. The AM printer must be capable of moving the plate or the cylinder in a horizontal plane starting and, when necessary, stopping the flow of material while printing. Once a layer is completed, the machine must move the cylinder upwards, or the plate downwards, so a further layer can be produced. The solidification of the layers should happen only after the printing of the following layer, letting it bind with the previous one.

6.3 Extrudable Paste and After-Printing Treatment

Generally speaking, the printable paste is a blend of an inorganic powder (metallic or ceramic) and a viscous solution made by a solvent and a polymeric binder. The powder is the material that one actually wants to print, while the solution confers the right viscosity for the printing process. The polymeric binder has also the crucial role of maintaining the piece shape after printing. Eventual additives such as lubricants, dispersant or surfactants may be used to facilitate the printing behaviour or have a better dispersion of the powder into the solution. Characteristic that is fundamental to prevent the formation of lumps or agglomerates that may complicate the extrusion.

Usually, afterwards, the 3D printed pieces are subject to a two-steps thermal treatment, as showed in “Figure 6.4”. The first step is needed to get rid of the polymeric component. The second is necessary to sinterize and consolidate the piece.

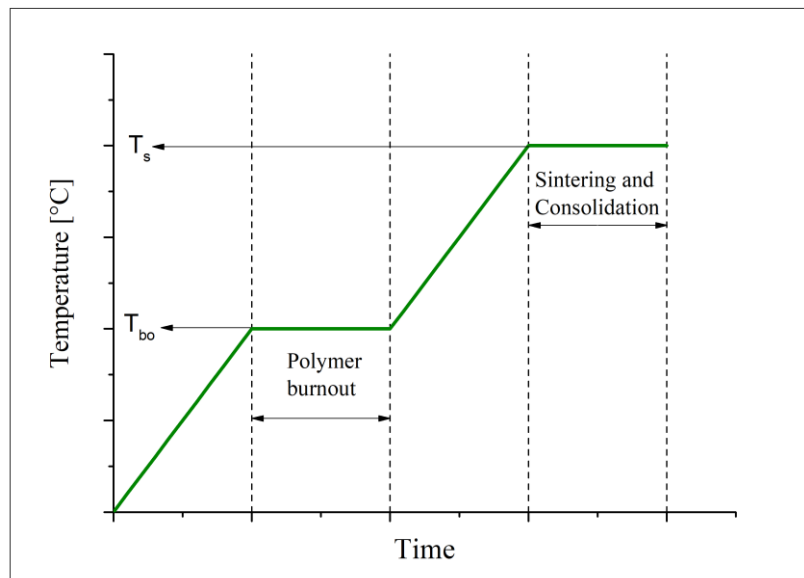


Figure 6.4: Representation of the thermal treatment necessary to get rid of the polymeric binder and consolidate the printed pieces

6.4 Paste formulation

The first step of the “paste receipt” conception should be the choice of the ingredients: they must be carefully selected. There is a large variety of possibility: many combinations of polymeric binders, solvents and additives are already used for many different applications. All of them may lead to good printing but the material selection must be done according to the application.

Some considerations are valid for any kind of application; the polymeric binder has to be coupled with a compatible solvent; the solvent has to evaporate in a reasonable time after printing but not being too volatile. If the evaporation, in fact, occurs during the printing the paste may get stuck inside the machine. The powder must be well dispersed inside the solution, so it is necessary a very good mixing. It is possible, for instance, by using a mechanical mixer. If this is not enough, some additives could be selected. The powder dimension is also an

important factor, too small grains could agglomerate easier than bigger ones, but on the other side too big grains may not pass the needle, blocking the process.

Specific considerations have to be made according to the specific process too. For example, if the final application is biomedical, then the ingredients must be biocompatible, or the following processes and treatments must lead to a complete removal of the non-biocompatible components. The chemical compatibility between powder, solvent, binder and additives must be always considered case by case. In this thesis work, considering that the final application concerns the use of magnesium silicide, an important consideration was made in the early stage of the work. The magnesium silicide reacts with water, so water was immediately excluded as a possible solvent.

6.4.1 Materials

Some possible ingredients were individuated and are reported in “Table 6.1”.

Table 6.1: Lists of the experimented materials

| SOLVENTS | BINDERS | ADDITIVES |
|-------------------------------------|--|------------|
| Ethanol Xylene Dodecanol | Ethyl cellulose (EC) Polystyrene (PS) | Oleic Acid |
| Acetone Dimethylacetamide (DMAc) | Cellulose acetate (CA) | Oleic Acid |

SOLVENTS:

Ethanol (Absolute anhydrous, Supplier: Carlo Erba Reagents)

Ethanol (formula in “Figure 6.5”) is a colorless and volatile liquid widely used as a solvent and preservative in many fields and as primary ingredient in alcoholic beverages.

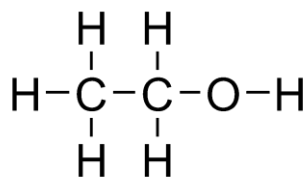


Figure 6.5: Chemical formula of ethanol (Source: www.wikipedia.org)

Xylene (o-xylene, Supplier: SigmaAldrich, reagent grade $\geq 98\%$) [63]

The term xylene represents the three isomers (ortho-, meta- and para- forms) of dimethyl benzene. “Figure 6.6” shows the chemical structure of the isomers. Xylene isomers have primary importance in the petrochemical industry since they are used as a basis for the synthesis of many organic compounds.

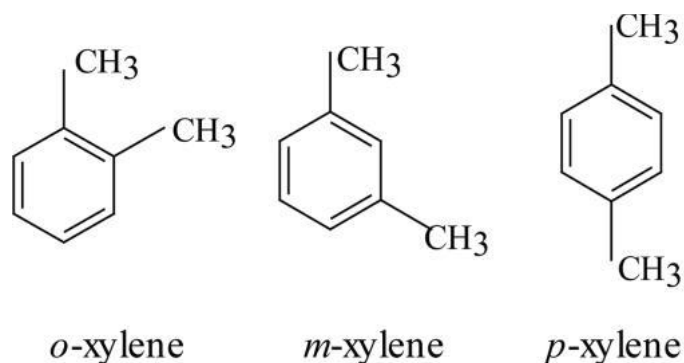


Figure 6.6: Chemical formula of xylene
 (Modified from [d]: Y. Zhou et al, *Thermodynamic Properties of o-Xylene, m-Xylene, p-Xylene, and Ethylbenzene*, 2012)

They are also widely used solvents. In this work was used the isomer *o*-xylene. In the following paragraphs and chapters of the thesis it is always reported only the word ‘xylene’: it has to be considered as the -orto isomer. However, the other isomers or a mixture of them could have been used without any appreciable difference.

Dodecanol (Supplier: Sigma Aldrich, purity $\geq 98\%$)

Dodecanol (or lauryl alcohol) is a saturated 12-carbon fatty alcohol. It is colourless and water insoluble. Its chemical formula is showed in “Figure 6.7”.

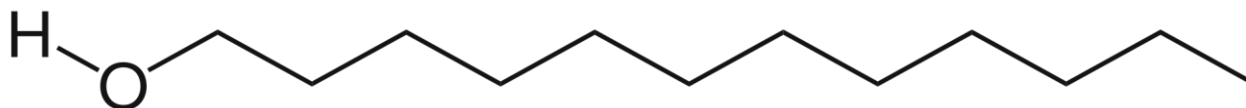


Figure 6.7: Chemical formula of dodecanol (Source: Wikipedia.com)

Acetone (supplier: SigmaAldrich, $\geq 99.5\%$)

Acetone (formula showed in “Figure 6.8”) is a colorless, volatile, flammable organic solvent.

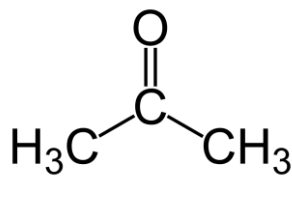


Figure 6.8: Chemical formula of acetone (Source: Wikipedia.com)

Dimethylacetamide DMAc (supplier: SigmaAldrich, anhydrous, 99.8%)

DMAc is a colorless liquid with a weak smell similar to ammonia. It presents comparable density of water. It may be toxic by skin absorption and irritate eyes and skin. Chemical formula in “Figure 6.9”.

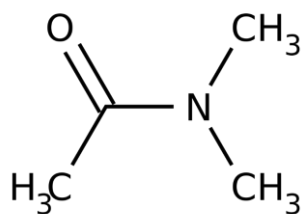


Figure 6.9: Chemical formula of DMAc (Source: Wikipedia.com)

BINDERS:

Ethyl cellulose (supplier: Sigma-Aldrich, 46% ethoxyl) [64]

Ethyl cellulose (EC) is a polymer derived from cellulose, in which some of the hydroxyl groups on the repeating glucose units are converted into ethyl ether groups. It has a wide diversity of applications ranging from organic soluble thermoplastic products to food additives, stabiliser and thickener in food industry. Ethyl cellulose is soluble in a wide variety of solvents: esters, aromatic hydrocarbons, alcohols, ketones, and chlorinated solvents. Monomer of EC is showed in “Figure 6.10”.

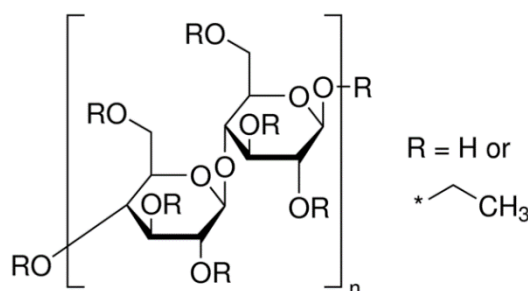


Figure 6.10: Chemical formula of repetitive unit of ethyl cellulose (Source: www.sigmaaldrich.com)

Polystyrene (supplier: Aldrich Chemistry, average Mw ~ 350000, average Mn ~ 170000) [65]

Polystyrene (PS) is an aromatic polymer synthesized from the monomer styrene (formula in “Figure 6.11”). Polystyrene (PS) belongs to the group of thermoplastics. Polystyrene has a linear hydrocarbon chain and dissolves in aromatic hydrocarbons (toluene, ethylbenzene, xylene). The mechanical and rheological behaviour of PS is mainly determined by its average molecular mass. PS with very good flow properties are often used for extrusion or injection molding processing.

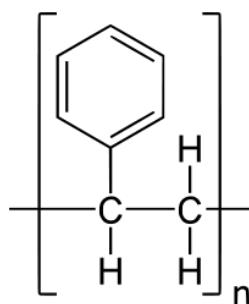


Figure 6.11: Chemical formula of styrene monomer (Source: www.wikipedia.org)

Cellulose acetate (supplier: Aldrich Chemistry, average Mn ~ 50000)

Cellulose acetate (CA) is a derivative of cellulose; it is used as an indirect food additive, photographic film and to produce synthetic fibers. It is a very appreciated fiber due to its low cost and good qualities. Cellulose acetate is one of the firsts synthetic fibers. The starting material of which CA is based is cotton or tree pulp cellulose. Monomer of CA is shown in “Figure 6.12”.

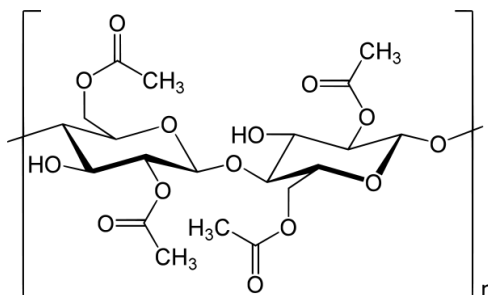


Figure 6.12: Chemical formula of constitutive monomer of Cellulose Acetate (Source: www.wikipedia.org)

ADDITIVE:

Oleic acid (supplier: Fluka Analytical)

Oleic acid (chemical formula in “Figure 6.13”) is an unsaturated fatty acid, commercially used in food and pharmaceutical industry.

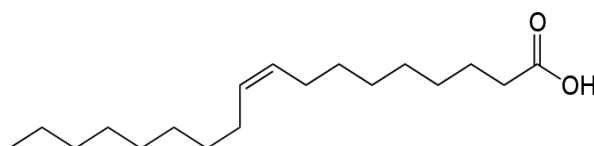


Figure 6.13: Chemical formula of oleic acid (Source: Wikipedia.com)

6.5 Paste formulation: Preliminary study

The main goal of this part of the work was to find one or more formulation that could lead to good printing behaviour and good quality of the printed pieces. This preliminary study was performed using silicon powder [40 µm] only, for a mere reason of opportunity. This study wanted to be the start for further formulations that include magnesium silicide or other silicon-based materials. The intention was to find one or more receipts that with small adjustments could be used in the second scenario.

The study concentrated mainly on the paste composition and on the proportion of the components. Printer settings were also considered, such as: rotation speed applied and temperature of the hot bed. The characteristics of the CAD models and printing parameters, like the height of the layers, were not optimized and are postponed for a further work. This preliminary study was a very time consuming and methodical work. It is described below and schematized in the flow chart represented in “Figure 6.14”.

6.5.1 Procedure

As a first step a known amount of binder was dissolved in a known amount of solvent. A certain amount of this solution (S) was mixed with a known amount of silicon powder, 40 μm (P). The proportion S/P has always been considered mass/mass; in this way eventual volume variation of the liquids, due to temperature variations in the laboratory, doesn't have to be considered.

The first times the proportion S/P was made by trial, starting from a proportion 50/50 up to reach a "satisfying" consistence and viscosity. The immediate following step was to insert some of the prepared paste in a syringe and try to manually extrude it out the needle. If it wouldn't happen or happened with difficulty, then something was adjusted in the paste formulation. If the manual extrusion would happen, the extruded paste would keep a "satisfying" consistence and showed a self-maintained shape, then it was tried to print.

It has to be noticed that, "adjusting the paste composition" means: change the proportion between the components and/or using additives. Changing the composition results mainly in a variation of viscosity.

The possible strategies to increase the viscosity are:

- increasing the amount of powder while keeping constant the amount of solution
- increasing the quantity of polymeric binder inside the solution while keeping constant the ratio S/P
- both the previous possibilities combined together

Clearly, to decrease the viscosity the procedure is the opposite.

In some cases, problems occurred due to an excessive volatility of the solvent; in those cases, the volatile solvent had to be substituted or mixed with non-volatile ones.

After passing the first steps and obtaining a printable paste, the quality of the printed pieces was evaluated. In this stage were printed simple shapes like small discs and 3D squares and more complex such as cylinders with an axial hole. This, indeed, was important criteria for discarding or eventually choosing a formulation. Some pictures of printings are shown in the next paragraph.

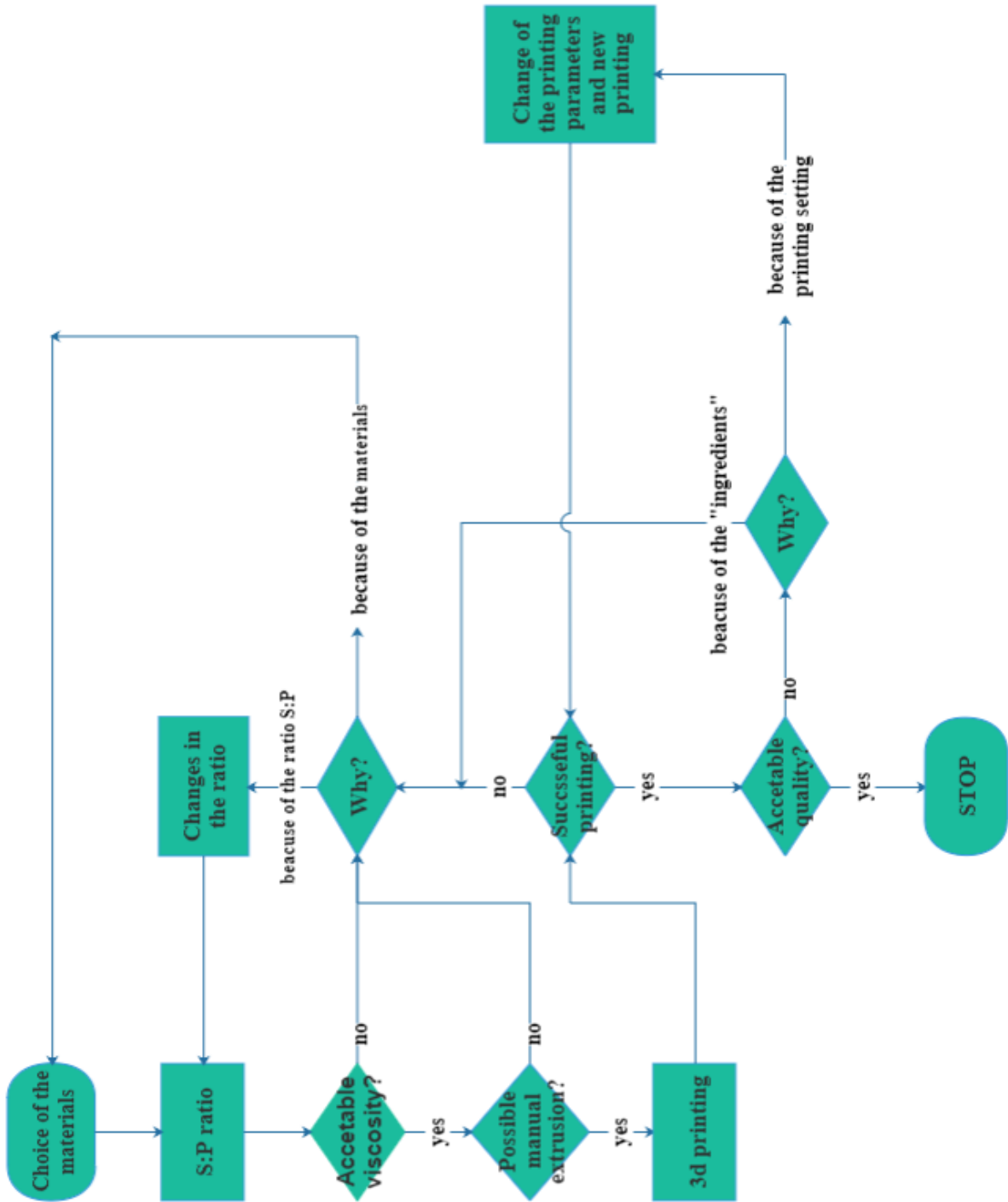


Figure 6.14: Flow chart schematizing the operating procedure of the preliminary study

6.5.2 Tested materials and formulations

This paragraph is a resume of all the “paste receipts” that were tried to print. Nine “groups” of formulations were individuated and listed with progressive numbers from 1) to 9).

In the first section of this paragraph, in the tables reported (from “Table 6.3” to “Table 6.11”) all the tested combinations (amount of binder, solvent, powder and additives) are listed. “Table 6.2” gives the reader the key to read the following tables.

In this section, also, images show some of the printed pieces, from “Figure 6.15” to “Figure 6.22”. The pictures correspond to printed pieces with the paste formulation marked with “ * ” in the related table. This information is also given in the caption of the figures.

The second section of the paragraph lists the advantages and disadvantages of each “group” of formulation. Everything is then resumed in “Table 6.12”. All these considerations led to selecting five formulations for further studies, discarding the others. The selected ones are marked in red in the tables.

During the printing process was sometimes changed the rotation speed of the plunger but, this is not here reported. The main goal of this part of the work, in fact, is to compare and chose the best “ingredients of the receipt”.

It has to be noticed how, in some lines of the table, sometimes is reported “+ oleic acid”. Oleic acid was the only used additive with the function of lubricant and fluidity improver. However, its use didn’t lead to any significant improvement; the use of this additive happened only few times before it was definitively discarded.

Legend:

EC: ethyl cellulose
CA: cellulose acetate
PS: polystyrene
Xy: xylene
Et: ethanol
Ac: acetone
DMAc: dimethylacetamide
Dod: dodecanol
Ol Ac: oleic acid

Table 6.2: Structure of Tables from 6.3 to 6.11

| Table structure: | | |
|---|---------------------------------------|-----------------------------------|
| Solvent (or mass proportion between solvents) | | Ratio S : P |
| BINDER | % of binder in the polymeric solution | Mass of Solution / Mass of Powder |

Group 1)

Table 6.3: Group 1) formulations

| Ethanol | | S : P |
|---------|-------|---------|
| EC | 7 % | 45 : 55 |
| | 7 % | 40 : 60 |
| | *10 % | 45 : 55 |

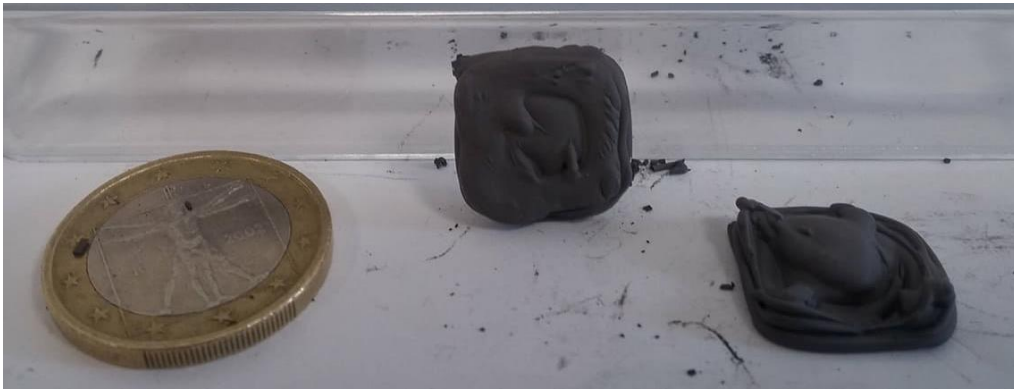


Figure 6.15: Printed pieces (Group 1), formulation with *EC 10 %, S : P = 45 : 55)

Group 2)

Table 6.4: Group 2) formulations

| Dodecanol | | S : P |
|-----------|----|---------|
| / | */ | 30 : 70 |
| | | |



Figure 6.16: Printed pieces using only dodecanol and Si powder (Group 2), formulation*)

Group 3)

Table 6.5: Group 3) formulations

| Dod : Et (1 : 1) | | S : P |
|------------------|------|---------|
| EC | 8 % | 45 : 55 |
| | 10 % | 50 : 50 |

Group 4)

Table 6.6: Group 4) formulation

| Ac : DMAc (1 : 1) | | S : P |
|-------------------|-------|---------|
| CA | *12 % | 40 : 60 |
| | | |

Group 5)

Table 6.7: Group 5) formulations

| Ac : DMAc (1 : 2) | | S : P |
|-------------------|------|---------|
| CA | 12 % | 45 : 55 |
| | 12 % | 40 : 60 |



Figure 6.17: Printed pieces (Group 4),

Group 6)

Table 6.8: Group 6) formulations

| Xy : Et (1 : 1) | | S : P |
|-----------------|-------|--------------------|
| EC | 7 % | 40 : 60 |
| | 7 % | 35 : 65 |
| | *10 % | 40 : 60 |
| | 10 % | 40 : 60 + Ol Ac |
| | 13 % | 40 : 60 |
| | 13 % | 37 : 63 |



Figure 6.18: Printed pieces (Group 6), formulation: EC 10 %, S : P = 40 : 60)*

Group 7)

Table 6.9: Group 7) formulations

| Xy : Et (1 : 2) | | S : P |
|-----------------|------|-----------------|
| EC | *5 % | 35 : 65 |
| | 10 % | 50 : 50 |
| | 10 % | 40 : 60 |
| | 10 % | 40 : 40 + Ol Ac |



Figure 6.19: Printed pieces (Group 7), formulation*)

Group 8)

Table 6.10: Group 8) formulations

| Xylene | | S : P |
|--------|-------|---------|
| EC | 2.5 % | 24 : 76 |
| | 3 % | 1 : 2 |
| | *5 % | 30 : 70 |
| | 8 % | 50 : 50 |

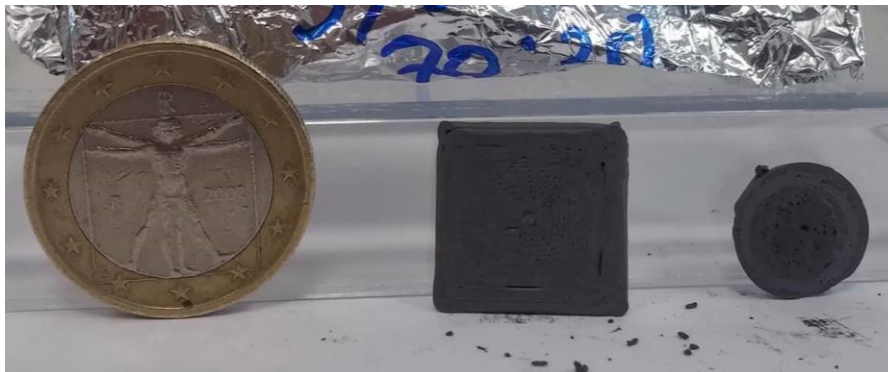


Figure 6.20: Printed pieces (Group 8), formulation*). The pieces show an improved quality in terms of definition, compared with the previous formulations.

Group 9)

Table 6.11: Group 9) formulations

| Xylene | | S : P |
|--------|--------|---------|
| PS | 3 % | 1 : 2 |
| | 5 % | 1 : 2 |
| | *10 % | 35 : 65 |
| | **20 % | 40 : 60 |



Figure 6.21: Printed pieces (Group 9), formulation*, PS 10 %). The pieces show good definition and quality.



Figure 6.22: Printed pieces (Group 9), formulation**, PS 20 %)

ADVANTAGES AND DISADVANTAGES

Group 1

- The ethanol used as a solvent alone resulted too volatile. That meant that the printing process stopped several times, due to the paste drying and getting stuck inside the syringe and the needle. That permitted to understand that volatile solvents should be used combined with non-volatile ones.

Group 2

- Dodecanol was tried alone without the use of any polymeric binder. That was possible thanks to the melting temperature of dodecanol: 24 °C. That means that at the operating temperature (room temperature) this solvent is solid or start to solidify. So, it was heated up to a complete melting and mixed with a known amount of powder. In this way it was possible to prepare a paste with a printable consistence. The self-maintaining of the pieces shape after printing, in this case, was possible thanks to the solidification of the solvent. Even it was observed a good printing behaviour and the absence of a polymeric binder was considered as a potential benefit (evaporation of dodecanol happens at 259°C, considerably lower than polymers burning out temperature), it was decided to not to optimize this formulation. The absence of a polymeric binder on the other side, in fact, lead to pieces too temperature sensitive. Temperature higher than 24 °C could melt the solvent leading to a shape-loss of the printed pieces. Concluding, this solution could be viable, but it wasn't optimized.

Group 3

- The mixture between dodecanol and ethanol led to a solvent with satisfying properties in terms of volatility and melting temperature (the mixture is fully liquid at room temperature). Ethyl cellulose is soluble in this mixture then, it was picked as a binder.

The printing behaviour was satisfying and the quality of the printed pieces too. In this stage was made an observation that, in the end, headed to discard this formulation. It was theorised that -OH groups of the solvent may react with magnesium silicide. In order to avoid any risk, the attention of this part of the work was moved to solvents with none or small amount of -OH groups; practically that means in the reduction or complete substitution of ethanol.

Group 4

- The proportion 1/1 acetone/DMAc resulted too volatile than these formulations were no more investigated.

Group 5

- The problem presented in the previous point was overcome using a higher percentage of non-volatile solvent (DMAc), however the quality of the printings was lower and less promising than the previous ones. The experimentations with these materials were then, stopped.

Groups 6 and 7

- Xylene was individuated as a possible substitute of ethanol: the two solvents were firstly tried combined (proportion xylene/ethanol: 1/1 and 1/2). The printing behaviour and quality gave very substantial and promising results. However, as already reported previously it was decided to keep investigating in order to find an ethanol-free formulation.

Groups 8 and 9

- Using only xylene as a solvent permitted to encounter the final selected formulations. Ethyl cellulose and polystyrene, both soluble in xylene, were used as binders. In the case of EC, smaller amounts of polymer were needed: dissolving only 8 % of EC in xylene, in fact, forms a very thick gel. Anyway, almost all the presented formulations had good printing response. It was, so, possible conclude the preliminary study: five formulations were picked (marked in red). The ones with PS and xylene are totally 'oxygen free', that may be an advantage when the powder is sensitive to oxidation. The slight disadvantage of these formulations is the necessity of using the printer hot bed to evaporate the solvent.

The advantages and disadvantages are summarized in "Table 6.12".

Table 6.12: Resume of the positive and negative sides of all the formulations experimented

| Group | Advantages | Disadvantages |
|-------|---|---------------------------------|
| 1 | / | Too volatile solvent |
| 2 | No use of a polymeric binder | Too temperature sensitive |
| 3 | Discrete printing behaviour | Presence of OH groups |
| 4 | / | Too volatile solvent |
| 5 | Improved conditions compared with 4) | Scarce quality of the printings |
| 6 | Good printing behaviour, no need of hot bed | Presence of OH groups |
| 7 | Good printing behaviour, no need of hot bed | Presence of OH groups |
| 8 | Good printing behaviour and quality of the printed pieces, -OH free | Use of hot bed |
| 9 | Good printing behaviour and quality of the printed pieces, -OH free | Use of hot bed |

6.5.3 Selected formulations

According to the printing performance, five formulations (resumed in “Table 6.13”) were selected as potential candidates for the following study.

Table 6.13: Resume of the selected formulations

| Solvent: Xylene | | | |
|-----------------|-------------|---------|----------------------|
| Binder | % of binder | S : P | Total polymer amount |
| EC | 2.5 % | 24 : 76 | 0.6 % |
| EC | 5 % | 30 : 70 | 1.5 % |
| PS | 5 % | 1 : 2 | 1.67 % |
| PS | 10 % | 35 : 65 | 3.5 % |
| PS | 20 % | 40 : 60 | 8 % |

The total amount of polymer (on the total mass) is the amount of polymeric binder in the printed pieces, assuming a total evaporation of the solvent. The total polymer amount was calculated simply multiplying the percentage of binder by the amount of solution in the paste.

6.5.4 Influence of powder grain size

Even though this aspect wasn’t deeply studied, it has been verified that the use of smaller powder grain size makes the printing process more difficult. As it has been said already all the previous presented tests were performed with commercial silicon powder (nominal particle dimension: 40 µm). It has been detected that real dimension of the particles is quite lower. Analysing some powder samples by scanning electron microscope (SEM) and calculating the average powder grain size by image analysis (“Figure 6.23”), it has been detected that the average grain size was 13.50 µm. The software used was ImageJ. Were measured 32 particles

and resulted a standard deviation of $7.50\ \mu\text{m}$. Since 32 is not a number big enough to create a consistent statistic, the reported average dimension doesn't want to be an absolute number. It wants to give a general idea: the particles dimension is lower than the nominal $40\ \mu\text{m}$ but higher than the case presented in the following paragraph.

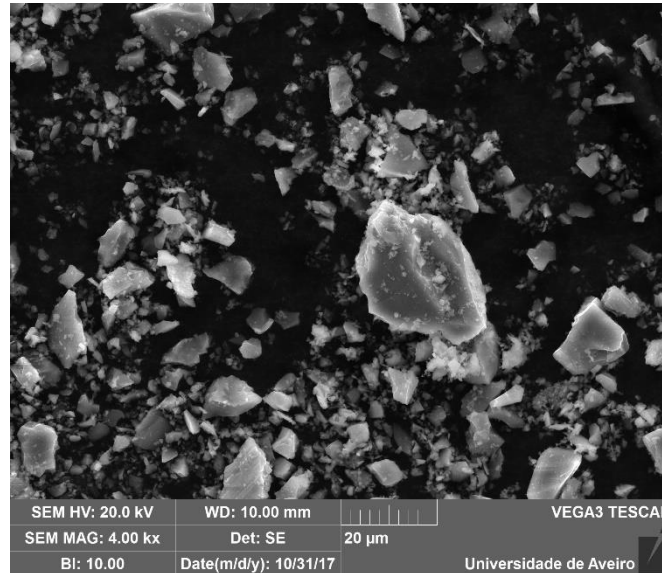


Figure 6.23: : SEM image used for calculating the average grain size of the commercial $40\ \mu\text{m}$ powder

The same $40\ \mu\text{m}$ powder was ball milled in a planetary ball mill PM100 for 5 hours. The dimension of the milled particles was analysed in the same way (“Figure 6.24”). The encountered average size was $1.07\ \mu\text{m}$ with a standard deviation of $0.48\ \mu\text{m}$ on 40 particles.

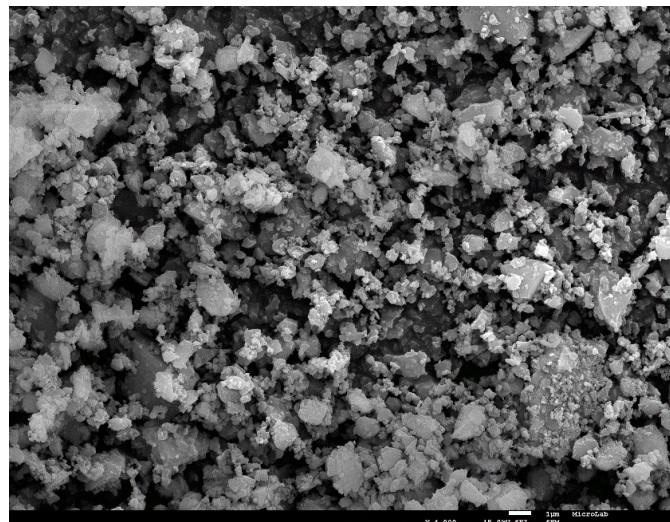


Figure 6.24: SEM image of 5 hours milled silicon powder

The size of the milled powder, as predictable, is clearly sensibly lower than the unmilled one. A paste was then made using the milled powder. It was chosen the formulation with 10 % of polystyrene in xylene with a proportion S : P, 35 : 65. Many lumps formed, turning impossible the printing process. The paste couldn't even be extruded out the 1 mm needle, the one used in all the previous work. It could be extruded out a bigger needle (nominal diameter of 1.5 mm).

So, it was tried to print but, the lumps agglomerate in the needle blocking the process. During the printing process sometimes, an amount of paste was suddenly extruded alternate with moments in which the printing was blocked. This behaviour could not lead to a good printing process as shown in “Figure 6.25”.



Figure 6.25: Particular of the printing process of milled silicon powder: lumps formed, turning impossible the printing

No more attempts were done to overcome the problem: such as the use of some surfactants that may prevent the formation of agglomerates.

6.6 DSC/TGA Analysis for de-binding temperature determination

DSC/TGA was performed on pieces printed with the five selected formulations. The aim of this analysis was to investigate the behaviour of the printings during the thermal treatment. In particular way, finding the burnout temperature (T_{bo} as indicated in the “Figure 6.4”) was the main goal of this section. T_{bo} is, in fact, the temperature at which is expected the polymeric binder to “go out”. Since it is an endothermic process was expected to observe, from the DSC analysis, one or more endothermic peaks. It also means a loss of mass, it was expected to observe it thanks to the TGA analysis, at more or less the same temperature of the endothermic peaks.

6.6.1 Polystyrene formulations: DSC/TGA results

DSC/TGA analysis was performed on the printed pieces of the selected formulations. “Figure 6.26” shows the results of DSC/TGA analysis performed on the formulation with 5 % of PS; “Figure 6.27” shows the results of the analysis on the “PS 10 %” formulation; “Figure 6.28”, the results of the analysis on the “PS 20 %” one. In all cases xylene is the solvent. The reader can find the resume with the selected formulations in “Table 6.13”. These first three analysis were performed in air, from room temperature up to 1000 °C with a heating ramp of 10 K/min. Another analysis (“Figure 6.29”) was performed on the “PS 20 %”, in nitrogen atmosphere, up to 800 °C, with the same heating ramp (10 °C/min) to compare the results and detect any eventual difference in the behaviour, due to the atmosphere. Since no differences were detected, the analysis in nitrogen wasn’t repeated for the other cases.

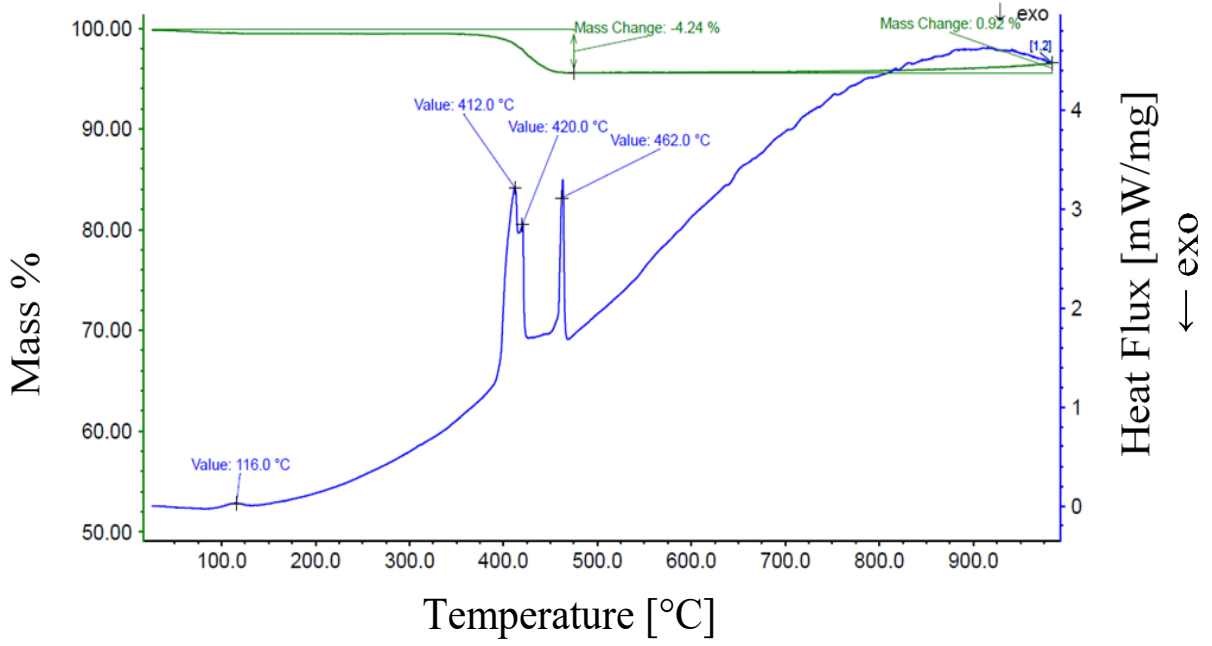


Figure 6.26: DSC/TGA analysis of the "PS 5 %" formulation. Atmosphere: air

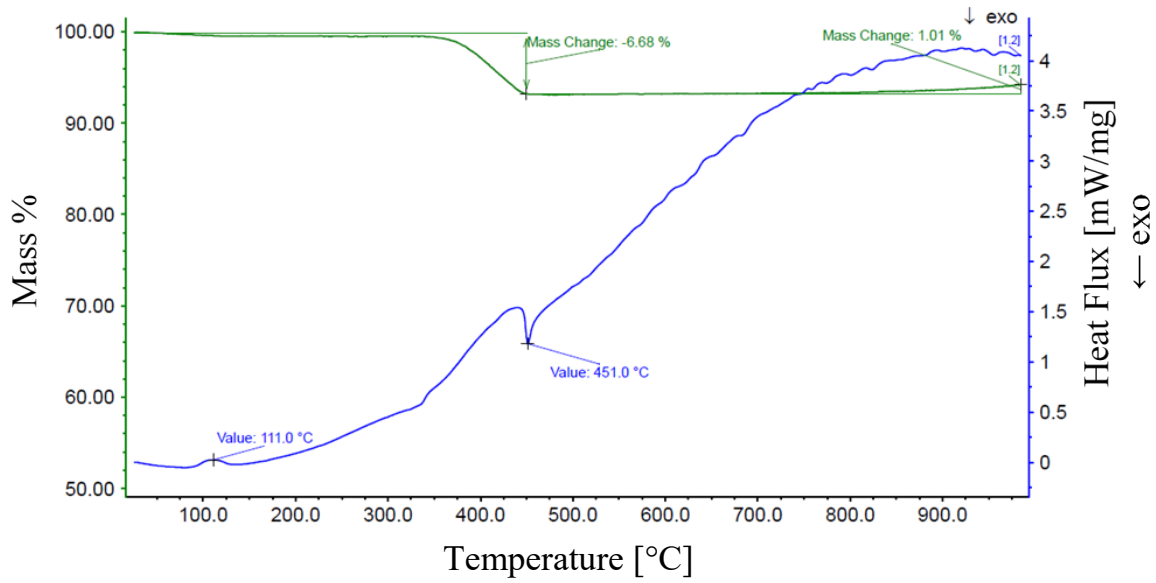


Figure 6.27: DSC/TGA analysis of "PS 10 %" formulation. Atmosphere: air

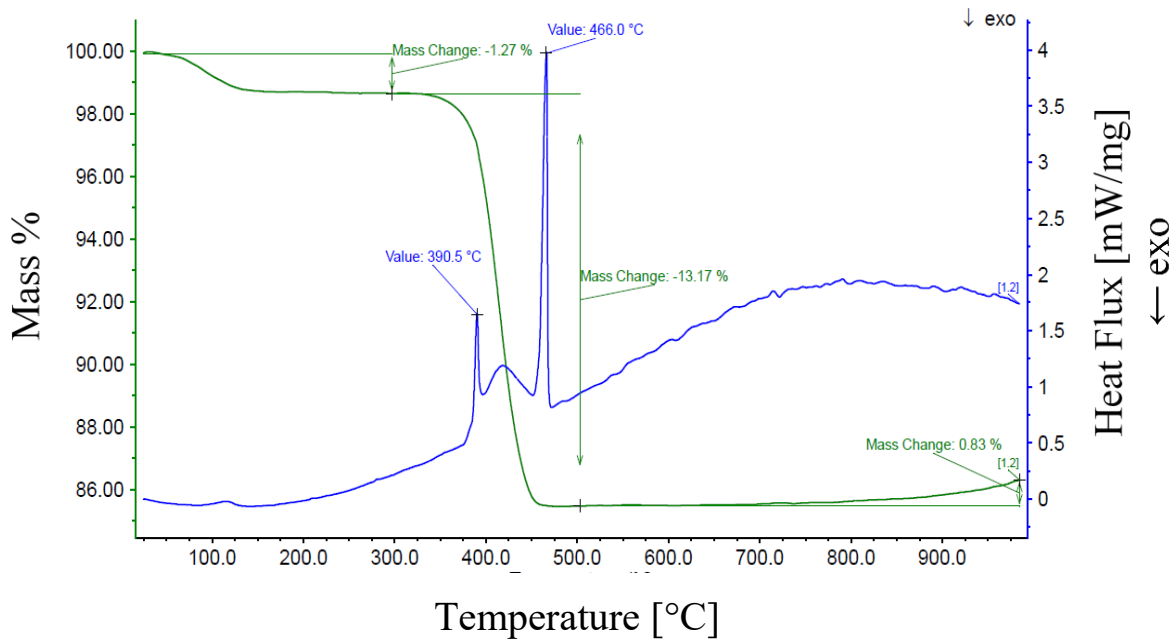


Figure 6.28: DSC/TGA analysis of “PS 20 %” formulation. Atmosphere: air

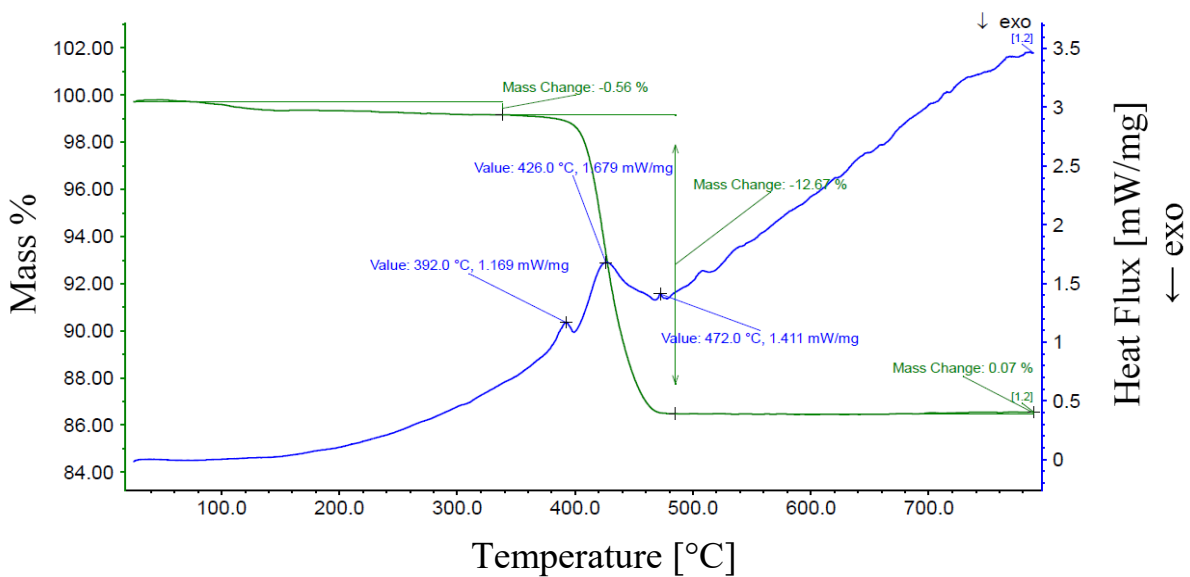


Figure 6.29: DSC/TGA analysis of “PS 20 %” formulation. Atmosphere: nitrogen

The results are compatible with the expectations. In an interval that is similar in the first three cases (400-460 °C / 400-450 °C / 390-470 °C) endothermic peaks were observed, while in the second sample the peak is less marked. In the same interval a loss of mass, compatible with the total amount of polymer, was observed. It is then clear that in this range polymer de-binding and burnout happen. The upper limit is then considered as the T_{bo} needed as the first thermal treatment step. The analysis performed in nitrogen showed a similar behaviour to the correspondent one performed in air (the third one). An endothermic peak appears between 390-470 °C and in the same interval a loss of mass is visible. Since differences weren't detected, no more analysis was done in nitrogen atmosphere.

6.6.2 Ethyl cellulose formulations

“Figure 6.30” shows the results of DSC/TGA analysis performed on the formulation with 2.5 % of EC; “Figure 6.31” shows the results of the analysis on the “EC 5 %” formulation. In all cases xylene is the solvent. The reader can find the resume with the selected formulations in “Table 6.13”. The analysis was performed in air, from room temperature up to 1000 °C with a heating ramp of 10 K/min.

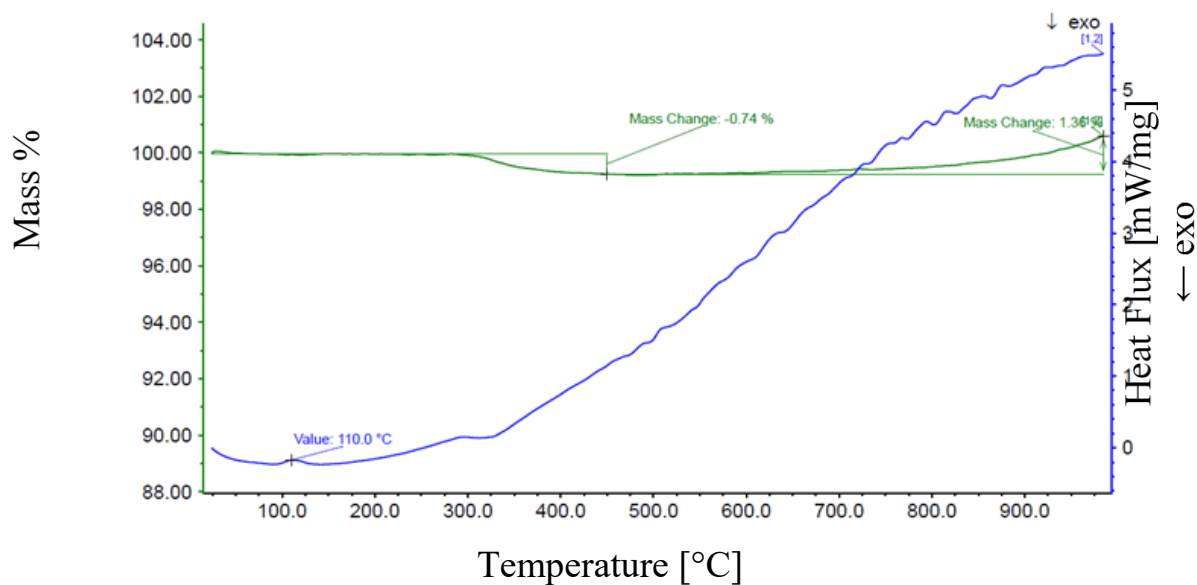


Figure 6.30: : DSC/TGA analysis of “EC 2.5 %” formulation

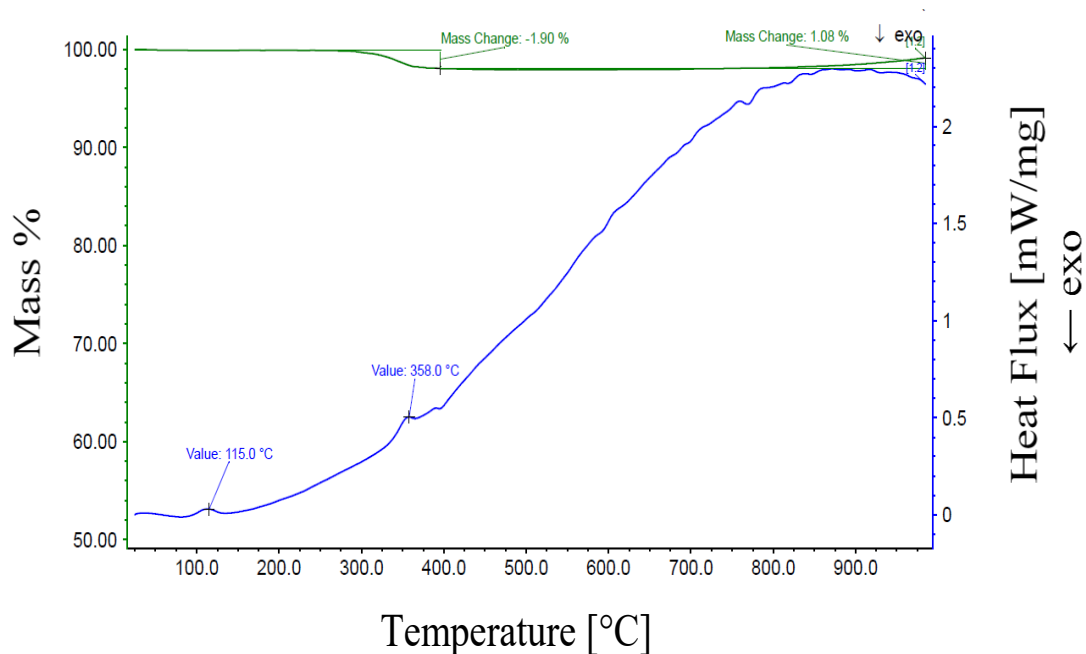


Figure 6.31: : DSC analysis of EC 5 % formulation

In this case no clear and marked endothermic peaks were observed. However, considering a small endothermic peak in the second formulation at 358 °C. At more or less the same temperature is visible, in both cases, a slight loss of mass compatible with the polymeric binder amount. The conclusion that can be drawn is then that the T_{bo} for EC formulations would have to be lower than the PS formulations.

6.6.3 Resume: Burnout Temperatures

In “Table 6.14” are resumed the T_{bo} , deduced from the previous analysis.

Table 6.14: Resume of the deduced T_{bo}

| | |
|-----------------|--|
| PS formulations | $T_{bo} \sim 460-470 \text{ }^\circ\text{C}$ |
| EC formulations | $T_{bo} \sim 360 \text{ }^\circ\text{C}$ |

6.7 3D printing of Mg_2Si powder

For the printing of the magnesium silicide fabricated powder, it was selected the 10%-PS formulation. In general, in fact, the printing performance was better for the PS formulations. The preliminary study gave, not only a basis for the following part of this thesis, but also is important source of information for eventual future work on this topic. For instance, it may provide useful information to whom would want to print Si-based materials, such as doped silicon powder.

For Mg_2Si the paste receipt was adjusted to the ratios indicated in “Table 6.15”. The magnesium silicide powder has been fabricated by ball milling and subsequently annealing in nitrogen atmosphere as discussed elsewhere.

Table 6.15: Experimented ratio S:P with magnesium silicide

| Solution (PS 10 %) | Powder (Mg_2Si) |
|---------------------------|---|
| 55 | 45 |
| 57 | 43 |

The printing behaviour was acceptable even though not optimum. The process run continuously without breaks, however the quality of the printing pieces – in terms of definition and resolution- was not particularly satisfying. This is visible in “Figure 6.32” and “6.33”. However, it is mainly a problem of paste composition and printing parameters. It is matter of finding the optimum ratio between polymeric solution and powder, experimenting the use of dispersant or surfactant that may guarantee a total homogeneity of the paste. At the same time, parameters regarding the printing process must be enhanced, such as rotation speed of the piston, height of the impressed layers. This is demanded to further works. Anyhow, one more time it has been demonstrated how additive manufacturing is a versatile and fast process. Pieces of many different shapes and dimensions are printable in short time (the pieces displayed in the pictures, and others not showed, were printed in about 3 hours work, including paste preparation and cleanings afterwards).



Figure 6.32: Mg_2Si Printed pieces (ratio 55 : 45)



Figure 6.33: Mg_2Si Printed pieces (ratio 57 : 43)

6.7.1 Post processing: de-binding and sintering

The printed pieces were subjected to a thermal treatment, with two main objectives: binder burnout (also called de-binding) and mechanical consolidation, as briefly explained in “Paragraph 6.3”. For this treatment the main parameters are:

- Heating rate (R_1) from room temperature to de-binding temperature
- Binder burnout temperature (T_{bo}) and hold time (H_1)
- Heating rate (R_2) from T_{bo} to sintering temperature (T_s)
- T_s value and hold time (H_2)

The T_{bo} depends on the binder. R_1 must be as lowest as possible [66], 1, 2 or 5 °C/min are values typically encountered in literature [67-70]. H_1 should be long enough for losing all the binder and typically goes from 30 minutes [69] up to 3 hours [71]. However, if the slow heating is kept from room temperature to T_s , it could be considered to not to have a hold time at T_{bo} . R_2 is usually faster than R_1 , even though a very wide range of values has been encountered in literature, from 3 °C/min [68] to 40 °C/min [71].

The hold time H_2 at the sintering temperature should be enough for the printed pieces to consolidate and it is in the order of one hour or more [66-70]. The sintering temperature is function of the material, typically between 70-90 % of the melting temperature.

6.7.2 Experimental setting

It has been used a furnace OTF-1200X-RTP-4 from MTI corporation (“Figure 6.34”), with internal quartz tube and digital vacuum gauge. The furnace allows to work in inert conditions (inert gas or vacuum). When operating in controlled atmosphere, according to furnace manual, some working limitations must be followed:

- at 800 °C, working time < 120 minutes
- between 1000 °C and 1100 °C working time < 10 minutes.

Exceeding these limits, the o-rings may melt. This was a limitation for the post-processing. As it has been presented in “Chapter 3”, magnesium silicide oxides at temperatures above 450 °C. The necessity of reaching high temperatures makes necessary working in inert conditions. The longer times needed for the post processing are clearly in contrast with the furnace restrictions.

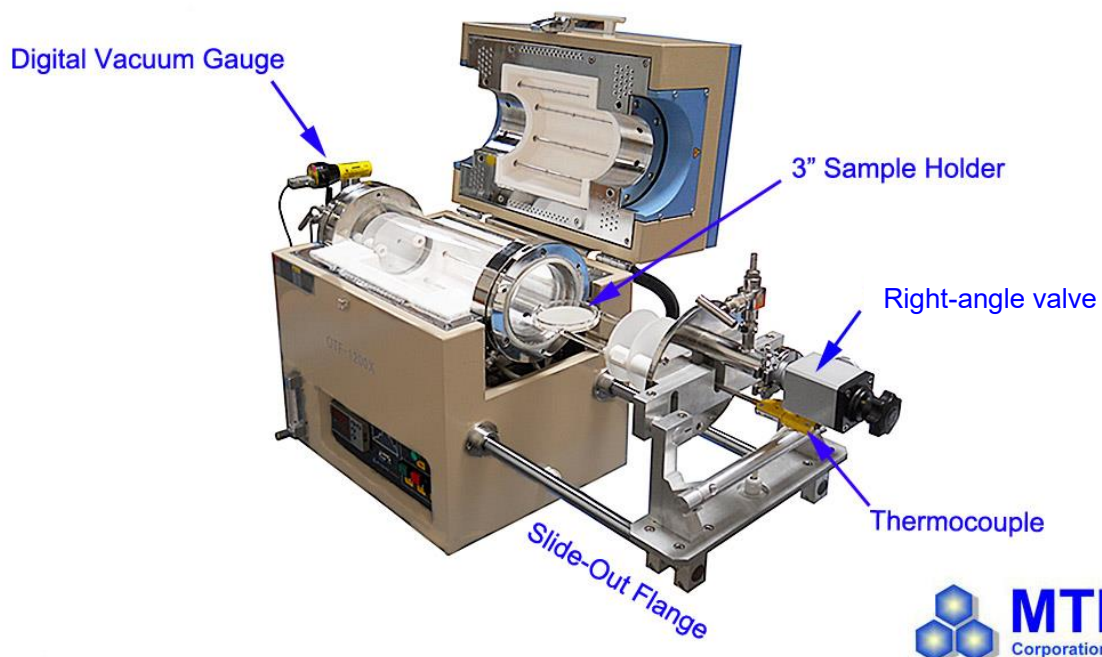


Figure 6.34: Picture of the oven used for post-processing of the printed pieces
(Source: www.mtixtl.com)

For testing the discussed parameters, small printed cylinders were used (nominal dimensions: diameter 4.5 mm and height 2 mm). T_{bo} (470 °C) was deduced from analysis (“Paragraph 6.6.1”), T_s , was hypothesised to be in the range 800-1000 °C (~ 70-90 % of Mg_2Si melting temperature).

Various cycles were experimented:

1. In the first thermal cycle, the temperature was increased from room temperature, with a heating rate of 5 °C/min, to 470 °C; this temperature was held for 90 minutes. Afterwards, with a ramp of 10 °C/min the temperature was increased to 800 °C and kept for 10 minutes. The cylinder didn’t present any mechanical property and got destroyed immediately after removing from the oven (“Figure 6.35”). This was predictable, in particular way because of the short hold time (10 minutes). It was observed a variation in the color piece before and after annealing (from dark-blue to brown). This is could be due to two reasons: not complete burnout of the binder or

color-change of the material itself. To understand this, in the following treatments it was included a small ball of polystyrene and a small quantity of Mg_2Si powder, as showed in “Figure 6.36”.



Figure 6.35: Broken cylinder after the first sintering attempt; the cylinder broke while extracting from the oven

2. The second cycle didn't contemplate a hold time at T_{bo} , since the temperature was slowly increased ($2\text{ }^\circ\text{C}/\text{min}$) from room T to $800\text{ }^\circ\text{C}$. The hold time was of 30 minutes. The annealed piece showed improved mechanical properties compared with the first attempt. It was possible to grab with hands the sample; however, it didn't stand little pressure applied with fingers and broke. Other useful info was given by this treatment. As showed by “Figure 6.37”, the polystyrene ball completely disappeared, the cylinder and the powder changed color (turning brown).

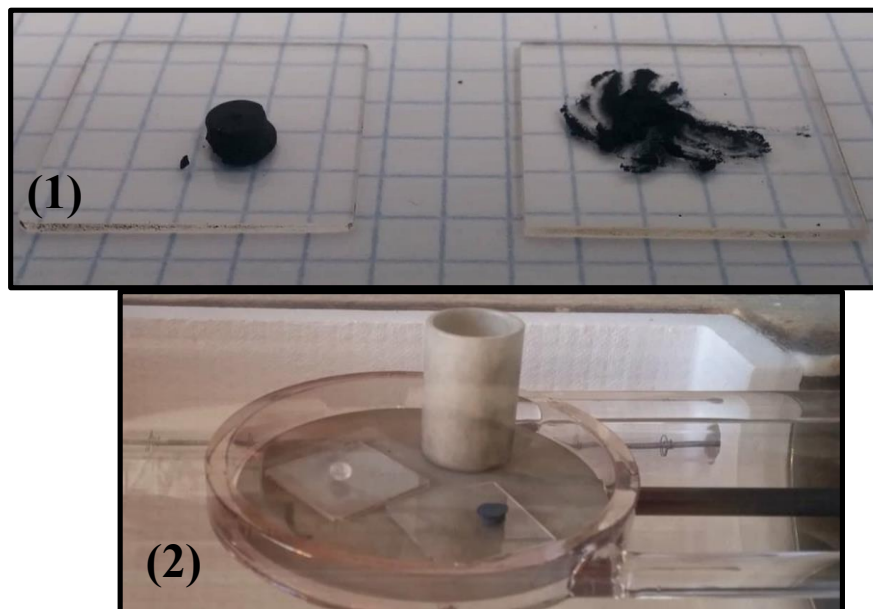


Figure 6.36: Picture of the materials before annealing.

- (1) Printed cylinder and Mg_2Si powder. They present dark-blue coloration.
- (2) Materials loaded into the furnace: the powder was inserted inside an alumina cylinder, simultaneously a small ball of polystyrene was subjected to the treatment too.



Figure 6.37: After thermal treatment the polystyrene completely vanished (*), while the cylinder and the powder turned brown.

- The third cycle contemplate a heating rate of 2 °C/min up to 470 °C, temperature held for 90 min. Than the temperature was increased with a heating rate of 4 °C/min to 900 °C/min, kept for 5 minutes; with the same ramp the temperature was decreased to 800 °C and maintained for 30 minutes. Also, in this case a small of PS and some magnesium silicide powder were loaded into the oven and annealed with the printed cylinder. Again, in the end of the treatment the polymer disappeared, and the powder turned brown, confirming the previous results. “Figure 6.38” shows the cylinder before and after sintering.

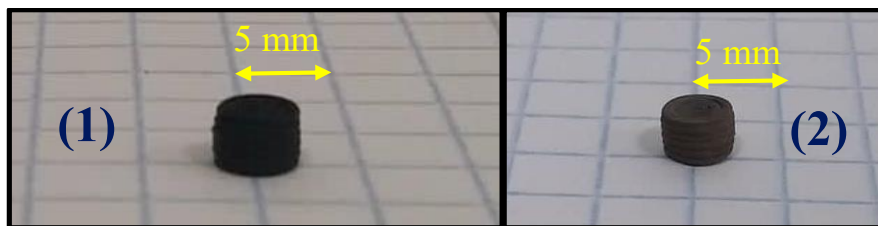


Figure 6.38: cylinder before (1) and after (2) cycle number 3.

The mechanical resistance increased, it was possible to handle with hands and apply small pressure with fingers. However, the piece broke when trying to perform electrical characterization.

Considering that in this treatment the piece stayed at a $T \geq 800$ °C for 85 minutes, of which 30 minutes at $850 \leq T \leq 900$ °C and 55 minutes in the range $800 \leq T \leq 850$ °C. After this annealing, it resulted clear how the sintering temperature applied wasn't enough to consolidate the printed pieces. It suggested that temperature higher than 900 °C are needed, with hold time in the order of 60-90 minutes, unfortunately out of the furnace limits. The last performed annealing (presented below), however, gave conflicting outcomes: suggesting that the unsuccess was not due (or not only, at least) to this presented “temperature problem”.

4. One last try was done by carrying out the post-processing in the tubular oven described in “Chapter 5”, “Paragraph 5.6.1”. This allowed to operate at temperatures above 900 °C without particular restrictions. The temperature profile used is represented by “Figure 6.39” and the parameters are resumed in “Table 6.16”. The treatment was performed in vacuum atmosphere with a pressure ranging from 10^{-3} to 10^{-5} mbar.

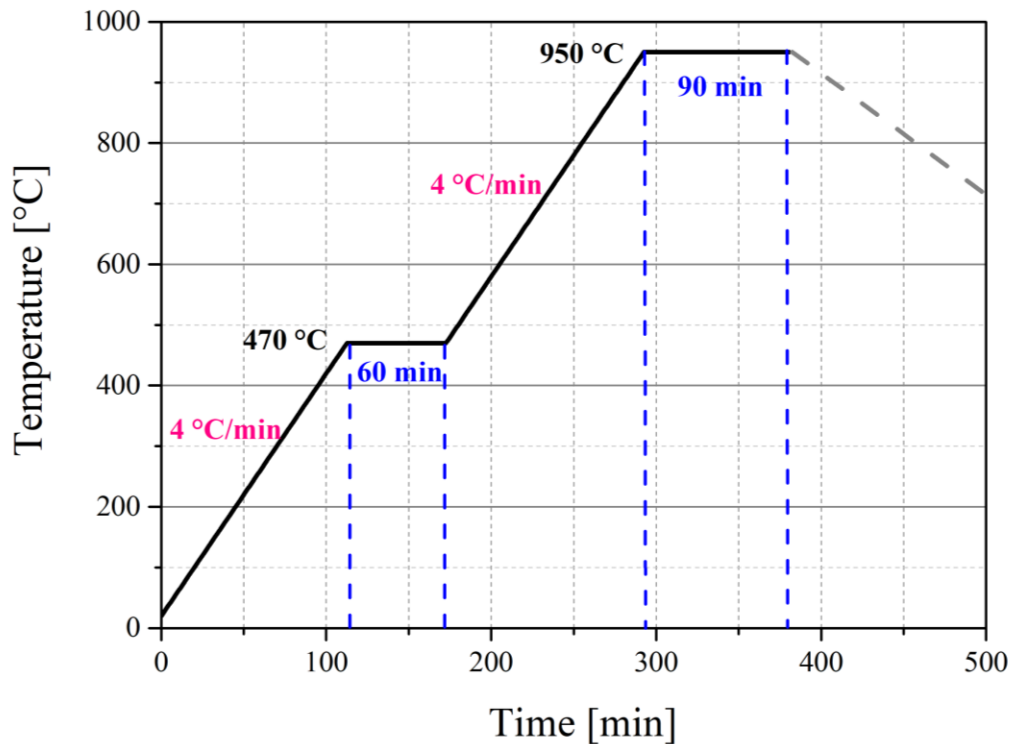


Figure 6.39: Scheme of the temperature perfil used for the last sintering attempt.

Table 6.16: Resume of the valuse of the last sintering attempt.

| | |
|-----------------------|----------|
| R₁ | 4 °C/min |
| T_{bo} | 470 °C |
| H₁ | 60 min |
| R₂ | 4 °C/min |
| T_s | 950 °C |
| H₂ | 90 min |

Printed pieces of different shapes and dimensions were subjected to the thermal treatment. Even this configuration didn't lead to mechanical consolidation of the printed pieces that broke while extracting from the oven. Unfortunately, it was not possible explore more solutions; so, the practical worked had to stop without any thermoelectrical characterization performed. XRD was performed on the treated pieces, the results showed in “Figure 6.40” explain why consolidation couldn't be achieved. In “Table 6.17” is showed a resume of the phase detected by XRD and their percentage.

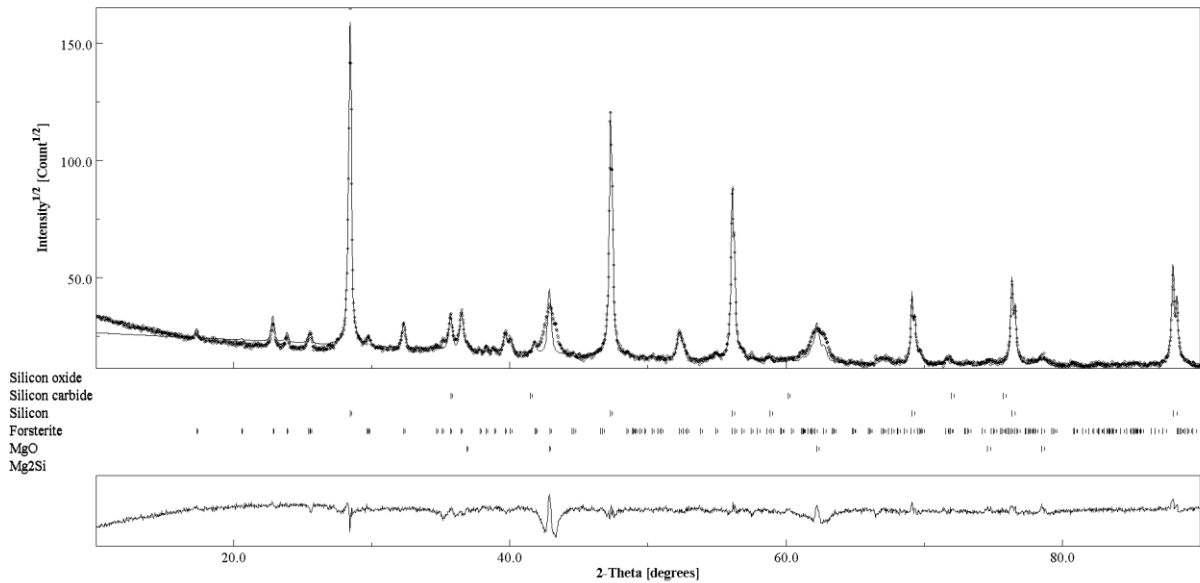


Figure 6.40: XRD pattern of the analysis performed on the thermal treated pieces

Table 6.17: Detected phases and their percentage

| Detected Phase | Weight % |
|---|----------|
| MgO | 9.54 |
| Mg ₂ SiO ₄ (Forsterite) | 22.19 |
| Silicon | 67.44 |
| Magnesium Silicide | 0 |
| Silicon Carbide | 0.83 |

Due to some chemical reactions happened during the treatment, magnesium silicide phase disappeared completely, turning silicon to be found in the highest weight percentage; formation of a considerable amount of forsterite was observed. The amount of MgO also increased and small peaks referable to silicon carbide appeared (probably due to the reaction with carbon of the organic binder). Mechanical consolidation couldn't then happen, because they are all compound with much higher melting points of Mg₂Si. The reactions may have been happened due to the high temperature and time applied. The treatment atmosphere and initial powder composition may have also influenced the process.

7 Conclusions

Magnesium silicide has gained great interest and attention in the past few years such as novel, eco-friendly, and innovative thermoelectric material. A combination of favourable physical, chemical, and electrical properties is the major reason that justify this increased interest. The fabrication of this intermetallic compound, however, is challenging because of:

- The great difference in the melting points of the constituents (silicon and magnesium), even with magnesium boiling point lower than silicon melting point
- The difficulty in avoiding magnesium oxide formation, even when operating in inert atmosphere due to the high reactivity of this element with oxygen
- The volatility of magnesium, that may evaporate during thermal treatments
- Mg_2Si is a “line compound”, meaning that non-stoichiometric composition lead to obtain coexistence of magnesium silicide with other phases/alloys/materials (for example silicon)

Another important challenge is the Mg_2Si devices fabrication with particular attention in developing fast and eco-friendly methods.

This thesis proposed a combination of materials synthesis method and devices fabrication, reporting then positive and negative conclusion.

The magnesium silicide synthesis happened successfully with a relatively short and easy process starting from powder constituents: combination of mechanical action and application of a thermal treatment. The mechanical action was applied by a high energy ball; its effectiveness is demonstrated by DSC analysis performed on non-milled powder (stoichiometric mixture) and on milled powder for 5 and 10 hours. Ball milling didn't lead alone to magnesium silicide formation as showed by XRD results, however analysing only this outcome may be misleading. Differential scanning calorimetry, in fact, showed a diminution of the temperature reaction (exothermic) between magnesium and silicon.

The mechanical action considerably increases the internal energy of the elements by the introduction of defects and stress, reduces the powder size and forces the constituents to be in intimate contact between them. This all result in a decrease of energy activation for the Mg_2Si formation reaction to happen. Practically it means in the possibility of operating at lower temperature in the following thermal treatment step. Treatment that is necessary for obtaining magnesium silicide. As it has been deduced by literature and discussed in this thesis the alloy formation, only by mechanical alloying, needs dozens of milling hours to be gained and in many cases, it is not even enough. The combination of mechanical action and of a thermal budget, it so, considered as an interesting and promising combination. Magnesium silicide has been fabricated also, only by thermal annealing without any previous milling. Indicating that, this option is also viable. The inconvenient is that the reaction happen at higher temperature: ~ 590 °C for unmilled powder, ~ 410 °C for 5-hours-milled and ~ 350 °C for 10-hours-milled.

In the “material-synthesis section” three different inert atmospheres (vacuum, nitrogen and argon) were tested (for the previously milled powder) for the thermal annealing step. In all cases magnesium silicide was obtained as a main phase, with coexistence with a small percentage of MgO ($\sim 4-6$ %) and a more important percentage of unreacted silicon ($\sim 10-12$ %).

In vacuum a considerable amount of Mg is lost by evaporation, so it is not advisable to operate in this atmosphere. Especially, because it was observed condensation of the evaporated Mg on the quartz tube walls of the furnace that had to be cleaned with nitric acid.

Nitrogen and argon atmosphere are considered quite identical, since led to very similar outcomes. In these cases, the residual presence of silicon in the annealed powder also suggests, somehow, loss of magnesium during the treatment. It wasn't observed condensation on the tube walls, indicating that eventual evaporated Mg may have been gone out with the gas flow. This may be a practical advantage.

From this, it has been concluded that to compensate magnesium loss during treatments, it is necessary to work in excess of magnesium.

An initial concern about N₂, namely the possibility of magnesium nitride formation, was proved by analysis to not to be happened. For this reason, nitrogen is preferable, since cheaper than argon.

The MgO formation, in a small but not negligible concentration, is a serious concern difficult to avoid; any step, from Mg storing and manipulation to milling and annealing, was performed in inert atmosphere.

These presented conclusions refer in particular way to the powder that in the experimental section was named "blue powder". The "grey powder", rich in magnesium oxide (~ 30-50 %), was obtained because of the practical configuration of the furnace and the gas inlet. The color difference was observed only in the cases in which, the inert gas was flowing directly on the powder, creating a "cold zone" in the area immediately close the gas tube. In configurations in which no gas was flowing directly on the powder, for instance in vacuum or when the powder was loaded inside the cylinder-type crucible, a colour difference grey/blue was not observed (all the powder was blue).

XRD gave information about the various phases present that were quantified by using the software Maud. Raman spectroscopy and FTIR-ATR also provided complementary information. Analysis by SEM showed morphology and size of the powder.

The second practical step of this thesis proposed the 3d printing of the fabricated material by paste-extrusion base method. Additive manufacturing is a wide known and spread method, but it hasn't been applied so far for Mg₂Si-based devices production. Additive manufacturing is a relatively fast process that also allows to obtain complex shapes. However, many parameters have to be considered and optimized.

The first step of this part was to perform a preliminary study using only silicon powder. The goal of this study was in first place to identify the most suitable "ingredients" for the extrudable paste namely solvent and polymeric binder. Many organic compounds were tested, ending up that xylene as solvent and ethyl cellulose and polystyrene as binders are the most promising options among the tested ones. Five paste formulations were individuated and worked as basis for the magnesium silicide printing.

Mg₂Si was successfully printed choosing and adjusting one of the five formulations. The quality of the printed pieces is certainly improvable, but due to the small amount of fabricated powder was not possible to optimize also this step.

The post-processing of the printed pieces consists in a two-step thermal treatment: de-binding and sintering. The de-binding temperature was obtained by DSC-TGA analysis (endothermic process). Some attempts were performed to consolidate the printed pieces however none of them resulted. This of course, couldn't permit any thermoelectrical characterization on the pieces. The reason why consolidation couldn't be performed was because during the sintering some chemical reactions happened, leading to get different phases respect to the initial ones.

7.1 Future perspectives

The presented procedure could be improved and optimized in several aspects, in particular:

- Find the most effective combination of parameters in terms of milling time, annealing time and temperature in order to identify the way that allows to save more time and energy possible
- Identify the correct excess of magnesium needed to obtain complete magnesium silicide formation without increase of oxide presence
- After the Mg_2Si fabrication route is optimized, it will be important to dope the material for obtaining n-type and p-type semiconductors for improving the TE properties and letting possible the fabrication of thermoelectric devices
- Optimize the printing parameters and paste formulation to obtain object with very good quality and definition
- Find the correct combination of parameters for effective de-binding and sintering; identifying also the best profile temperature to obtain the best combination in terms of TE and mechanical properties

If all these, absolutely not trivial, steps would be overcome, then it will be possible to think to scale up the production for industrial application. Such as in the automotive field, where good TE performance, light-weight and low cost are important issues.

List of Symbols and Acronyms

k_B : Boltzmann constant

Ac: Acetone

AM: Additive manufacturing

ATR: Attenuated total reflectance

BM: Ball milling

BSE: Backscattered electrons

CA: Cellulose Acetate

d: Interplanar distance

DMAc: Dimethylacetamide

Dod: Dodecanol

DSC: Differential scanning calorimetry

e: Electron charge

EC: Ethyl cellulose

Et: Ethanol

FT-IR: Fourier transform infrared spectroscopy

h, k, l: Miller indexes

h: Planck constant

H₁, H₂: Hold time

HP: Hot Pressing

L: Lorentz number

m*: Density of states effective mass

MA: Mechanical alloying

n: Carrier concentration

Ol Ac: Oleic acid

P: Powder

PF: Power factor

PS: Polystyrene

R₁, R₂: Heating rate

rpm: rounds per minute

S: Solution

SE: Secondary electrons

SEM: Scanning electron microscopy

SPS: Spark plasma sintering

T_{bo} : Burning out temperature, de-binding temperature

TE: Thermoelectricity/Thermoelectric

TEGs: Thermoelectric generators

TGA: Thermogravimetric analysis

T_s : Sintering temperature

Xy: Xylene

ZT: Figure of merit

α : Seebeck coefficient

η : Thermoelectric efficiency

κ : Total thermal conductivity

λ : Wavelength

ρ : Electrical resistivity

σ : Electrical conductivity

List of Figures

| | |
|--|----|
| Figure 2.1: Representation of p-type ($\alpha > 0$) and n-type ($\alpha < 0$) thermoelectric semiconductors | 6 |
| Figure 2.2: Structure of a TEG module..... | 8 |
| Figure 2.3: Structure of a TEG composed by many TE modules | 9 |
| Figure 2.4: Comparison of Carnot efficiency with TEGs efficiency in function of ZT | 10 |
| Figure 2.5: High ZT bulk thermoelectric materials listed with their weighted crustal abundance..... | 13 |
| Figure 2.6: ZT vs crustal abundance for bulk TE materials..... | 14 |
| Figure 3.1: Antifluorite structure of magnesium silicide | 15 |
| Figure 3.2: Correlation between MgO wt % and ZT at 320 K \square and 500 K \circ | 17 |
| Figure 3.3: Phase diagram magnesium-silicide..... | 18 |
| Figure 3.4: Comparison of DSC curves on milled and unmilled powders: Shifting of the exothermic peak. | 20 |
| Figure 3.5: Increase of internal energy by mechanical action, resulting in decrease of the activation energy of the formation reaction of Mg ₂ Si. | 21 |
| Figure 3.6: Carrier concentration [$10^{20}/\text{cm}^3$] vs Bismuth Atomic % | 23 |
| Figure 3.7: ZT function of Temperature and Bismuth atomic concentration | 23 |
| Figure 3.8: Dimensionless figure of merit (ZT) of Sb-doped Mg ₂ Si in function of dopant concentration and temperature. | 24 |
| Figure 4.1: Scheme of a SEM | 27 |
| Figure 4.2: Generation of secondary electrons (SE), back-scattered electrons (BSE) and x-rays after interaction of the sample with the primary electrons beam (PE)..... | 28 |
| Figure 4.3: Interaction between the incident x-rays beam and the materials atoms. | 28 |
| Figure 4.4: Scheme of the Bragg-Bentano congiguration..... | 29 |
| Figure 4.5: Scheme of Raman spectrometer. | 30 |
| Figure 4.6: Heat flux configuration for DSC analysis. | 31 |
| Figure 5.1: Horizontal section of a planetary ball mill | 34 |
| Figure 5.2: Picture of a planetary ball mill PM100 Retsch®..... | 38 |
| Figure 5.3: Picture of the milling tools: Jar (1), Balls (2) and security lid (3)..... | 38 |
| Figure 5.4: Hexane chemical formula (Source: www.wikipedia.org) | 39 |
| Figure 5.5: Picture of the glovebox (1), detail of the pre-chamber (2), preparation of a milling jar inside the glovebox (3)..... | 40 |
| Figure 5.6: Scheme of the operating routine for milling operation..... | 40 |
| Figure 5.7: DSC/TGA results of unmilled powder | 41 |
| Figure 5.8: DSC/TGA results of 5hours-milled powder | 42 |
| Figure 5.9: DSC/TGA results of 5hours-milled powder | 43 |
| Figure 5.10: DSC results comparison | 43 |
| Figure 5.11: TGA results comparison..... | 45 |
| Figure 5.12: Tubular oven used for annealing | 46 |
| Figure 5.13: Picture of the alumina crucibles used..... | 46 |
| Figure 5.14: Picture of the quartz tube still fixed on the support, after the oven was slided away in the end of thermal treatment. The tube was removed, and the crucible extracted only after reaching room temperature. The cooling, so, could happen while inside the tube the atmosphere was still inert..... | 47 |
| Figure 5.15: Pictures of the crucible inside the quartz tube before (1) and after (2) thermal treatment in N ₂ atmosphere. After the annealing it is visible an increase of volume of the | |

| | |
|---|----|
| powder inside the crucible and at the same a color difference is visible (blue and grey/brown, left and right side). | 48 |
| Figure 5.16: Pictures of the crucible inside the quartz tube, before (1) and after (2) argon annealing. After the treatment it is visible an increase of volume of the powder inside the crucible and at the same a color difference is visible (blue and grey/brown, left and right side). | 48 |
| Figure 5.17: Quartz tube “dirty” after Mg being evaporated during annealing in vacuum (first vacuum annealing (1), second (2) and third (3)). | 49 |
| Figure 5.18: Powder that was dragged along the tube during annealing in vacuum..... | 50 |
| Figure 5.19: Alumina crucibles containing a mixture of Mg and Si powder, inside the furnace quartz tube | 50 |
| Figure 5.20: XRD patterns comparison between Si, Mg and mixture 2 Mg-1 Si | 51 |
| Figure 5.21: Comparition of mixture Mg-Si before milling and after 5 and 10 hours of milling. | 52 |
| Figure 5.22: XRD patterns of powder milled 5 hours, before any therml treatment and powder (previously milled 5 hours) annealed in the three different atmosphere tested (N ₂ , argon and vacuum)..... | 53 |
| Figure 5.23: Comparaton between nle and grey powder after annealing in nitrogen atmosphere | 54 |
| Figure 5.24: Comparaton between blue and grey powder after annealing in argon atmosphere | 54 |
| Figure 5.25: XRD Patterns of milled and unmilled subjected to thermal treatment in N ₂ atmosphere. | 57 |
| Figure 5.26: Raman spectra of annealed and non-annealed powder | 60 |
| Figure 5.27: FTIR-ATR spectrum of 5hours milled powder | 61 |
| Figure 5.28: FTIR-ATR spectrum of annealed powder after milling. Comparition between nitrogen and argon blue and vacuum | 61 |
| Figure 5.29: FTIR-ATR spectrum of nitrogen and argon grey powder | 62 |
| Figure 5.30: SEM image of commercial silicon powder | 63 |
| Figure 5.31: SEM image of 5 hours milled powder (magnitude 1000x) | 64 |
| Figure 5.32: SEM image of 5 hours milled powder (magnitude 4000x) | 64 |
| Figure 5.33: SEM image of powder subject to annealing in nitrogen atmosphere (blue powder) after 5 hours milling powder (magnitude 4000x) | 65 |
| Figure 5.34: SEM image of powder subject to annealing in nitrogen atmosphere (blue powder) after 5 hours milling powder (magnitude 10000x) | 65 |
| Figure 5.35: SEM image of powder subject to annealing in nitrogen atmosphere (grey powder) after 5 hours milling powder (magnitude 4000x) | 66 |
| Figure 5.36: SEM image of powder subject to annealing in argon atmosphere (blue powder) after 5 hours milling powder (magnitude 4000x)..... | 66 |
| Figure 5.37: SEM image of powder subject to annealing in nitrogen atmosphere (blue powder) after 5 hours milling powder (magnitude 10000x) | 67 |
| Figure 5.38: SEM image of powder subject to annealing in argon atmosphere (grey powder) after 5 hours milling powder (magnitude 4000x)..... | 67 |
| Figure 5.39: SEM image of powder subject to annealing in vacuum atmosphere (grey powder) after 5 hours milling powder (magnitude 4000x) | 68 |
| Figure 5.40: SEM image of powder subject to annealing in vacuum atomosphere (blue powder) after 5 hours milling powder (magnitude 10000x) | 68 |
| Figure 6.1: Detail of the printing cylinder and syringe | 70 |
| Figure 6.2: Picture of the 3D printer: the printing plate is equipped with a hot bed..... | 70 |
| Figure 6.3: Detail of the syringe..... | 70 |

| | |
|---|----|
| Figure 6.4: Representation of the thermal treatment necessary to get rid of the polymeric binder and consolidate the printed pieces | 71 |
| Figure 6.5: Chemical formula of ethanol (Source: www.wikipedia.org)..... | 72 |
| Figure 6.6: Chemical formula of xylene | 73 |
| Figure 6.7: Chemical formula of dodecanol (Source: Wikipedia.com) | 73 |
| Figure 6.8: Chemical formula of acetone (Source: Wikipedia.com) | 73 |
| Figure 6.9: Chemical formula of DMAc (Source: Wikipedia.com) | 74 |
| Figure 6.10: Chemical formula of repetitive unit of ethyl cellulose (Source: www.sigmaaldrich.com) | 74 |
| Figure 6.11: Chemical formula of styrene monomer | 74 |
| Figure 6.12: Chemical formula of constitutive monomer of Cellulose Acetate (Source: www.wikipedia.org)..... | 75 |
| Figure 6.13: Chemical formula of oleic acid..... | 75 |
| Figure 6.14: Flow chart schematizing the operating procedure of the preliminary study | 77 |
| Figure 6.15: Printed pieces (Group 1), formulation with *EC 10 %, S : P = 45 : 55) | 79 |
| Figure 6.16: Printed pieces using only dodecanol and Si powder (Group 2), formulation*) .. | 79 |
| Figure 6.17: Printed pieces (Group 4), formulation*)..... | 80 |
| Figure 6.18: Printed pieces (Group 6), formulation*: EC 10 %, S : P = 40 :60) | 80 |
| Figure 6.19: Printed pieces (Group 7), formulation*)..... | 81 |
| Figure 6.20: Printed pieces (Group 8), formulation*). The pieces show an improved quality in terms of definition, compared with the previous formulations. | 81 |
| Figure 6.21: Printed pieces (Group 9), formulation*, PS 10 %). The pieces show good definition and quality. | 82 |
| Figure 6.22: Printed pieces (Group 9), formulation**, PS 20 %)..... | 82 |
| Figure 6.23: : SEM image used for calculating the average grain size of the commercial 40 μm powder | 85 |
| Figure 6.24: SEM image of 5 hours milled silicon powder | 85 |
| Figure 6.25: Particular of the printing process of milled silicon powder: lumps formed, turning impossible the printing | 86 |
| Figure 6.26: DSC/TGA analysis of the “PS 5 %” formulation. Atmosphere: air | 87 |
| Figure 6.27: DSC/TGA analysis of “PS 10 %” formulation. Atmosphere: air | 87 |
| Figure 6.28: DSC/TGA analysis of “PS 20 %” formulation. Atmosphere: air | 88 |
| Figure 6.29: DSC/TGA analysis of “PS 20 %” formulation. Atmosphere: nitrogen..... | 88 |
| Figure 6.30: : DSC/TGA analysis of “EC 2.5 %” formulation | 89 |
| Figure 6.31: : DSC analysis of EC 5 % formulation | 89 |
| Figure 6.32: Mg ₂ Si Printed pieces (ratio 55 : 45) | 91 |
| Figure 6.33: Mg ₂ Si Printed pieces (ratio 57 : 43) | 91 |
| Figure 6.34: Picture of the oven used for post-processing of the printed pieces | 92 |
| Figure 6.35: Broken cylinder after the first sintering attempt; the cylinder broke while extracting from the oven | 93 |
| Figure 6.36: Picture of the materials before annealing. | 93 |
| Figure 6.37: After thermal treatment the polystyrene completely vanished (*), while the cylinder and the powder turned brown..... | 94 |
| Figure 6.38: cylinder before (1) and after (2) cycle number 3. | 94 |
| Figure 6.39: Scheme of the temperature perfil used for the last sintering attempt. | 95 |
| Figure 6.40: XRD pattern of the analysis performed on the thermal treated pieces | 96 |

List of tables

| | |
|--|----|
| Table 5.1: Characteristics of materials milling tools [51] | 35 |
| Table 5.2: Suggested number of balls per bowl. In red the number of balls and in blue the % of filled volume in the jar by the balls (without counting powder and eventual fluid process). | 36 |
| Table 5.3: Summary of the calculations for evaluating the needed mass of Si and Mg powder | 40 |
| Table 5.4: Weight percentage of phases calculated with the software Maud | 55 |
| Table 5.5: Characteristics values of the fitted magnesium silicide peaks (referring to “Figure 5.22”)..... | 56 |
| Table 5.6: Mean experimental lattice parameters calculated values | 57 |
| Table 5.7: Phase percentages in the magnesium silicide obtained from unmilled powder, calculate by using software Maud | 58 |
| Table 5.8: Characteristics values of the fitted magnesium silicide peaks (referring to “Figure 5.25”)..... | 58 |
| Table 5.9: comparison of the detected peaks positions with values reported in literature | 62 |
| Table 5.10: Resume of the particle size analysed | 63 |
| Table 6.1: Lists of the experimented materials | 72 |
| Table 6.2: Structure of Tables from 6.3 to 6.11 | 78 |
| Table 6.3: Group 1) formulations..... | 78 |
| Table 6.4: Group 2) formulations..... | 79 |
| Table 6.5: Group 3) formulations..... | 79 |
| Table 6.6: Group 4) formulation | 79 |
| Table 6.7: Group 5) formulations..... | 80 |
| Table 6.8: Group 6) formulations..... | 80 |
| Table 6.9: Group 7) formulations..... | 80 |
| Table 6.10: Group 8) formulations..... | 81 |
| Table 6.11: Group 9) formulations..... | 81 |
| Table 6.12: Resume of the positive and negative sides of all the formulations experimented | 84 |
| Table 6.13: Resume of the selected formulations | 84 |
| Table 6.14: Resume of the deduced Tbo..... | 90 |
| Table 6.15: Experimented ratio S:P with magnesium silicide | 90 |
| Table 6.16: Resume of the valuse of the last sintering attempt..... | 95 |
| Table 6.17: Detected phases and their percentage | 96 |

Bibliography

- [1] Y. Demirel, *Energy: Production, Conversion, Storage, Conservation, and Coupling*, 2016, Second Edition, Springer, New York, USA
- [2] Xiao Zhang, Li-Dong Zhao, *Thermoelectric materials: Energy conversion between heat and electricity*, 2015, Journal of Materiomics 1, 92-105
- [3] W. Liu et al, *Eco-friendly high-performance silicide thermoelectric materials*, 2017, Natl Sci Rev, 2017, Vol. 4, No. 4, 611-626
- [4] R.D. Schmidt et al, *Mechanical properties of Mg₂Si thermoelectric materials with the addition of 0–4 vol% silicon carbide nanoparticles (SiC_{NP})*, 2015, J Mater Sci
- [5] Y. Pei et al, *Convergence of electronic bands for high performance bulk thermoelectrics*, 2011, Nature, Vol 473, 66-69
- [6] L. Anatyshuk et al, *On the discovery of thermoelectricity by A. Volta*, 2010, in Proceedings of the 8th European Conference on Thermoelectrics, Como, Italy
- [7] M Gartner et al, *Thermoelectricity*, 2012, Ullmann's Encyclopedia of Industrial Chemistry, Wiley-VCH Verlag GmbH & Co. KGaA, Weinheim, Germany
- [8] T. M. Tritt, *Thermoelectric Phenomena, Materials, and Applications*, 2011, Annu. Rev. Mater. Res. 41:433–48
- [9] J.R. Sootsman et al, *New and Old Concepts in Thermoelectric Materials*, 2009, Angew. Chem. Int. Ed., 48, 8616 – 8639
- [10] D. Champier, *Thermoelectric generators: A review of applications*, 2017, Energy Conversion and Management 140, 167–181
- [11] M. Brignone and A. Ziggotti, *Impact of novel thermoelectric materials on automotive applications*, 2011, FIAT Research Center, in Proceedings of the 9th European conference on thermoelectrics, published by American Institute of Physics
- [12] R. Amatya, R. J. Ram, *Trend for Thermoelectric Materials and Their Earth Abundance*, 2012, Journal of ELECTRONIC MATERIALS, Vol. 41, No. 6
- [13] G. Homm and P. J. Klar, *Thermoelectric materials – Compromising between high efficiency and materials abundance*, 2011, Phys. Status Solid RRL 5, No. 9, 324–331
- [14] L. A. Dvorina et al, *Preparation and some chemical properties of magnesium silicide*, 1969, Institute of Materials Science, Academy of Sciences of the Ukrainian SSR. Translated from Poroshkovaya, Metallurgiya, No. 5 (77), pp. 29-32
- [15] M. R. Bogala and R. G. Reddy, *Synthesis, characterization and Gibbs energy of thermoelectric Mg₂Si*, Processing, Properties, and Design of Advanced Ceramics and Composites, Ceramic Transactions, Volume 259, 143-152
- [16] D. Stathokostopoulos et al, *Oxidation resistance of magnesium silicide under high temperature air exposure*, 2015, J Therm Anal Calorim, 121:169–175
- [17] J Tani et al, *Thermoelectric properties and oxidation behaviour of Magnesium Silicide*, 2011, IOP Conf. Ser.: Mater. Sci. Eng. 18 142013
- [18] J. de Boor et al, *Microstructural effects on thermoelectric efficiency: A case study on magnesium silicide*, 2014, Acta Materialia 77, 68–75

- [19] A. Nadiradze et al, *Thermodynamic Probability of Realization of the Process of Silicon Dioxide Reduction by Magnesium at High Temperatures*, 2009, bulletin of the Georgian National Academy of Sciences, vol. 3, no. 2
- [20] I. Barin, *Thermochemical Data of Pure Substances*, 1995, Third edition, VCH Verlagsgesellschaft mbH, Weinheim (Federal Republic of Germany)
- [21] G.H. Li et al, *Magnesium Silicide Intermetallic Alloys*, 1993, Metallurgical Transactions A, Volume 24^o, 2383-2391
- [22] C. Uher, *Materials Aspect of Thermoelectricity*, 2017, CRC Press, Taylor & Francis Group, Boca Raton, USA
- [23] J. de Boor et al, *Fabrication parameters for optimized thermoelectric Mg₂Si*, 2014, J Mater Sci, 49:3196–3204
- [24] E. Godlewska et al, *Combustion synthesis of Mg₂Si*, 2011, Intermetallics 19, 1983-1988
- [25] E. Savary, *Fast synthesis of nanocrystalline Mg₂Si by microwave heating: a new route to nano-structured thermoelectric materials*, 2010, Dalton Trans., 39, 11074–11080
- [26] M. J. Yang et al, *Simple fabrication of Mg₂Si thermoelectric generator by spark plasma sintering*, 2009, Indian Journal of Engineering and Materials Sciences, Vol. 16, pp. 277-280
- [27] W. Liu et al, *Low-temperature solid state reaction synthesis and thermoelectric properties of high-performance and low-cost Sb-doped Mg₂Si_{0.6}Sn_{0.4}*, 2010, J. Phys. D: Appl. Phys. 43
- [28] C. Lee et al, *Fabrication of Mg₂Si Thermoelectric Materials by Mechanical Alloying and Spark-Plasma Sintering Process*, 2006, Journal of Nanoscience and Nanotechnology Vol.6, 3429–3432
- [29] L. Wang and X.Y. Qin, *The effect of mechanical milling on the formation of nanocrystalline Mg₂Si through solid-state reaction*, 2003, Scripta Materialia 49, 243–248
- [30] L. Lu et al, *Formation of nanocrystalline Mg₂Si and Mg₂Si dispersion strengthened Mg-Al alloy by mechanical alloying*, 1998, Nano Structured Materials, Vol. 10. No. 4. pp. 551-563
- [31] M. Ioannou et al, *Solid-state synthesis of Mg₂Si via short-duration ball-milling and low-temperature annealing*, 2012, Journal of Solid State Chemistry 197, 172–180
- [32] S. K. Bux et al, *Mechanochemical synthesis and thermoelectric properties of high quality magnesium silicide*, 2011, J. Mater. Chem., 21, 12259
- [33] J. Tani, H. Kido, *Thermoelectric properties of Sb-doped Mg₂Si semiconductors*, 2007, Intermetallics 15, 1202-1207
- [34] Q. Zhang et al, *In situ synthesis and thermoelectric properties of La-doped Mg₂(Si, Sn) composites*, 2008, J. Phys. D: Appl. Phys. 41, 185103 (6pp)
- [35] P. Gao et al, *Reduced lattice thermal conductivity in Bi-doped Mg₂Si_{0.4}Sn_{0.6}*, 2014, Appl. Phys. Lett. 105, 202104
- [37] N. Miyazaki et al, *Thermoelectric property of bulk CaMgSi intermetallic compound*, 2017, Journal of Alloys and Compounds 691, 914-918
- [38] Q. Zhang et al, *Thermoelectric performance of Mg_{2-x}Ca_xSi compounds*, 2008, Journal of Alloys and Compounds 464, 9–12
- [39] D. Berthebaud and F. Gascoin, *Microwaved assisted fast synthesis of n and p-doped Mg₂Si*, 2013, Journal of Solid State Chemistry 202, 61–64

- [40] A. M. Chiodoni and E. Tresso, *Morphological and Structural Properties*, 2013, Silicon Based Thin Film Solar Cells, Chapter 6, 146-176, Roberto Murri (Ed), Bentham Science Publishers
- [41] R.F. Egerton, *Physical Principles of Electron Microscopy. An Introduction to TEM, SEM, and AEM*, 2016, Second Edition, Springer International Publishing, Switzerland
- [42] F. Giorgis, *Lez 3 – SEM*, improved 2016, Slides from the course: Materials and characterizations for Micro and Nanotechnologies, Politecnico di Torino
- [43] W. D. Callister and D. G. Rethwisch, *Materials Science and Engineering. An introduction*, 2014, 9th edition, John Wiley & Sons, USA
- [44] S. A. Speakman, *Introduction to X-Ray Powder Diffraction Data Analysis*, 2016, Center for Materials Science and Engineering at MIT
- [45] U. Coscia et al, *Infrared and Raman Spectroscopies*, 2013, Silicon Based Thin Film Solar Cells, Chapter 5, 108-145, Roberto Murri (Ed), Bentham Science Publishers
- [46] F. Giorgis, *Lez. 7 – Raman, SERS, TERS*, improved 2016, improved 2016, Slides from the course: Materials and characterizations for Micro and Nanotechnologies, Politecnico di Torino
- [47] *Differential Scanning Calorimetry (DSC). A Beginner's Guide*, 2014, PerkinElmer, USA
- [48] *Simultaneous Thermal Analyzer – STA 449 F3 Jupiter®*, Method, Technique, Applications, Product Brochure, Netzsch, Germany
- [49] L. Lü and M. O. Lai, *Mechanical Alloying*, 1998, First Edition Springer Science + Business Media, New York, USA
- [50] M. Sopicka-Lizer, *High-energy ball milling. Mechanochemical processing of nanopowders*, 2010, First Edition, Woodhead Publishing Limited, Cambridge, UK
- [51] *The Art of Milling, An expert guide to neutral-to-analysis size reduction and homogenization in the laboratory*, 2017, Copyright © 2017 by RETSCH GmbH Haan
- [52] Tanja Butt and Gerhard Beckers, *Practical tips for the efficient grinding in laboratory ball mills*, in Proceedings of Retsch ® Live Webinar: Useful tips for efficient grinding in laboratory Ball Mills”, 7/12/2017
- [53] P.R. Soni, *Mechanical alloying, Fundamentals and Applications*, 2001, Cambridge International Science Publishing, Cambridge, UK
- [54] C. Suryanarayana, *Mechanical Alloying and Milling*, 2004, Marcel Dekker, New York, USA
- [55] Silicon Powder Safety Data Sheet, ThermoFisher Scientific, 13/04/2017
- [56] Magnesium Powder Safety Data Sheet, ThermoFisher Scientific, 12/04/2017
- [57] H. Uchida et al, *Synthesis of Magnesium Silicon Nitride by the Nitridation of Powders in the Magnesium-Silicon System*, 1997, Journal of the Ceramic Society of Japan 105
- [58] Y. Chunmiaoa et al, *Thermal analysis of magnesium reactions with nitrogen/oxygen gas mixtures*, 2013, Journal of Hazardous Materials 260 (2013) 707– 714
- [59] R. Saravanana and M. Charles Robert, *Local structure of the thermoelectric material Mg₂Si using XRD*, Journal of Alloys and Compounds 479 (2009) 26–31
- [60] I. Gibson, D. W. Rosen. B. Stucker, 2010, *Additive Manufacturing Technologies: Rapid Prototyping to Direct Digital Manufacturing*, Springer, New York, USA

- [61] F. Calignano et al, *Overview on Additive Manufacturing Technologies*, 2017, Proceedings of the IEEE (Volume: 105, Issue: 4, April 2017)
- [62] S.C. Ligon et al, *Polymers for 3D Printing and Customized Additive Manufacturing*, 2017, Chem. Rev., 2017, 117 (15), pp 10212–10290
- [63] Y. Zhou et al, *Thermodynamic Properties of o-Xylene, m-Xylene, p-Xylene, and Ethylbenzene*, 2012, Journal of Physical and Chemical Reference Data
- [64] G. S. Rekhi, S. S. Jambhekar, *Ethylcellulose - A Polymer Review*, 1995, Drug Development and Industrial Pharmacy, 21:1, 61-77
- [65] J. Maul et al, *Polystyrene and Styrene Copolymers*, 2012, Ullmann's Encyclopedia of Industrial Chemistry, Wiley-VCH Verlag GmbH & Co. KGaA, Weinheim, Germany
- [66] Uwe Scheithauer et al, *Thermoplastic 3D Printing—An Additive Manufacturing Method for Producing Dense Ceramics*, 2015, Int. J. Appl. Ceram. Technol., 12 [1] 26–31
- [67] M. Schwentenwein and J. Homa, *Additive Manufacturing of Dense Alumina Ceramics*, 2015, Int. J. Appl. Ceram. Technol., 12 [1] 1–7
- [68] L. Ren et al, *Process Parameter Optimization of Extrusion-Based 3D Metal Printing Utilizing PW–LDPE–SA Binder System*, 2017, Materials, 10, 305
- [69] L. Moballegh et al, *Copper injection molding using a thermoplastic binder based on paraffin wax*, 2005, Materials Letters 59 (2005) 2832 – 2837
- [70] G.C. Obasi et al, *Influence of processing parameters on mechanical properties of Ti–6Al–4V alloy fabricated by MIM*, 2010, Materials Science and Engineering A 527 (2010) 3929–3935
- [71] Z. W. Zhong, *Effects of Sintering Process Conditions on Size Shrinkages of Low-Temperature Co-Fired Ceramic Substrate*, 2006, Materials and Manufacturing Processes, 21:8, 721-726
- [72] S.A. Dotsenko et al, *Formation, optical and electrical properties of a new semiconductor phase of calcium silicide on Si(111)*, 2012, Asian School-Conference on Physics and Technology of Nanostructured Materials, Physics Procedia 23 (2012) 41 – 44
- [73] S.V. Vavanova et al, *Synthesis of Mg₂Si precipitates in Mg-implanted silicon by pulsed ion-beam treatment*, 2012, Asian School-Conference on Physics and Technology of Nanostructured Materials, Physics Procedia 23 (2012) 45 – 48
- [74] K. N. Galkin and N. G. Galkin, *Silicon overgrowth atop low-dimensional Mg₂Si on Si(111): structure, optical and thermoelectrical properties*, 2011, Physics Procedia 11 (2011) 55–58
- [75] E. Stefanaki et al, *Thermal Stability Study from Room Temperature to 1273 K (1000 °C) in Magnesium Silicide*, 2016, Metallurgical and materials transactions, 5146—volume 47a

Acknowledgements

I would like to thank all the people who contributed, somehow, to the work described in this thesis. Thanks to prof. Isabel and to Guilherme for the proposal and the possibility you gave me. Thanks to Ana, for all the time you spent following me, and for the patience. Thanks to all the 'lab team'.

I am really thankful for having had the possibility of living almost two years in Portugal, counting the time of Erasmus and the time for the master thesis. Living abroad made me grow so much as a person, and this is something inestimable.

Grazie alla mia famiglia, questa tesi è per voi. Grazie a mamma Claudia, per esserci sempre, per ascoltarmi e per avermi insegnato tanto. Grazie a papà Mauro, a Luca e a nonna Rosanna per il vostro supporto e appoggio. Includo nei ringraziamenti anche nonna Ada, che vorrei potesse vedermi raggiungere questo importante traguardo. Grazie a zii e cug(g)ini per la fiducia che avete sempre riposto in me.

Grazie a tutti i miei amici e alle persone che ho incontrato e frequentato; tutti coloro che sono stati parte in qualche modo di questi anni tra Casale, Torino e Lisbona. Tante facce e tante storie; tante persone che vorrei ringraziare e abbracciare una ad una. Su tutti, grazie a Rocco compagno di mille battaglie; le cose cambiano e si rinnovano continuamente, ma la tua amicizia è sempre stata, per me, una certezza.

Obrigado Lisboa pelos teus pores do sol, pela vida na rua, pelo sol e pelo mar. Obrigado pelas festas, pela cultura e pela comida boa. Obrigado pelos miradouros e pelos santos populares. Agradeço-te pelas pessoas maravilhoas que conheci. Obrigado Lisboa por ter estado uma segunda casa.

*“Lisboa menina e moça, amada
Cidade mulher da minha vida”*

Obrigado Inês por ter sido um verdadeiro apoio em cada momento desta tese, por ter estado sempre ao meu lado. Sem ti, tudo seria estado mais difícil; foste parte fundamental e imprescindível do meu trabalho e da minha felicidade em Lisboa.